

**PLASMA ENHANCED CHEMICAL VAPOR DEPOSITION OF SILICON
THIN FILMS: CHARACTERIZATION OF FILM GROWTH
AT DIFFERENT FREQUENCIES AND GAS COMPOSITIONS UTILIZING
PLASMA DIAGNOSTICS**

by

Lala Zhu

A dissertation submitted to the Faculty of the University of Delaware in partial fulfillment of the requirements for the degree of Doctor of Philosophy in Physics

Fall 2014

© 2014 Lala Zhu
All Rights Reserved

UMI Number: 3685169

All rights reserved

INFORMATION TO ALL USERS

The quality of this reproduction is dependent upon the quality of the copy submitted.

In the unlikely event that the author did not send a complete manuscript and there are missing pages, these will be noted. Also, if material had to be removed, a note will indicate the deletion.



UMI 3685169

Published by ProQuest LLC (2015). Copyright in the Dissertation held by the Author.

Microform Edition © ProQuest LLC.

All rights reserved. This work is protected against unauthorized copying under Title 17, United States Code



ProQuest LLC.
789 East Eisenhower Parkway
P.O. Box 1346
Ann Arbor, MI 48106 - 1346

**PLASMA ENHANCED CHEMICAL VAPOR DEPOSITION OF SILICON
THIN FILMS: CHARACTERIZATION OF FILM GROWTH
AT DIFFERENT FREQUENCIES AND GAS COMPOSITIONS UTILIZING
PLASMA DIAGNOSTICS**

by

Lala Zhu

Approved: _____
Edmund R. Nowak, Ph.D.
Chair of the Department of Physics and Astronomy

Approved: _____
George H. Watson, Ph.D.
Dean of the College of Arts and Sciences

Approved: _____
James G. Richards, Ph.D.
Vice Provost for Graduate and Professional Education

I certify that I have read this dissertation and that in my opinion it meets the academic and professional standard required by the University as a dissertation for the degree of Doctor of Philosophy.

Signed:

Robert W. Birkmire, Ph.D.
Professor in charge of dissertation

I certify that I have read this dissertation and that in my opinion it meets the academic and professional standard required by the University as a dissertation for the degree of Doctor of Philosophy.

Signed:

James MacDonald, Ph.D.
Member of dissertation committee

I certify that I have read this dissertation and that in my opinion it meets the academic and professional standard required by the University as a dissertation for the degree of Doctor of Philosophy.

Signed:

Steven S. Hegedus, Ph.D.
Member of dissertation committee

I certify that I have read this dissertation and that in my opinion it meets the academic and professional standard required by the University as a dissertation for the degree of Doctor of Philosophy.

Signed:

Ujjwal K. Das, Ph.D.
Member of dissertation committee

ACKNOWLEDGMENTS

First of all, I would like to use this opportunity to express my sincerest gratitude to my advisor Dr. Robert Birkmire for providing the opportunities of research and his kindly guidance and support through my entire Ph.D. program with his patience, motivation, enthusiasm and wealth of knowledge.

I would like to express my deepest gratitude to Dr. Steven Hegedus and Dr. Ujjwal Das for insightful advice, discussion and patient daily guidance which led me the right way to understand the film growth, characterization and plasma diagnostic. I would particularly appreciate Dr. Steven Hegedus for his help and support on my career development.

I would also thank my dissertation committee Dr. James MacDonald for his time to review my thesis proposal and provide suggestions on my research.

I wish to thank Dr. Robert Ridgeway of Air Products and Chemicals Inc. for helpful discussion and support. This work was partially funded by a Department of Energy grant DE-EE0000580 awarded to Air Products and Chemicals Inc. through a subcontract to Institute of Energy Conversion.

I would like to thank IEC staff Brian McCandless, Kevin Dobson, Chris Thompson and Shannon Fields for their advice and technique support. I would also

thank my friends Brent Shu, Lulu Zhang, Jianbo He, Peipei Xin and Lei Zhang for their suggestions and joyful discussions.

Last but not least, I would like to thank my parents Zhiqin Chen and Mingliang Zhu, my wife Fei He for their patience, understanding, encouragement and love during my Ph.D. pursuit. None of this would ever have been accomplished without their support.

TABLE OF CONTENTS

LIST OF TABLES	x
LIST OF FIGURES	xii
ABSTRACT	xvii

Chapter

1	INTRODUCTION	1
1.1	Research Motivation.....	1
1.2	Thesis Outline.....	9
2	FUNDAMENTAL OF PLASMA ENHANCED CHEMICAL VAPOR DEPOSITION AND PLASMA DIAGNOSTICS	11
2.1	Fundamental of Plasma Enhanced Chemical Vapor Deposition.....	11
2.1.1	Plasma Discharge in PECVD System	12
2.1.2	Plasma and substrate surface interaction in PECVD.....	16
2.1.3	PECVD Silicon thin film growth mechanism	17
2.2	Plasma Diagnostic	19
2.2.1	Optical Emission Spectroscopy.....	19
2.2.2	Langmuir Probe.....	22
3	SILICON THIN FILM DEPOSITION, FILM AND DEVICE CHARACTERIZATION.....	27
3.1	Multi-Chamber Plasma Enhanced Chemical Vapor Deposition (PECVD) System	27
3.2	Material Characterization	30
3.2.1	Ultraviolet-Visible-Infrared (UV-VIS-IR) Spectroscopy.....	30
3.2.2	Fourier Transform Infrared Spectroscopy (FTIR).....	32
3.2.3	Raman Spectroscopy	36
3.2.4	X-Ray Diffraction.....	40
3.3	Solar Cell Device Characterization	42

4	AMORPHOUS SI FILM DEPOSITION AND SOLAR CELL WITH GAS PHASE ADDITIVE	44
4.1	Introduction	44
4.2	Experiment	45
4.3	A-Si:H Deposition and Material Properties with and without Si ₂ H ₆ Additive	47
4.3.1	A-Si:H deposition without H ₂ dilution	47
4.3.2	A-Si:H deposition with H ₂ dilution	49
4.3.3	Effect of deposition Temperature	55
4.4	Device Performance of a-Si:H at Different Deposition Conditions	59
4.4.1	Solar cell performance: i layer with Si ₂ H ₆ and without H ₂ Dilution	60
4.4.2	Effect of growth temperature and H ₂ dilution on solar cell without additive	61
4.4.3	Effect of growth temperature and H ₂ dilution with Si ₂ H ₆ additive and stability performance	64
4.5	Summary	65
5	NANOCRYSTALLINE SILICON FILM DEPOSITION AND CHARACTERIZATION	67
5.1	Introduction	67
5.2	Experiment	69
5.3	Nc-Si:H Thin Film Deposition with Variable Parameters	70
5.3.1	Effect of H ₂ dilution on nc-Si:H film deposition	71
5.3.2	Effect of RF Power on nc-Si:H deposition	73
5.3.3	Effect of Deposition Pressure on nc-Si:H film deposition	74
5.3.4	Effect of RF Frequency on nc-Si:H film deposition	76
5.3.5	Nc-Si:H film deposition with Si ₂ H ₆ additive	78
5.4	Nc-Si:H Film Structural Properties	80
5.4.1	Raman Crystal Volume Fraction and XRD Grain Size	80
5.4.2	Grain Size and Growth Orientation of nc-Si:H by RF	82
5.4.3	Evolution of nc-Si:H growth orientation	85
5.4.4	Grain Size and Growth Orientation of nc-Si:H by VHF	86
5.4.5	Structural properties of nc-Si:H deposited with Si ₂ H ₆ additive ..	87

5.5	Nc-Si:H Solar Cell Device Performance	89
5.5.1	Solar cell performance on ZnO-coated SnO ₂ :F/glass (TEC 8 brand) and Al doped ZnO/glass substrates	90
5.5.2	Nc-Si:H solar cell with different back reflector contact.....	97
5.6	Summary.....	99
6	INSIGHT OF SILICON FILM DEPOSITION BY PLASMA DIAGNOSTICS	101
6.1	Introduction	101
6.2	Experiment	102
6.3	Plasma Characterization in a-Si:H Deposition Regime by OES	105
6.3.1	Relationship between SiH* and a-Si:H Growth Rate.....	106
6.3.2	OES Analysis: Effect of RF Power for a-Si:H deposition and film properties	108
6.3.3	OES Analysis: Effect of Si ₂ H ₆ Additive	110
6.3.4	OES Analysis: Effect of H ₂ dilution for a-Si:H deposition.....	112
6.4	Plasma Characterization in nc-Si:H Deposition by OES	113
6.4.1	Effect of SiH ₄ Flow and Partial Pressure.....	115
6.4.2	SiH* and nc-Si:H growth Rate	116
6.4.3	H α /SiH* and Raman Xc	117
6.4.4	OES measurement at different Pressure	118
6.4.5	Effect of RF Power on SiH* and H α /SiH*	120
6.5	Nc-Si:H Deposition Plasma Properties by Langmuir Probe Measurement	121
6.5.1	EEDF at Different Pressure measured by Langmuir Probe.....	121
6.5.2	Sheath Potential of the plasma and Effect on Grain Size	124
6.5.3	Interpretation of OES results at different pressure by Langmuir Probe Analysis.....	126
6.5.4	Effect of RF Power and EEDF inside Plasma	127
6.5.5	Comparison of RF and VHF Plasma with Langmuir Probe Measurement	129
6.6	Summary.....	129
7	SUMMARY AND OUTLOOK	131

REFERENCES134

Appedix

A-Si:H P-I-N SOLAR CELL STABILITY 141

LIST OF TABLES

Table 2-1	Electron and Molecule interaction inside PECVD plasma	14
Table 2-2	Summary of variable Voltage Region for Langmuir Probe data Interpretation	24
Table 3-1	Range of Si thin film deposition parameters in this research	29
Table 4-1	Intrinsic a-Si:H main deposition parameters with and w/o additive	46
Table 4-2	A-Si:H deposition conditions and film structural properties at substrate temperatures of 200 °C and 250 °C	56
Table 4-3	JV performance comparison of devices with and without 10% Si ₂ H ₆ additive	61
Table 4-4	A-Si:H p-i-n cell results with different i layer conditions. Initial cell performance and % degradation after LS shown. Cells without Si ₂ H ₆ (SiH ₄ /Si ₂ H ₆ /H ₂ =10/0/50) are in bold. All others are with SiH ₄ /Si ₂ H ₆ /H ₂ =9/1/50. All devices deposited at 200°C except for the last entry deposited at 250°C. i layer deposited at 1.25 Torr (white background) or 2.5 Torr (tan background)	64
Table 5-1	Nc-Si:H growth rate, X _c with different H ₂ /SiH ₄ ratio by VHF	77
Table 5-2	RF and VHF Growth Rate and Raman X _c of nc-Si:H deposited by H ₂ /SiH ₄ with and without Si ₂ H ₆	80
Table 5-3	Raman X _c , growth rate, XRD analysis results for nc-Si:H film deposited by RF	83
Table 5-4	Nc-Si:H deposited by RF and VHF with and without Si ₂ H ₆ additive	88
Table 5-5	JV performance of nc-Si:H p-i-n solar cell with Al back contact on different substrates	91
Table 5-6	Gain Size of nc-Si:H on different substrates	93

Table 5-7	JV performance of nc-Si:H p-i-n solar cell with Al back contact on different substrates.....	96
Table 5-8	JV comparison of nc-Si:H solar cells with different Back Contact	97
Table A-1	Device stability performance of p-i-n solar cells fabricated at: 1. 200C and 2. 250C, RF 25W, 0.5 Torr with pure SiH ₄ ; 3. 200C, RF 30W, 1.25 Torr with H ₂ dilution R=5.....	142

LIST OF FIGURES

Figure 1-1	U.S PV installations and System Price	2
Figure 1-2	New electricity Generation Capacity in US, 2012 vs 2013	3
Figure 1-3	P-i-n solar cell configuration and photo-excited carriers drifted by the built in electric field inside i layer	5
Figure 1-4	Structure of nc-Si:H deposited with a variation of hydrogen dilution	7
Figure 1-5	Absorption coefficient of crystalline silicon, nanocrystalline silicon and amorphous silicon	8
Figure 2-1	Schematic of a typical PECVD Chamber	12
Figure 2-2	Capacitive Coupled RF Discharge	13
Figure 2-3	Cross Section of electron and SiH ₄ collision with two different EEDF: black dash curve with less distribution in high electron energy compared with red curve	15
Figure 2-4	Silicon thin film deposition process by PECVD	17
Figure 2-5	Scheme of Silicon Film Growth	18
Figure 2-6	Diagram of Energy Level of radicals for Optical Emission inside plasma	20
Figure 2-7	Typical OES spectrum from pure SiH ₄ discharge	21
Figure 2-8	Optical Emission Spectroscopy Apparatus at IEC	22
Figure 2-9	Current-Voltage measurement by Langmuir Probe.....	23
Figure 2-10	EEDF calculated by Equation 2-9 for a Ar Plasma measured at IEC.....	25
Figure 2-11	Hidden Analytical Langmuir Probe installed in PECVD chamber at IEC.....	26
Figure 3-1	Schematic of in-line multichamber PECVD system at IEC	28

Figure 3-2	Six Chamber in-line PECVD system at IEC	29
Figure 3-3	Transmission and Reflection of a-Si:H film on glass substrate.....	31
Figure 3-4	Tauc Plot of a-Si:H film deposited by PECVD at IEC.....	32
Figure 3-5	Schematic Diagram of Michelson Interferometer for FTIR	33
Figure 3-6	Nicolet 6700 FT-IR Spectrometer by Thermo Scientific	34
Figure 3-7	FT-IR spectra of a-Si:H thin film and Si-H bond analysis	36
Figure 3-8	Energy of Raman Scattering light.....	37
Figure 3-9	Raman Spectra of Crystal Silicon, Nanocrystalline Silicon and Amorphous Silicon.....	38
Figure 3-10	Three Peak Devolution of nc-Si:H layer Raman Spectrum leading to a crystalline fraction $X_C=65\%$	40
Figure 3-11	Scheme of X-Ray Diffraction	41
Figure 3-12	XRD Spectrum of nc-Si:H with $X_C=67\%$ and 46% , color in red and black respectively	41
Figure 3-13	Standard Solar Cell J-V curve and power output as a function of voltage	43
Figure 3-14	Apparatus of Solar Cell J-V measurement	43
Figure 4-1	Variation of growth rate as a function of RF power at 200°C , 0.5 Torr without H_2 dilution	48
Figure 4-2	FTIR results microstructure factor R_{mf} at 200°C , 0.5 Torr without H_2 dilution.....	49
Figure 4-3	Variation of growth rate as a function of RF power at 200°C with deposition pressure of 1.25 Torr.....	51
Figure 4-4	Variation of growth rate as a function of RF power at 200°C with deposition pressure of 2.5 Torr.....	52
Figure 4-5	FTIR results of R_{mf} for a-Si:H films on c-Si.....	53
Figure 4-6	FTIR results of H content for a-Si:H films on c-Si	54

Figure 4-7	Tauc plots of a-Si:H i layers on glass at different deposition conditions.....	55
Figure 4-8	FTIR Spectra of a-Si:H deposited at 200 °C and 250 °C.....	57
Figure 4-9	Hydrogen desorption reaction at a-Si:H growth surface	58
Figure 4-10	Tauc Plot of a-Si:H deposited at 200 °C and 250 °C.....	59
Figure 4-11	Light JV curves for devices with and without 10% Si ₂ H ₆ additive.....	60
Figure 4-12	QE curves for devices with and without 10% Si ₂ H ₆ additive.....	61
Figure 4-13	QE curves of devices with 200 °C and 250 °C i layer, before light soaking.....	63
Figure 5-1	Growth Rate and X _c of films deposited with variable H ₂ /SiH ₄ Dilution..	71
Figure 5-2	Raman Spectra of Si films deposited with different SiH ₄ flow at H ₂ =500 sccm 3 Torr and RF power of 300W. The H ₂ /SiH ₄ ratio varied from 71 to 36.	72
Figure 5-3	Growth Rate and X _c of Si films deposited at different RF power at H ₂ /SiH ₄ =500/7, 3 Torr.....	73
Figure 5-4	Growth Rate and X _c of Si films deposited at different Pressure at H ₂ /SiH ₄ =500/8.5,RF 515W	75
Figure 5-5	Growth Rate and Raman X _c of nc-Si:H deposited by VHF as a function of H ₂ /SiH ₄ ratio	77
Figure 5-6	Raman Spectra of nc-Si:H deposited by H ₂ /SiH ₄ with and without Si ₂ H ₆	78
Figure 5-7	Raman Spectra of nc-Si:H deposited by HWCVD and PECVD with similar X _c	81
Figure 5-8	XRD Spectra of nc-Si:H deposited by HW-CVD and PECVD	82
Figure 5-9	XRD pattern of nc-Si:H deposited at different pressure by RF 515W	83
Figure 5-10	Raman spectra of nc-Si:H film at 3 Torr and 8 Torr by RF 515W	85
Figure 5-11	XRD pattern of nc-Si:H films different dilution at 8 Torr H ₂ =300sccm by RF 515W	86

Figure 5-12	XRD pattern of nc-Si:H by RF and VHF at 3 Torr with different SiH ₄ flow	87
Figure 5-13	XRD pattern of nc-Si:H deposited by RF and VHF with and without Si ₂ H ₆	89
Figure 5-14	Nc-Si:H p-i-n solar cell configuration	90
Figure 5-15	XRD pattern of nc-Si:H solar cell on Glass, Z-TEC8 and AZO	92
Figure 5-16	AMF Tilt Top View of AZO and Z-TEC8 surface prior to any nc-Si:H film deposition.....	94
Figure 5-17	AFM line scan profile of AZO and Z-TEC8	95
Figure 5-18	QE of nc-Si:H solar cells on Z-TEC8 and AZO	96
Figure 5-19	QE Comparison of the nc-Si:H solar cell fabricated on AZO with Al Back Reflector and ITO/Ag Reflector.....	98
Figure 5-20	JV curve of nc-Si:H solar cell on AZO with ITO/Ag back reflector.....	98
Figure 6-1	Experimental Apparatus of OES and Langmuir Probe.....	103
Figure 6-2	OES of SiH ₄ /H ₂ plasma for a typical a-Si:H deposition condition.....	104
Figure 6-3	OES Spectra of a-Si:H deposition plasma at 0.5 Torr, 30W without H ₂ dilution comparing pure SiH ₄ and 10% Si ₂ H ₆ in SiH ₄	106
Figure 6-4	Growth Rate vs. SiH* intensity normalized to the lowest SiH* intensity for each series	107
Figure 6-5	OES H α emission intensity at 656 nm and SiH* emission intensity at 414 nm as a function of RF power at 1.25 Torr	109
Figure 6-6	SiH* emission intensity at 414 nm as a function of Si ₂ H ₆ fraction and RF power	110
Figure 6-7	Ionization Cross Section Comparison of SiH ₄ and Si ₂ H ₆ , with EEDF curve in blue for eye guide	112
Figure 6-8	Ratio of H α /SiH* as a function of RF power with and without H ₂ dilution	113
Figure 6-9	Normalized OES Spectra of a-Si:H and nc-Si:H deposition plasma.....	114

Figure 6-10 OES SiH* and H α as a function of SiH ₄ flow with H ₂ 450 sccm at 3 Torr with RF power 250W	115
Figure 6-11 OES SiH* and Growth Rate by RF (left) and VHF (right)	116
Figure 6-12 OES H α /SiH* and Raman X _c by RF(left) and VHF (right)	117
Figure 6-13 OES SiH* and H intensity as a function of pressure with SiH ₄ /H ₂ =8.5/500, RF Power 515W	119
Figure 6-14 OES SiH* and H α /SiH* as a function of RF Power for nc-Si:H deposition SiH ₄ /H ₂ =7/300 at 3 Torr	120
Figure 6-15 Langmuir Probe Results: EEDF at different pressure with RF Plasma.....	122
Figure 6-16 Langmuir Probe Results: Electron Density at different Pressure with RF Plasma.....	123
Figure 6-17 Langmuir Probe Results: Mean Electron Energy at different Pressure with RF Plasma.....	124
Figure 6-18 Langmuir Probe Results: Sheath Potential at different Pressure with RF Plasma.....	125
Figure 6-19 Electron Density, both total and that with energy larger than SiH* excitation threshold, as a function of Pressure	127
Figure 6-20 EEDF of RF plasma at different Power	128
Figure 6-21 Normalized EEDF by RF and VHF Plasma, normalized to unity integrated area	129
Figure A-1 Normalized Stability of 3 devices: baseline; higher growth temperature; H ₂ dilution	143

ABSTRACT

Hydrogenated amorphous Si (a-Si:H) and nano-crystalline silicon (nc-Si:H) thin films with unique properties have provoked wide research interest and technology applications for thin film silicon solar cells, and active layer in thin film transistors for liquid crystal display. The technologies investigated for both a-Si:H and nc-Si:H thin film preparation have included Sputtering, Hot Wire Chemical Vapor Deposition (HWCVD), Photochemical-CVD and Plasma Enhanced CVD (PECVD). Of these, PECVD is the most recognized and utilized technology for high quality, low temperature and large area thin film deposition. The effect of PECVD silicon thin film growth condition on the film properties, device performance and the plasma characterization need to be deeply understood.

This dissertation analyzes the growth rate and material properties of thin film silicon at different plasma excitation frequencies and gas compositions by PECVD based on *in-situ* Plasma Diagnostics by Optical Emission Spectroscopy (OES) and Langmuir Probe. A relatively unique aspect of this research is evaluating the effect of adding a small amount of higher order silane gas to catalyze decomposition of the dominant silane species to enhance the growth rate.

It has been found that the addition of 1.7% Si₂H₆ flow into SiH₄/H₂ mixture increased the a-Si:H growth rate by 60%. The optimization of a-Si:H deposition

utilizing the $\text{SiH}_4/\text{Si}_2\text{H}_6/\text{H}_2$ mixture resulted in films grown at high rate and power with low microstructure factor which correlates with better stability of a-Si:H. The process window for transition from a-Si:H to nc-Si:H deposition was increased at higher H_2/SiH_4 ratio and large grain size was achieved at either high pressure for RF 13.56 MHz or low pressure for Very High Frequency (VHF) 40.56MHz discharge.

Si films grown at high H_2/SiH_4 ratio or RF power, corresponding to a higher $\text{H}\alpha/\text{SiH}^*$ intensity ratio, have lower microstructure factor (R_{mf}) from Fourier Transform Infrared Spectroscopy for a-Si:H and higher fraction crystallinity (X_c) from Raman spectroscopy for nc-Si:H films, respectively where the growth rate is proportional to the electron density of the plasma analyzed by Langmuir Probe. The plasma Electron Energy Distribution calculated through Druyvesteyn Method indicates an increase of high energy electron percentage at higher RF power, resulting in larger H_2 dissociation level for higher $\text{H}\alpha/\text{SiH}^*$ detected by OES. The high energy electron density and plasma potential is decreased at higher process pressure, resulting in less ion-surface bombardment and larger grain size formation of nc-Si:H film. Comparing RF with VHF plasma, the VHF plasma had one order of magnitude higher electron density leading to better H_2/SiH_4 utilization.

An a-Si:H solar cell with initial efficiency of 7.4% was fabricated with intrinsic layer deposited from $\text{SiH}_4/\text{Si}_2\text{H}_6/\text{H}_2$ discharge at a high growth rate of $>5\text{\AA}/\text{s}$ and the stabilized performance after light soaking was similar with the baseline cells grown at $1.8\text{\AA}/\text{s}$. nc-Si:H solar cell with efficiency of 4.5% was obtained with a growth rate of $4\text{\AA}/\text{s}$ by $\text{SiH}_4/\text{Si}_2\text{H}_6/\text{H}_2$ discharge.

Chapter 1

INTRODUCTION

1.1 Research Motivation

Nowadays, the world's major source of energy is from by the fossil fuel such as coal, oil and natural gas. However, these energy sources are facing more and more challenges where fossil fuels are nonrenewable and their prices keep increasing till the final depletion predicted in 2055 [1]. The fossil fuel consumption also results in environmental concern due to the large amount of CO₂ emission into the atmosphere, which is considered a major reason for global climate warming. People have started to seek the renewable energy sources with guaranteed supply which are environmentally friendly, such as hydro, wind, tidal and solar energy.

Photovoltaic (PV) technology converts solar radiation to electricity with solar cell device. It has been considered as a promising solution for future energy since the sunshine is unlimited and there is no CO₂ emission during the energy generation. PV was first developed for space satellite power supply in 1960s and now PV system can deliver electricity to both off grid individual units and grid-connected systems.

According to the newly released data shown in Figure 1-1, 4751 Mega Watts of PV capacity was installed in 2013 worldwide which is an increase of 41% over record increase in 2012 [2]. In 2013, new PV installations exceeded wind and became the

second largest source among the new electricity generating capacity in US, as shown in Figure 1-2. PV installations are predicted to keep increasing in 2014. However, the PV price is relatively expensive compared with other commercial electric sources although the price has fallen significantly in the past 5 years. There are two ways to make PV more cost effective in terms of the standard metric of dollars per watt of PV power produced: reducing the cost per module or increasing the efficiency per module. Thus, PV researchers have been focused on increasing PV module efficiency while reducing production cost.



Figure 1-1 U.S PV installations and System Price [2]



Figure 1-2 New electricity Generation Capacity in US, 2012 vs 2013 [2]

Currently the world solar market is dominated by the crystal silicon based solar modules, which are fabricated from either mono- or multi-crystalline silicon wafers. The thin film solar modules based on hydrogenated amorphous silicon (a-Si:H) and nanocrystalline silicon (nc-Si:H) technology have the potential for reducing the cost per watt for the solar market. Compared with crystalline silicon based solar cell, the thin film silicon has significant less material consumption. The typical thickness of silicon layer in a thin film solar cell is less than 2 μ m, compared with the crystal silicon solar cell ~150 μ m. Moreover, the manufacturing of silicon wafers requires a large amount of thermal energy where processing temperatures are >1300 °C for 200 to 300 cm diameter wafers. The a-Si:H and nc-Si:H films can be deposited at much lower temperature, ~200 °C by Plasma Enhanced Chemical Vapor Deposition (PECVD) technology on on low cost substrate, such as glass, plastic [3] or metal foils [4]. Thin

film silicon technology has become an attractive approach to reducing the PV cost in future.

The operation of the solar cell starts with the absorption of a solar photon leading to the generation of an electron and hole pair and their subsequent separation and collection. The electron and hole generated by the incident light must have a long lifetime to be spatially separated for contribution to net current. The typical solar cell includes p-type and n-type materials used to create a p-n junction, such as c-Si, CuInGaSe, CdTe based solar cell [5]. The a-Si:H and nc-Si:H based solar cell can't be operated with stacking p type and n type material since they are so defective and the carriers have an insufficient mobility and lifetime to be collected. The a-Si:H and nc-Si:H based solar cell consists of three layers - a p type, intrinsic (i-layer), and a n type - forming a p-i-n or n-i-p configuration. The p type and n type layers are very thin with typical thickness ~20nm. The intrinsic layer needs to be much thicker, ~ 200 to 400 nm, to absorb light for carrier generation. The electron and holes drift in the built-in electric field to the n type and p type layers, respectively, thus contributing to the current. Figure 1-3 shows a p-i-n solar cell configuration and carrier drifting.

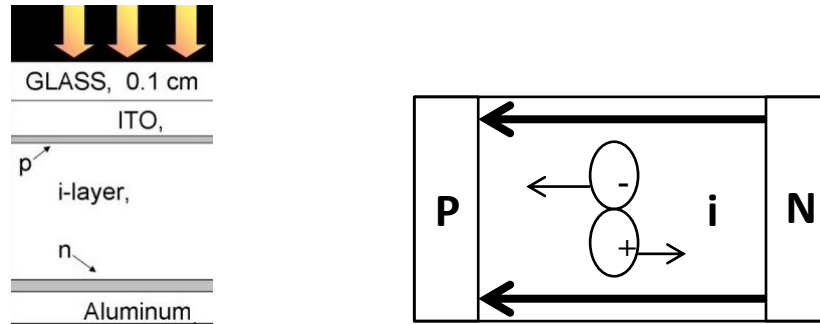


Figure 1-3 P-i-n solar cell configuration and photo-excited carriers drifted by the built in electric field inside i layer

The first single junction a-Si:H based solar cell was reported with 2.4% efficiency by David Carlson and Christopher Wronski in 1974 [6]. Nowadays, the best Si thin film research cell efficiency is a triple junction structure had been reported LG with a stabilized (after light soaking) efficiency 13.4% [7].

However, one serious problem which limits the a-Si:H solar cell application is the stability. The performance of a-Si:H solar cell degrades while exposing to light, which is known as Staebler-Wronski effect [8]. The light exposure results in changes in properties of the a-Si:H such as increase of defects density and reduction of photoconductivity which degrades device performance. The light induced defects become recombination centers resulting shorter carrier lifetime, and suppress the electric field inside the i layer which reduces the carrier collection performance.

The a-Si:H stability improvement has attracted intense research. The light induced degradation in a-Si:H is strongly correlated with the hydrogen concentration and di-hydride (Si-H₂) concentration in the i a-Si:H where higher hydrogen content and Si-H₂ bond density results larger light induced degradation [9, 10]. The hydrogen

content and Si-H₂ bond density are in turn influenced by the deposition condition. Previous studies using Hot-Wire deposition technique [11], ECR deposition [12] or PECVD with high hydrogen dilution [13] have shown a reduction in the hydrogen content and Si-H₂ density for a-Si:H resulting in improve the stability. Overall, the deposition technology for optimized stability and high growth rate a-Si:H is one of the major research motivation for a-Si:H solar cell application.

Nanocrystalline silicon, nc-Si:H, which is a phase between crystalline silicon and amorphous silicon, is another attractive material for thin film Silicon solar cell application. The structure of nc-Si:H is considered as nano-sized crystalline silicon passivated in the a-Si:H matrix with a mixture of crystalline silicon, amorphous silicon and grain boundaries. It has a lower bandgap hence absorbs light at lower energies compared to a-Si:H. nc-Si:H can be deposited by similar technique as a-Si:H but under different deposition conditions. The gas phase hydrogen-to-silane ratio, called the Hydrogen dilution, and the substrate temperature control the transition from an amorphous phase to nanocrystalline silicon phase. nc-Si:H is much more stable under light exposure compared with a-Si:H, and thus became an attractive material as absorption layer in p-i-n solar cell. In 1996, J. Meier reported a nc-Si:H solar cell with 7.7% efficiency which led to an expansion in the research activity on nc-Si:H application. By stacking a-Si:H top cells and nc-Si:H bottom cells, a micromorph tandem solar cell [14], a initial efficiency of 14.7% has been reported by Yamamoto in 2004 [15]. Several companies have reported full size (1.4 m²) micromorph modules having stabilized (after light soaking) efficiencies > 10%.

The solar cell performance highly depends on the structural properties of the nc-Si:H film and the best solar cell are fabricated from intrinsic nc-Si:H films deposited near the amorphous/nanocrystalline transition regime [16]. It has been reported that the optimized nc-Si:H cell performance is obtained with (220) orientated film with grain size around 25nm with a-Si:H passivated [17]. Figure 1-4 shows variable nc-Si:H structure deposited by the different gas mixture [18]. Understanding the process conditions and correlating them with the material properties became a critical topic for nc-Si:H research.

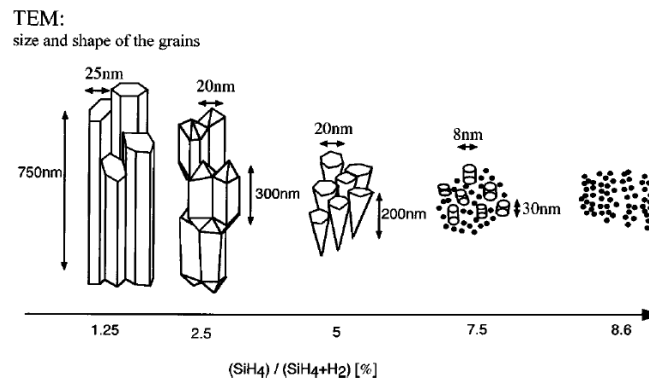


Figure 1-4 Structure of nc-Si:H deposited with a variation of hydrogen dilution [18]

nc-Si:H is an indirect bandgap material similar to crystalline silicon and the absorption coefficient in solar spectrum is relatively low compared with a-Si:H. Therefore a much thicker nc-Si:H layer, compare with a-Si:H, is necessary to absorb sufficient light for carrier generation. Figure 1-5 presents the absorption coefficient comparison between crystal, nanocrystalline and amorphous silicon [19]. While the optimum i-layer thickness requirement for p-i-n solar cell applications depends on

light trapping, relative stability, and other material specific parameters, typically the top a-Si:H cell is around 300 nm while the bottom nc-Si:H is around 2000 nm thick. The typical deposition rate for high quality silicon film is 1Å/s for a-Si:H and 2Å/s for nc-Si:H. The nc-Si:H i layer deposition with ~3hrs limits the mass production of nc-Si:H. Thus the development of high growth rate of high quality nc-Si:H is crucial for solar cell applications. The current approaches for high growth rate includes high pressure depletion, Very High Frequency (VHF >13.56 MHz) PECVD technique and growth rate enhancement by gas phase additive into plasma discharge [20, 21, 22].

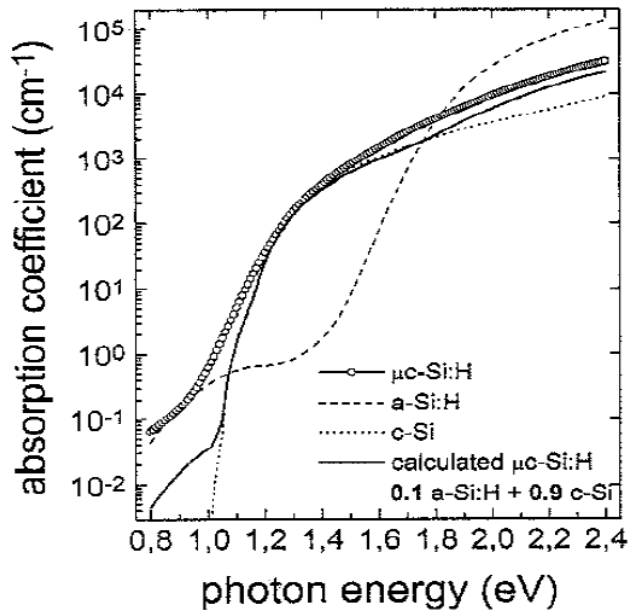


Figure 1-5 Absorption coefficient of crystalline silicon, nanocrystalline silicon and amorphous silicon [19]

The technologies investigated for both a-Si:H and nc-Si:H thin film preparation have included Sputtering, Hot Wire Chemical Vapor Deposition (HW-CVD), Photochemical-CVD and Plasma Enhanced CVD (PECVD). Of these,

PECVD is the most utilized recognized technology for high quality, low temperature and large area thin film deposition. The PECVD process is based on creating a plasma discharge in a gas mixture of silane or disilane with hydrogen. The deposition condition strongly affects the quality of Si thin film for both structure and optoelectronic properties. Decades of research have shown that the PECVD process conditions, e.g. Gas Mixture, RF Power and Frequency, Pressure, influence the growth and material properties, e.g. growth rate, Si-H bond, band gap, crystalline volume fraction and growth orientation [17, 23, 24]. Intensive research has been carried out to understand the relation between PECVD Si thin film growth mechanism and material properties. For insight of film growth, the deposition conditions determines the plasma properties such as gas phase composition of film precursor species like SiH_3 , H radical density, electron density and electron energy distribution [25, 24]. The a-Si:H and nc-Si:H material properties are strongly influenced by the plasma parameters. The characterization and correlation of the deposition parameters, film properties and plasma diagnostics is critical to optimize the silicon thin film technology application.

1.2 Thesis Outline

The work presented in this thesis focuses on the deposition of silicon thin film by PECVD, characterization of the plasma in-situ, characterization of the material and solar cell device properties, and then correlating those properties with the plasma parameters. The topics covered in the chapters are:

- Chapter 2 describes fundamental background of plasma enhanced chemical vapor deposition which includes the basic mechanism of film deposition and plasma discharge. The plasma diagnostic methods for PECVD are also introduced.
- Chapter 3 describes the material characterization techniques for a-Si:H and nc-Si:H structural properties and the device fabrication and characterization.
- Chapter 4 presents correlates the a-Si:H process conditions with material properties and device performance. This chapter focuses on understanding disilane as gas additive for a-Si:H growth rate enhancement as well as the effect on material and device properties.
- Chapter 5 discusses the deposition of nc-Si:H films and their material characterization including the correlation between process parameter and critical material properties for device performance.
- Chapter 6 focuses on the PECVD plasma characterization. The relationship between process condition, material properties and plasma characterization are presented.
- Chapter 7 summarizes the conclusions of the thesis followed by a brief outlook for future research.

Chapter 2

FUNDAMENTAL OF PLASMA ENHANCED CHEMICAL VAPOR DEPOSITION AND PLASMA DIAGNOSTICS

2.1 Fundamental of Plasma Enhanced Chemical Vapor Deposition

PECVD typically uses the plasma produced at low pressure (glow discharge). The free electrons are accelerated by electric field from a bias voltage to gain sufficient kinetic energy. The collision between energetic electron and gas molecules results the processes of excitation, ionization, dissociation as well as attachment. The plasma used for PECVD contains ions, electrons and a variety of neutral species in both ground and excited states. The average electron energy is several electron volts while the ion (or neutral) energy is at least two orders of magnitude less. The plasma generated by the electric field at low temperature is called "cold" plasma in nonequilibrium state, which is unlike the equilibrium "thermal" plasma at high temperature. The various reactive species inside glow discharge, which results from the ionization and dissociation of feed gas from electron impact, allows the opportunity to process materials at a low temperature $<400\text{ }^{\circ}\text{C}$. Without a plasma, typical thermal processes require much higher temperature $> 900\text{ }^{\circ}\text{C}$ to dissociate the gases [26]. The species from gas dissociation by plasma diffuse to the substrate followed by surface reactions for film formation. Figure 2-1 shows a typical schematic of PECVD chamber [5].

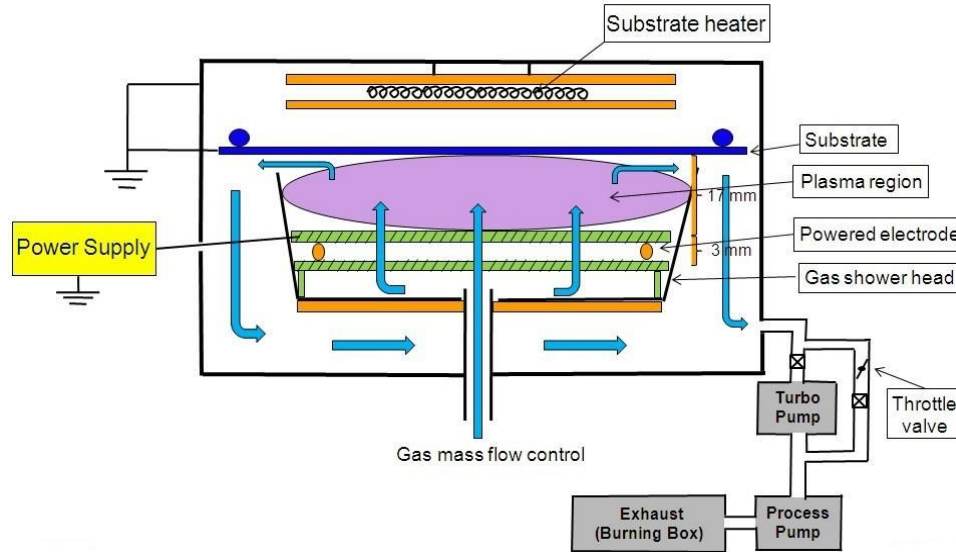


Figure 2-1 Schematic of a typical PECVD Chamber [5]

2.1.1 Plasma Discharge in PECVD System

The physics and chemistry in glow discharge is very complicated. In general, the PECVD process includes electron and molecule impact, formation of radicals, creation of various charged or neutral species inside plasma, followed by diffusion to substrate and Surface Reaction. Figure 2-2 presents typical scheme of capacitive coupled RF plasma powered by bias voltage V_b , with electron and ion densities (n_e , n_i) as well as the plasma potential (V_{pl}) distribution [27]. The plasma bulk includes large amount of electrons, positive ions, negative ions and neutrals. The electrons diffuse to the electrode or grounded surface leaving the plasma bulk with relatively positive potential. The electric field with direction from plasma bulk to surfaces creates a plasma sheath to reflect the electron back to plasma bulk and maintain the plasma discharge. The positive ions are accelerated by the plasma potential towards the electrode or grounded substrate resulting surface bombardment.

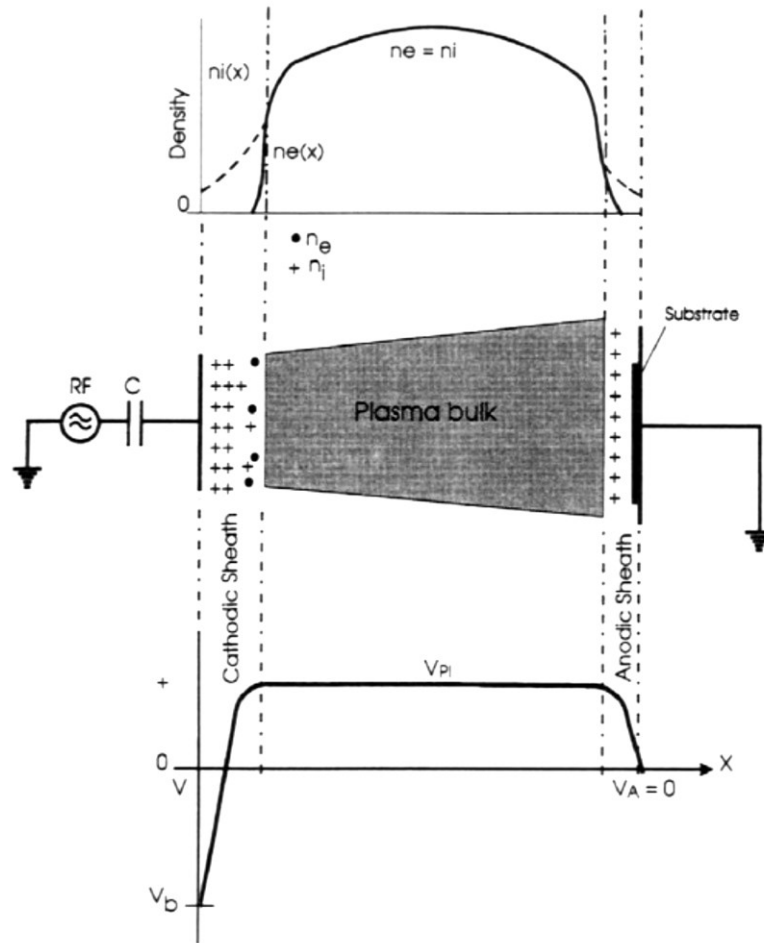


Figure 2-2 Capacitive Coupled RF Discharge [27]

Inside the plasma bulk, electrons gain energy accelerated by the electric field and the energy transfer from high energy electrons to molecule and radicals during the collision. The impact reaction results in the inelastic collision including dissociation, ionization and excitation as shown in Table 2-1:

Table 2-1 Electron and Molecule interaction inside PECVD plasma [27]

Interaction Type	Electron and Molecule Reaction
Dissociation	$e+AB \rightarrow A+B+e$
Ionization	$e+AB \rightarrow AB^++2e$
Dissociative Ionization	$e+AB \rightarrow A^++B+2e$
Attachment	$e+AB \rightarrow AB^-$
Dissociative Attachment	$e+AB \rightarrow AB^- \rightarrow A^-+B$
Recombination	$e+A^+ \rightarrow A$
Vibrational Excitation	$e+AB(v) \rightarrow e+AB(\omega)$
Electric Excitation	$e+AB \rightarrow AB^*+e$
Dissociative Excitation	$e+AB \rightarrow A^*+B+e$

while v and ω are the vibrational quantum numbers.

The electron and molecule/radical interaction is characterized by a collision cross section σ , which is a function of electron energy describing the probability of impact. The reaction rate $k(E)$ of the electron collision is a function of electron energy distribution function (EEDF) $f(E)$ and cross section $\sigma(E)$ as shown:

$$k(E) = \int_{threshold} \sqrt{E} \cdot f(E) \cdot \sigma(E) dE \quad (2-1)$$

The excitation and dissociation generally requires the electron energy around several electron volts (eV) while ionization of molecules normally requires electron energy >10 eV. Figure 2-3 presents cross section for electron impact on SiH_4 gas with electron energy distribution curve for a device grade a-Si:H growth condition [28].

The reaction rate highly depends on the overlap of EEDF and $\sigma(E)$ area. Due to lower threshold energy, the dissociation reaction rate is higher than the ionization rate, resulting typical neutral species density/charge density ratio in the range $\sim 10^4$ to 10^7 .

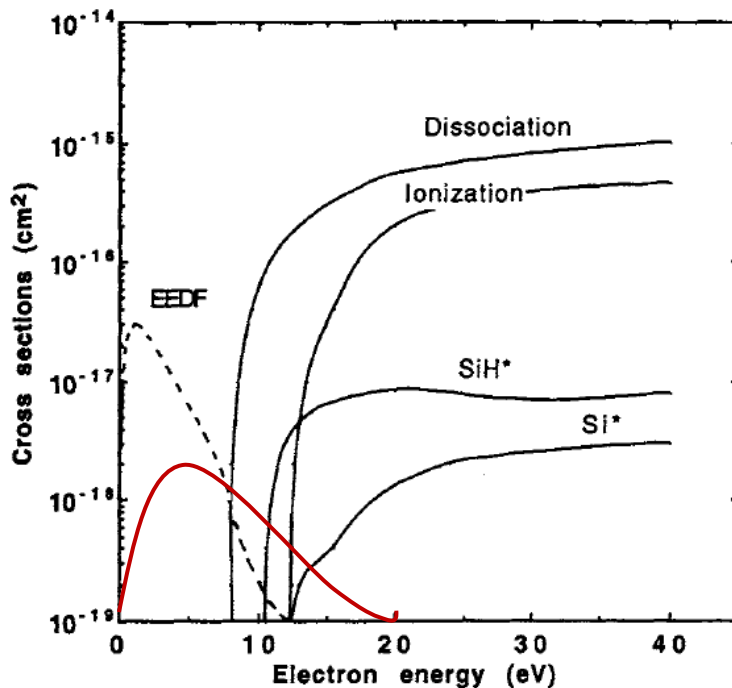


Figure 2-3 Cross Section of electron and SiH₄ collision with two different EEDF [28]: black dash curve with less distribution in high electron energy compared with red curve

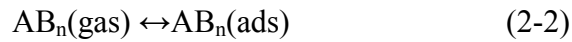
Figure 2-3 also highlights the electron energy overlap region of EEDF and molecule dissociation/ionization cross section, which dominates the reaction rate for variable radical generation based on Equation 2-1. Moreover, the ratio of the reaction rate for different radical could be determined by the EEDF. For example, the EEDF with red curve shown in Figure 2-3 results larger reaction ratio of Si*/SiH* compared with the black dash curve. EEDF is one of the most important plasma parameter to understand the discharge mechanism. Typically the electron energy distribution results from energy loss by impact and energy gain by electric field acceleration

simultaneously. Langmuir Probe has been used to characterize the relationship between EEDF and plasma process conditions, which will be introduced later.

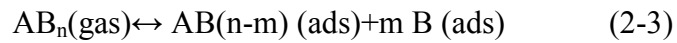
2.1.2 Plasma and substrate surface interaction in PECVD

The species generated from plasma diffuse to the substrate result in the complex interactions such as physical or chemical adsorption, desorption, surface reaction process and surface ion bombardment.

The molecule or fragments undergoes adsorption on surface which can be presented as:



The species on the surface can be also produced by a chemisorption process as:



Once adsorbed, the surface species would react with each other or with radicals in gas phase. The reaction 2-2 and 2-3 typically results in materials being deposited on the substrate. In addition, the energetic particle bombardment on surface, either by ions or electrons, can break chemical bonds and create adsorption for material formation [29]. Meanwhile the weakly bonded surface species could also react with gas phase radicals followed by a desorption resulting in the material etching from substrate. The material structural and electrical properties are strongly affected by the complex reactions at the film forming surface.

2.1.3 PECVD Silicon thin film growth mechanism

SiH₄ based discharge is the most common method used for silicon thin film PECVD growth. The Deposition process could be described by the scheme shown in Figure 2-4.

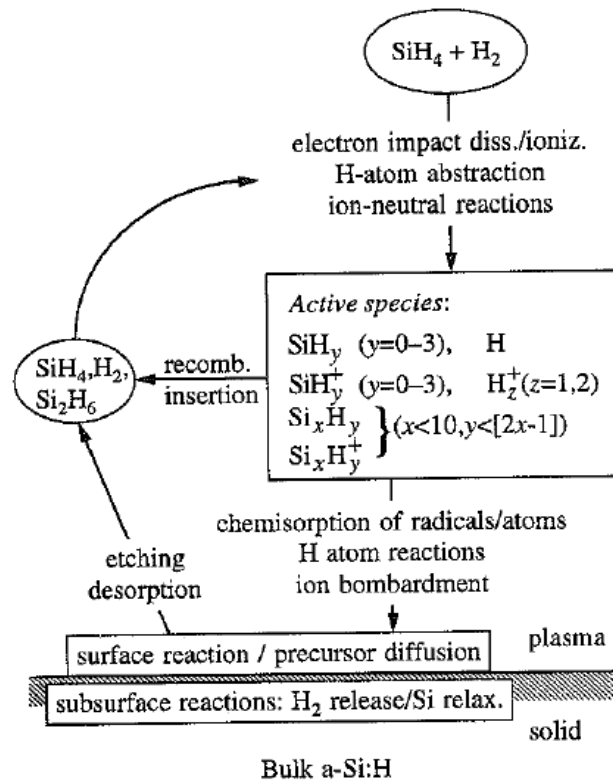
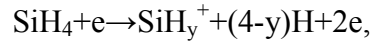


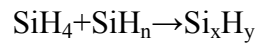
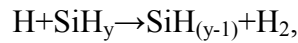
Figure 2-4 Silicon thin film deposition process by PECVD [30]

The Si thin film PECVD growth could be summarized as the following steps: First, the electron and SiH₄ molecule collide with each other inside the plasma consisting of positive and negative ions, electrons as well as neutral radicals and molecules, followed by the secondary reaction to form other silicon based radicals and ions.

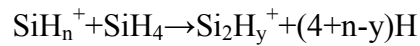
I. Electron-molecule interaction:



II. Neutral interaction:



III. Ion-Molecule interaction:



The species inside plasma bulk diffuse to substrate for thin film formation. It has been widely reported that a-Si:H with good electric properties is grown by discharge with SiH_3 as dominant radical impinging on the substrate due to its long lifetime [31]. The surface silicon dangling bonds are formed by either ion bombardment breaking weak Si-Si bond or surface H desorption from Si-H bond. The Si- dangling bond is attached by $-\text{SiH}_3$ with Si-Si bond forming silicon network, as shown in Figure 2-5 reported by W.M.M. Kessels.

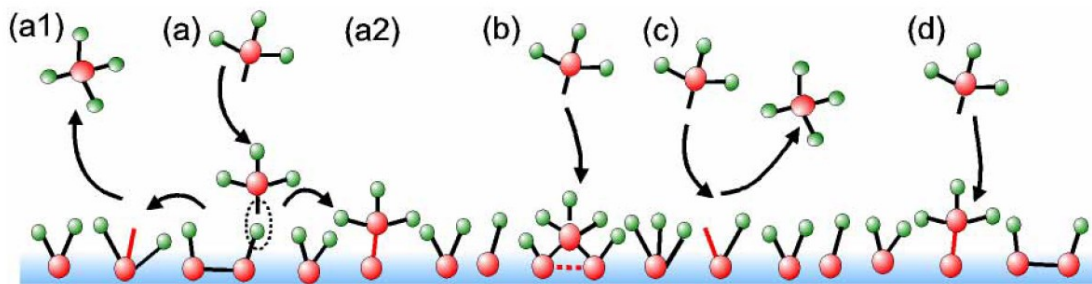


Figure 2-5 Scheme of Silicon Film Growth [32]

Nowadays, the PECVD process mechanism is still under research, which focused on dominated growth species and species reaction on substrate surface.

2.2 Plasma Diagnostic

The plasma in PECVD is a complicated reactive system including not only electron-molecule collisions, but also a series of secondary reactions among neutrals, radicals and ions. Plasma diagnostic technologies have been applied to understand the discharge mechanism and kinetics. In this thesis, Optical Emission Spectroscopy and Langmuir Probe are used to characterize the optical and electric properties of the plasma for insight of the PECVD process.

2.2.1 Optical Emission Spectroscopy

Optical Emission Spectroscopy (OES) is powerful and relatively simple technique which measures the wavelength-resolved emission signal from the plasma. Figure 2-6 indicates the mechanism of Optical Emission inside plasma [33]. The atom A at ground state is excited to excitation state A* through electron impact, followed by relaxation to a lower state A_f accompanied by subsequent photon emission with frequency ω. The emission wavelength is defined as

$$\lambda = \frac{2\pi c}{\omega}, \omega = E_{A^*} - E_f \quad (2-4)$$

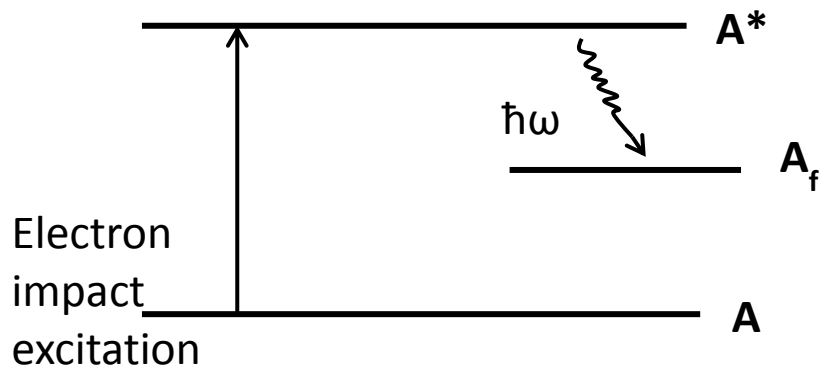


Figure 2-6 Diagram of Energy Level of radicals for Optical Emission inside plasma

The intensity of the emission from ground state A is written as:

$$I_{\lambda} = \alpha_{\lambda A} \cdot n_A \quad (2-5)$$

where

$$\alpha_{\lambda A} = k_D(\lambda) \int_0^{\infty} 4\pi v^2 dv Q_{A^*} \sigma_{\lambda A}(v) v f_e(v) \quad (2-6)$$

f_e is electron density with energy distribution function, $\sigma_{\lambda A}$ is cross section of excitation of A by electron impact, k_D is the detector response constant, Q_{A^*} is quantum yield for photon emission and $Q_{A^*} \approx 1$ for low pressure discharge and excited states with short lifetime. Equations 2-5 and 2-6 indicate the optical emission intensity is a function of energy dependent electron $f_e(v)$ and radical density n_A inside plasma. Therefore, the OES measurement provides qualitative information of the electron and radical density of the discharge.

Figure 2-7 is the OES spectrum collected from pure SiH_4 discharge reported by A. Matsuda [34]:

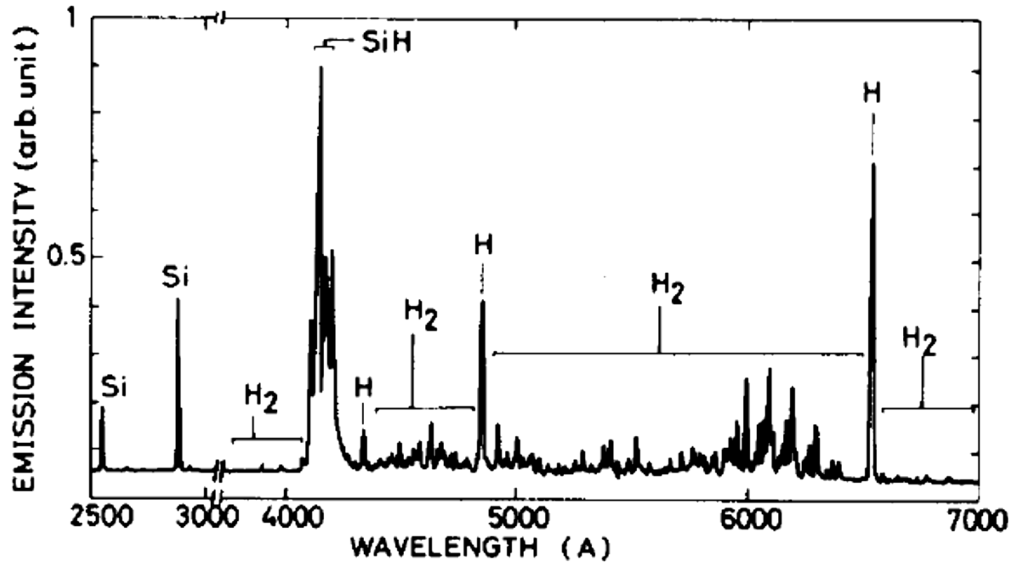
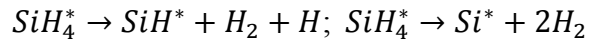
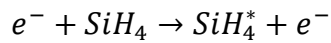


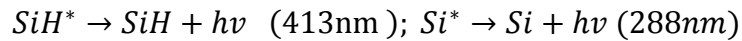
Figure 2-7 Typical OES spectrum from pure SiH₄ discharge [34]

The commonly monitored emission lines include Si* at 288 nm (UV 43 transition), SiH* at 413 nm (A²Δ-X2Π of SiH), H_α at 656 nm (3d²D-2p²p^o of hydrogen), H_β at 486 nm (4d²D-2p²p^o of hydrogen).

As an example for the formation of SiH* and Si*, the SiH₄ molecule is excited by the electron collision:



The excited state SiH* and Si* decay to lower state producing radiative emission:



The OES measurement is used to qualitatively correlating the growth rate and material properties with electron density and dissociation from electron collision at different energy.

Figure 2-8 shows the apparatus of OES used in this thesis.

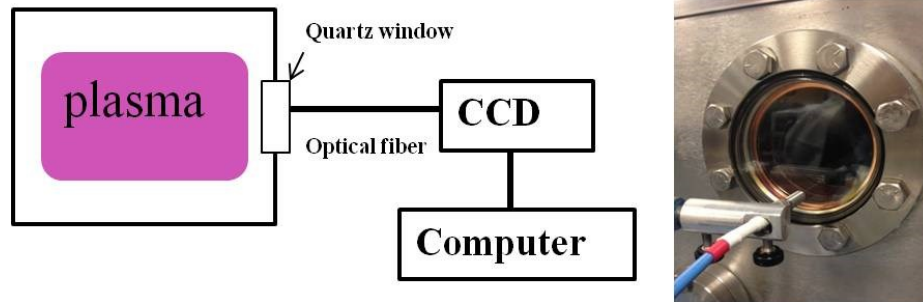


Figure 2-8 Optical Emission Spectroscopy Apparatus at IEC

2.2.2 Langmuir Probe

Langmuir Probe is used to measure current and voltage of the discharge and it is one of the most useful tools for plasma diagnostic. The Langmuir probe is a metal probe, commonly using Tungsten with high melting point, inserted in discharge and biased with positive and negative voltage to draw electron or ion current. The probe inside plasma is surrounded by a sheath with dimension of the Debye Length λ_d [35]. The Debye Length of the plasma for PECVD application is $\sim\mu\text{m}$ and the diameter of the probe normally $\sim\text{mm}$, so there is only minor local disturbance of the plasma by probe inserted.

The current -voltage curve measured by the Langmuir Probe can be analyzed to determine the electrical properties of the plasma such as electron density (n_e), mean electron temperature (T_e), plasma potential (V_p), floating potential (V_f) and Electron Energy Distribution Function (EEDF).

Figure 2-9 shows a typical current - voltage curve of plasma measured by Langmuir Probe [33]. Table 2-2 lists different region to interpret physics of the Langmuir Probe measurement. When probe voltage $V=V_p$, the probe has same potential as the plasma and collects the electron and ions random flux onto probe surface. The current collected is more attributed by more mobile electron. Further increasing the probe voltage, the probes work in electron saturation region to collect saturated current. However, the collected current keeps increasing with voltage due to larger collection area. When probe voltage $V < V_p$, the electron is repelled until $V=V_f$ while electron and ion flux to probe surface are equal when $I=0$. When probe voltage $V \ll V_f$, the current collected by probe is attributed by the positive ion. The current also increase with more negative bias voltage of the probe due to change of collection area.

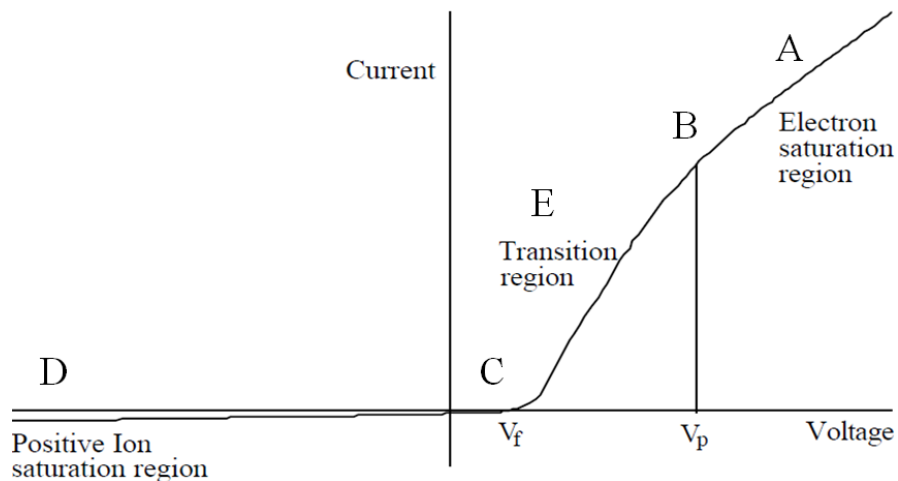


Figure 2-9 Current-Voltage measurement by Langmuir Probe

Table 2-2 Summary of variable Voltage Region for Langmuir Probe data Interpretation

Bias Voltage Region	Current collected by Probe
A: $V > V_p$	Draw electron and negative ions from plasma
B: $V = V_p$	Collecting electron and ions by random collision
C: $V = V_f$	No current collected , probe insulated
D: $V \ll V_p$	Draw positive ions from plasma
E: Transition region	composite both ion and electron current

The bias range between float and plasma voltage is the transition region where physics models are built to analyze the plasma properties. The electron current is given by Equation 2-7 assuming the Maxwellian Distribution of electrons:

$$I_e = eAn_e \left[\frac{kT_e}{2\pi m} \right]^{1/2} \exp\left(-\frac{e(V_p - V)}{kT_e}\right) \quad (2-7)$$

where A is the probe area, m is the electron mass, n_e is electron density, V_p is plasma potential. The electron temperature T_e is determined by the slope of logarithm of I_e vs. V from Equation 2-8:

$$\ln I = \frac{eV}{kT_e} + Const \quad (2-8)$$

The actual EEDF for non-Maxwellian electrons can be determined by Druybesteyn Method [36] by which the EEDF is calculated from second derivative of current and voltage curve:

$$f(\varepsilon) = \frac{4}{e^2 A} \sqrt{\left(\frac{-m(V - V_p)}{2e}\right)} \frac{d^2 I}{dV^2} \quad (2-9)$$

Figure 2-9 presents an EEDF calculated from Equation 2-9, with a current-voltage measured by Langmuir Probe for Ar plasma discharged at 0.5 Torr, RF at 30W.

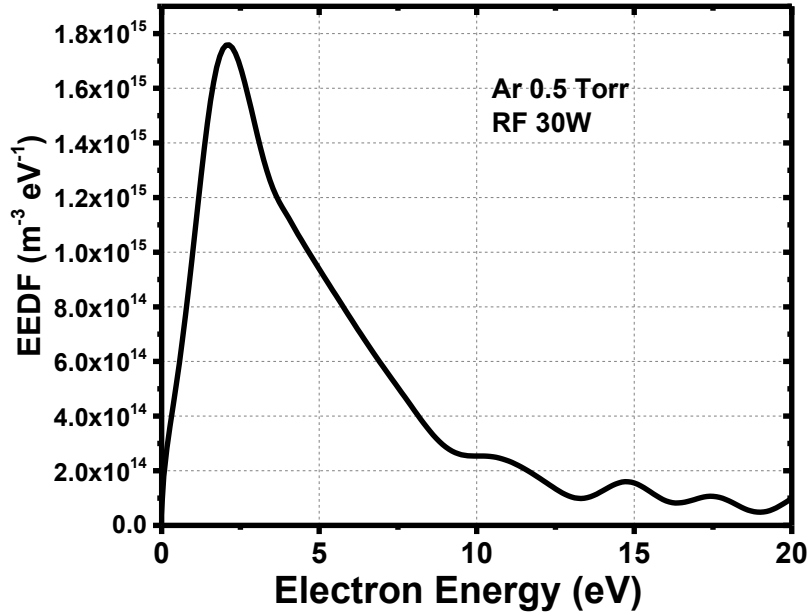


Figure 2-10 EEDF calculated by Equation 2-9 for a Ar Plasma measured at IEC

The electron density and electron temperature is estimated from:

$$n_e = \int f(\varepsilon) d\varepsilon \quad (2-10)$$

$$\langle E_e \rangle = \frac{1}{n_e} \int \varepsilon * f(\varepsilon) d\varepsilon \quad (2-11)$$

In this thesis, the Druybesteyn Method is used to analyze the current and voltage curve measured by Langmuir Probe. To avoid the probe surface becoming coated from the deposition, the probe is in-situ heated to re-evaporate the surface

coating by applying positive voltage drawing high electron current from plasma.

Figure 2-11 shows the picture of Hiden Analytical Langmuir Probe installed at IEC with z-direction and x-y 360° rotation.



Figure 2-11 Hiden Analytical Langmuir Probe installed in PECVD chamber at IEC

Chapter 3

SILICON THIN FILM DEPOSITION, FILM AND DEVICE CHARACTERIZATION

The purpose of this chapter is to describe the PECVD deposition system and the processing condition for the growth of the Si film, as well as the material and device characterization tools used to analyze film and device properties.

3.1 Multi-Chamber Plasma Enhanced Chemical Vapor Deposition (PECVD) System

Typically, a mixture of Silane (SiH_4) and Hydrogen (H_2) gases are used for the growth intrinsic Si films where P type and N type Si layer can be deposited by introducing dopant gas such as Diborane (B_2H_6) and Phosphine (PH_3) respectively. The flow rates of each gas are controlled by Mass Flow Controllers (MFC). A gas discharge is initiated and maintained by electric field between the two parallel plates shown in Figure 2-1, with one at ground and the other one powered either by DC, Radio Frequency (RF) -13.56 MHz or Very High Frequency (VHF) >40.68 MHz power supply. The substrates are usually connected to the grounded electrode (cathode). The radicals from the gas dissociation diffuse to the substrates for hydrogenated silicon film deposition. The substrate is usually between 150 and 400 °C for optimized film quality. The gas pressure is controlled by the throttle valve connected to process pump. The process window for deposition is typically from 0.1

Torr to 10 Torr depending on the geometry of the vacuum chamber. The minimum plasma ignition voltage is a function of pressure \times electrode gap referred to as the Paschen Curve [37].

Silicon thin film solar cell application requires either doped or intrinsic film deposited by PECVD. A multichamber PECVD system is designed to minimize impurities and dopants by avoiding cross contamination. Moreover, in the multichamber design the deposition temperature, internal electrode spacing as well as discharge frequency can be optimized for each layer individually.

Figure 3-1 is the schematic of in-line configuration of multichamber PECVD system at IEC, which includes 2 loadlock chamber for sample load and unload, 2 process chamber for different intrinsic layers deposition and 2 process chamber for p type and n type layer deposition. Each chamber has individual plasma generator and gas line for variable film deposition.

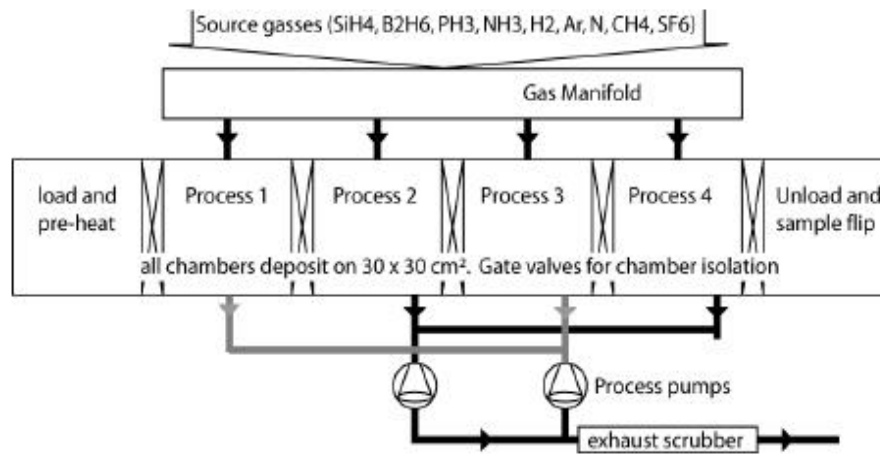


Figure 3-1 Schematic of in-line multichamber PECVD system at IEC

Figure 3-2 shows the picture of the Six Chamber in line PECVD system used in this research.



Figure 3-2 Six Chamber in-line PECVD system at IEC

A range of deposition parameters for this thesis are listed in Table 3-1:

Table 3-1 Range of Si thin film deposition parameters in this research

Film type	Pressure (Torr)	Substrate Temperature (°C)	Gas Flow (sccm)	Power (W)
a-Si:H i layer	0.5~2.5	200,250	SiH ₄ :10~20 Si ₂ H ₆ :0~20 H ₂ :0~50	20~120 RF
nc-Si:H i layer	2.5~8	200,250	SiH ₄ :5~20 Si ₂ H ₆ :0~20 H ₂ : 100~500	200~500 RF and VHF
a-SiC:H p layer	0.5	200	SiH ₄ :60 B ₂ H ₆ :15 CH ₄ :3~21	DC Current 123mA
a-Si:H n layer	1.25	200	SiH ₄ :20 H ₂ :120; PH ₃ :20	DC Current 123mA

3.2 Material Characterization

3.2.1 Ultraviolet-Visible-Infrared (UV-VIS-IR) Spectroscopy

In this research, the Perkin-Elmer UV-VIS-IR Spectroscopy is used to measure the film transmission and reflection (T and R) spectrum from which the optical band gap and thickness can be calculated.

The intensity of the light exponentially decreases after penetrating the surface of a material based on Beer-Lambert Law:

$$I(\lambda) = I_o e^{-\alpha(\lambda) \cdot t} \quad (3-1)$$

where I_o is the intensity of incident light, λ is wavelength. t is the thickness of the film can be calculated from the interference fringes:

$$t = \frac{2\lambda_1 \cdot \lambda_2}{n \cdot (\lambda_1 - \lambda_2)} \quad (3-2)$$

where λ_1 and λ_2 are two wavelength peak to peak and n is material refractive index.

The absorption coefficient α can be calculated from T and R of the incident light based on the matrix method for multilayer optical model [38].

Figure 3-3 presents typical transmission and reflection spectrum of a-Si:H layer on glass substrate.

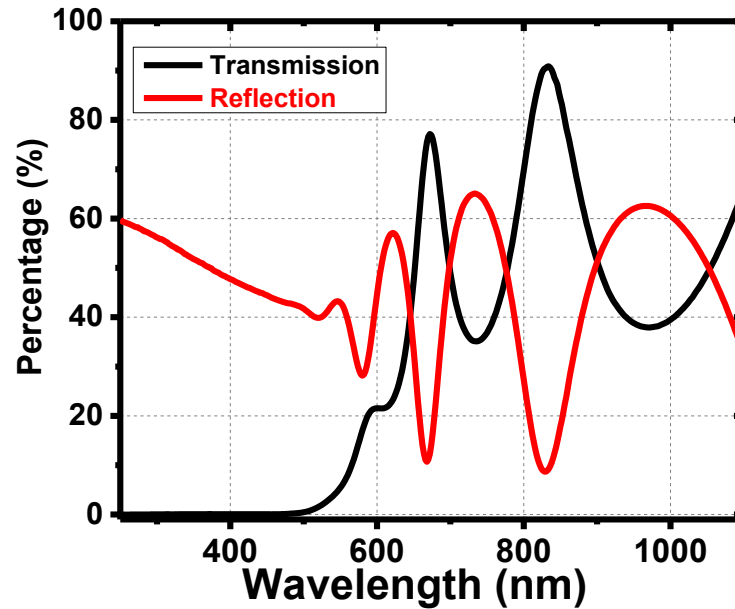


Figure 3-3 Transmission and Reflection of a-Si:H film on glass substrate

The optical band gap of the material can be estimated from Tauc's Equation [39] which the optical band gap can be determined by intercept of the x-axis of the plot based on Equation 3-3:

$$\sqrt{\alpha(\nu) \cdot h\nu} = B(h\nu - E_g^{opt}) \quad (3-3)$$

where α is the absorption coefficient, ν is the frequency of the light and B is constant.

Figure 3-4 shows the typical a-Si:H optical band gap determined by the Tauc's plot with absorption coefficient measured by UV-VIS-IR spectroscopy.

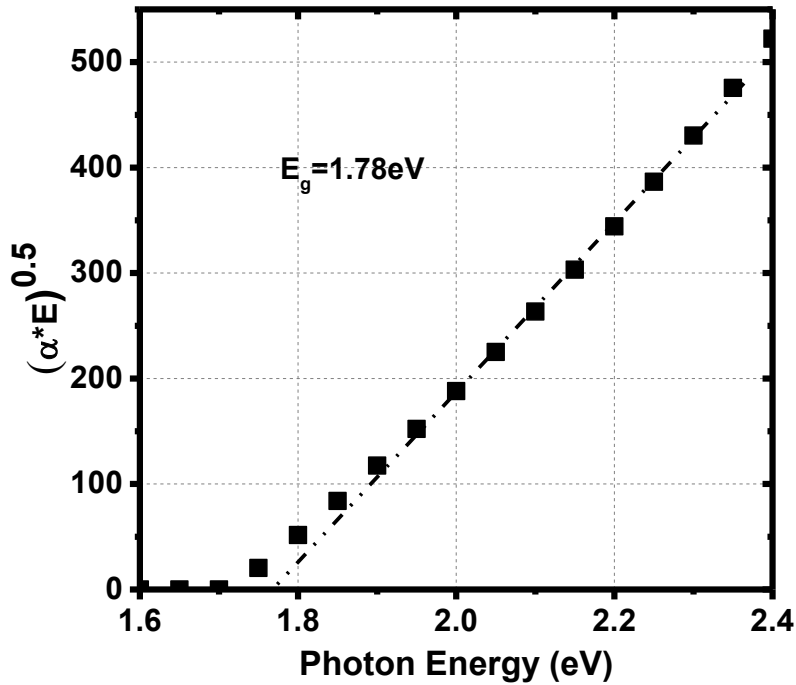


Figure 3-4 Tauc Plot of a-Si:H film deposited by PECVD at IEC

3.2.2 Fourier Transform Infrared Spectroscopy (FTIR)

Fourier Transform Infrared Spectroscopy is a technique to analyze the infrared spectrum of absorption of the material. FTIR is a commonly used method to characterize the chemical bonding as well as different bond vibration modes.

The FTIR measures infrared absorption spectrum at different frequency where instead of using monochromatic light, the incident light beam of FTIR includes a wide range of frequencies. The detector collects total absorption of the beam by the sample. Then the beam is modified to contain a different combination of frequencies to collect a second data point. The Michelson interferometer is used for the generation of light source with combination of different frequencies. The incident light pass through the

Michelson Interferometer with mirror configuration and one of the mirror can be moved to change the light path for wave interference as shown in Figure 3-5. The output light beam from the interferometer includes combination of different wavelength as a function of distance the mirror moved. The raw data of the FTIR collected is total absorption as a function of mirror position. The result of absorption as a function of different frequency is calculated by Fourier Transform of the raw data. FTIR has higher frequency resolution compared with the one using monochromatic light. Figure 3-6 shows Nicolet 6700 FT-IR Spectrometer by Thermo Scientific used in this research.

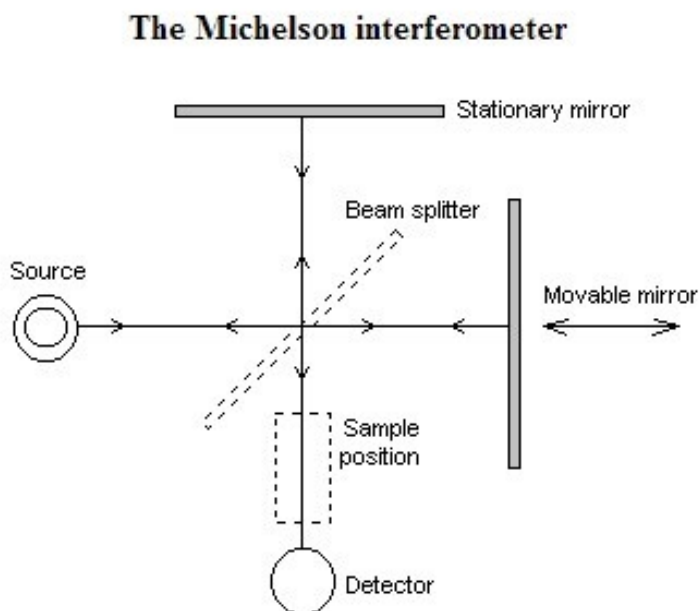


Figure 3-5 Schematic Diagram of Michelson Interferometer for FTIR



Figure 3-6 Nicolet 6700 FT-IR Spectrometer by Thermo Scientific

FT-IR is used to characterize the Si-H bond and H content of hydrogenated Si thin film deposited by PECVD. The wagging mode with absorption peak at 640 cm^{-1} and stretching mode at $2000\sim 2100\text{ cm}^{-1}$ are typically used to characterize the Si-H bond in hydrogenated Si film. The stretching mode could be deconvolve into Low Stretching Mode (LSM) peak centered at 2000 cm^{-1} and High Stretching Mode (HSM) peak centered at 2100 cm^{-1} . The LSM is identified with the bulk Si-H monohydride vibration mode. The HSM peak is contributed by dihydride or polydride Si-H_x bonds, as well as surface Si-H bonds [40]. The HSM peak is also used to estimate the defectiveness or porous structure of hydrogenated Si thin film.

The Microstructure Factor (R_{mf}) is defined as the percentage of HSM of the entire Si-H stretching mode as:

$$R_{mf} = \frac{I_{HSM}}{I_{HSM} + I_{LSM}} \quad (3-4)$$

Microstructure Factor is often used to estimate the a-Si:H thin film quality [41]. In general, it has been established that films which are good for solar cell fabrication, so-called ‘device quality’ films, have low R_{mf} since the dihydride bonds are correlated with voids, defects and unpassivated internal surfaces.

The Hydrogen Content (C_H) can be determined by either wagging mode or stretching mode. The hydrogen content is proportional to the integrated absorption peak. For wagging mode, the hydrogen concentration is calculated by:

$$I_{640} = \int_{-\infty}^{+\infty} \alpha_{640}(\omega) d\omega / \omega; [H] = A_{640} I_{640} \quad (3-5)$$

while α is absorption coefficient, ω is wavenumber and $A_{640} = 1.6 \times 10^{19} \text{ cm}^{-2}$ as a proportionality constant for a-Si:H. For stretching mode, the hydrogen content is calculated by [42]:

$$[H] = A \cdot I_{2000} + B \cdot I_{2100} \quad (3-6)$$

where A and B have been found to be $7.34 \times 10^{19} \text{ cm}^{-2}$ and $2.06 \times 10^{20} \text{ cm}^{-2}$ respectively, which is calibrated by Elastic-Recoil-Detection Analysis (ERDA). The hydrogen content is defined as

$$C_H = [H] / 5 \cdot 10^{22} \quad (3-7)$$

Figure 3-7 shows the FT-IR spectrum of a-Si:H thin film on Si substrate and the Si-H bond analysis from stretching mode, with $R_{mf} = 7.3\%$ and $C_H = 8.2\%$

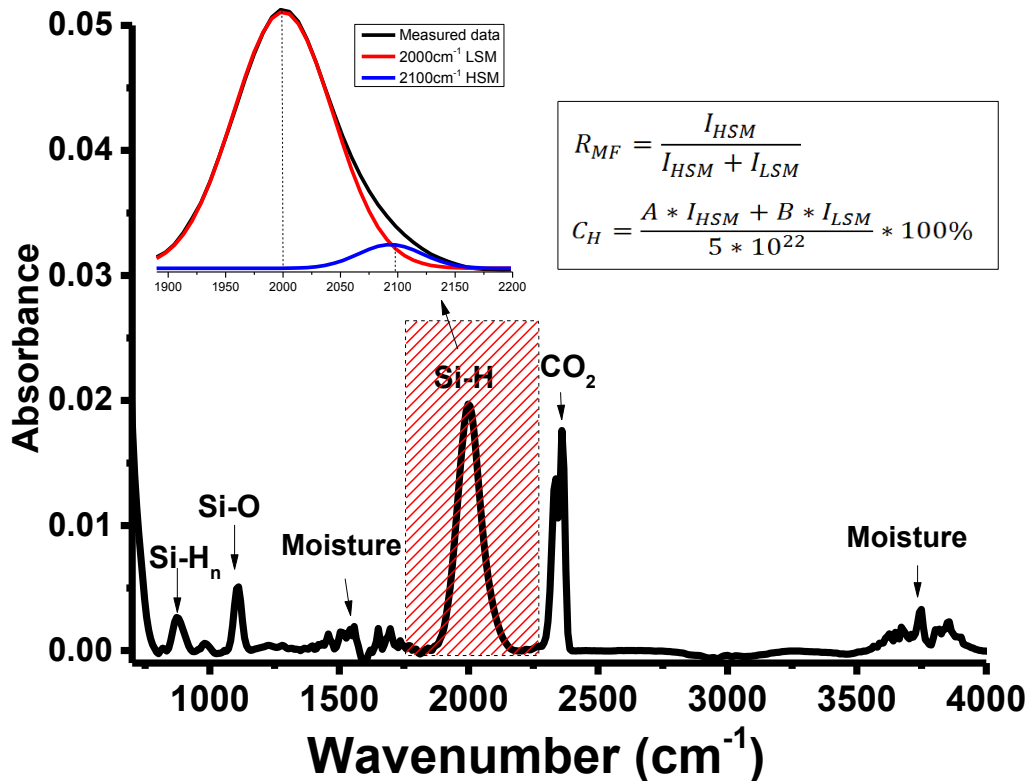


Figure 3-7 FT-IR spectra of a-Si:H thin film and Si-H bond analysis

3.2.3 Raman Spectroscopy

Raman Spectroscopy is a nondestructive technique to characterize molecular vibration modes. Raman Spectroscopy is also called Raman Scattering or Raman Shift spectroscopy.

A laser with visible, near infrared or near ultraviolet range shines on the material surface. The scattered light contains primarily the same wavelength as the incident light, named Rayleigh scattering. However, there are very low intensities of light at different wavelengths which represents the interaction between laser and

materials, named Raman Shift from inelastic scattering. Figure 3-8 presents the energy of the light from Raman scattering. If the final vibrational state of the molecule has higher energy than initial state, the laser frequency shift is known as Stokes Shift. If the final vibrational state is at lower energy state compared with initial state, the shift is called Anti-Stokes shift. The shift frequency correlates vibration energy state inside material.

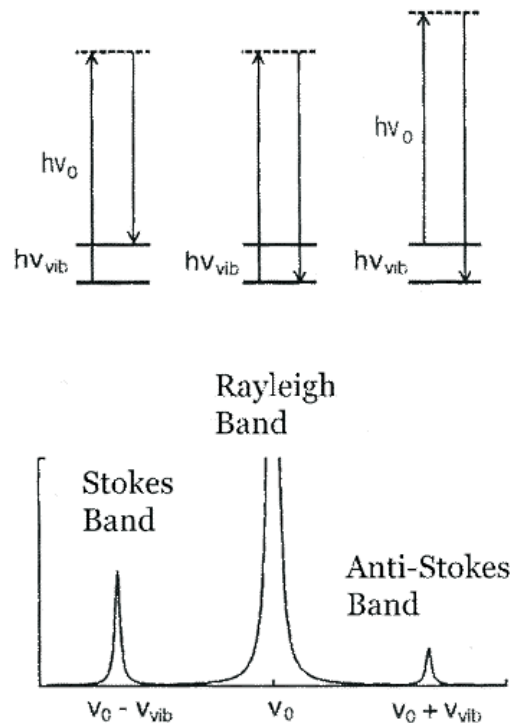


Figure 3-8 Energy of Raman Scattering light

In this thesis, Raman Spectroscopy is used to measure the crystallinity of nanocrystalline portions of the silicon film [43]. Figure 3-9 shows the Raman spectrum of crystal Silicon (c-Si), nanocrystalline Silicon (nc-Si:H) and amorphous Silicon (a-Si:H). Raman spectrum of c-Si shows a narrow peak at 520 cm^{-1}

corresponding to the Transverse Optic (TO) Mode. The Raman Spectrum of a-Si:H sample shows a broad peak centered at 480 cm^{-1} from TO mode of a-Si:H phase. The Raman Spectrum of nc-Si:H film shows asymmetrical peak which containing a mixture of c-Si and a-Si:H spectrum.

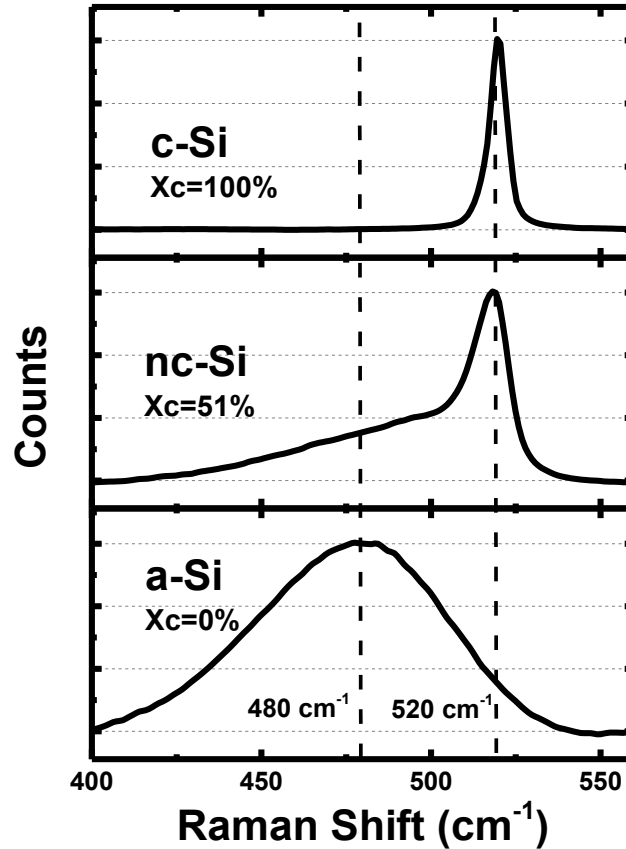


Figure 3-9 Raman Spectra of Crystal Silicon, Nanocrystalline Silicon and Amorphous Silicon

The crystallinity of nc-Si:H is determined by 3-peak deconvolution of the Raman Spectrum. The narrow peak centered at 520 cm^{-1} is attributed to crystal silicon phase and the broad peak centered at 480 cm^{-1} is attributed to amorphous silicon

phase. The intermediate peak around 510 cm⁻¹ is attributed by crystal silicon with small size or defective crystalline phase. In Raman spectrum, the integrated peak intensity is proportional to the phase volume:

$$I_a = \sigma_a V_a; \quad I_c = \sigma_c V_c \quad (3-8)$$

where σ is the integrated Raman cross-section of the TO mode and V is the phase volume. The crystalline volume fraction can be calculated by the equation:

$$F_c = \frac{V_c}{V_c + V_a} = \frac{I_c}{I_c + \left(\frac{\sigma_c}{\sigma_a}\right) \cdot I_a} \quad (3-9)$$

The ratio of cross section for crystal phase and amorphous depends on the crystal size as well as the excitation wavelength [44]. The Raman Crystalline Volume Fraction X_c defined by Equation 3-10 with assumption $\sigma_c/\sigma_a=1$:

$$X_c = (I_{520} + I_{510}) / (I_{520} + I_{510} + I_{480}) \quad (3-10)$$

Therefore, X_c is not the true crystalline volume fraction in the film, but used as a “figure of merit” for crystallinity and often termed as “Raman crystallinity”. Figure 3-10 shows the 3 peak devolution analysis of Raman Spectrum for nc-Si:H layer.

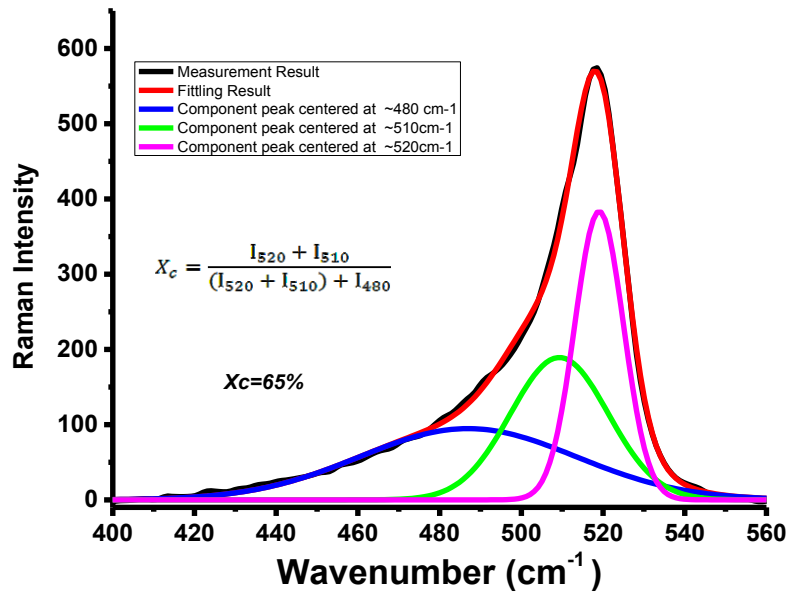


Figure 3-10 Three Peak Devolution of nc-Si:H layer Raman Spectrum leading to a crystalline fraction $X_C=65\%$.

3.2.4 X-Ray Diffraction

X-Ray Diffraction (XRD) characterizes the atomic structure of crystalline material. The crystal material could be considered as a series of parallel plane with atoms in periodic lattice position.

X-ray incident on the material with variable angles as shown in Figure 3-11, and the diffraction peak is determined by Bragg's Law:

$$2d \sin\theta = n\lambda \quad (3-11)$$

where d is the spacing between lattice plan, θ is incident angle, n is integer and λ is the wavelength of the X-ray. In this thesis, the incident X-ray is from CuK_α with wavelength 1.5418\AA .

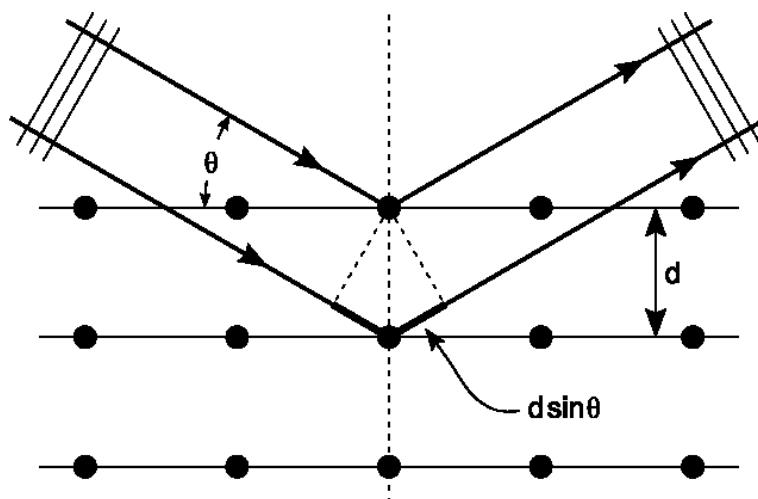


Figure 3-11 Scheme of X-Ray Diffraction

Figure 3-12 shows the XRD spectrum of $\sim 1\mu\text{m}$ nc-Si:H deposited on glass substrate with high and low X_c . There are three main diffraction peaks of crystal silicon plane (111), (220) and (311) with 2θ at 28.47° , 47.34° and 56.17° respectively.

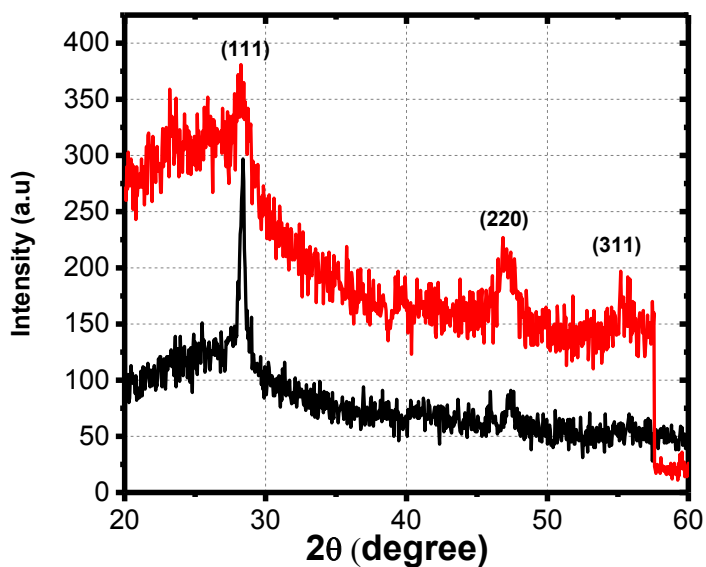


Figure 3-12 XRD Spectrum of nc-Si:H with $X_c=67\%$ and 46% , color in red and black respectively

Moreover, the grain size of the crystal phase can be estimated from Full Width of Half Maximum (FWHM) of the diffraction peak through Scherrer's Equation [45]:

$$\tau = \frac{0.9\lambda}{\beta \cos\theta} \quad (3-12)$$

where τ is the grain size, λ is X-ray wavelength, β is FWHM of the peak and θ is Bragg angle.

3.3 Solar Cell Device Characterization

The solar cell behavior under illumination is characterized by Current-voltage (J-V) measurements from which key performance parameters are obtained: open circuit voltage (V_{oc}), short circuit current (J_{sc}) and fill factor (FF). Figure 3-13 presents a standard J-V curve from solar cell measurement with definition of FF and Efficiency:

$$FF = \frac{V_{mp}J_{mp}}{V_{oc}J_{sc}} \quad (3-13)$$

$$E_{ff} = J_{sc} * V_{oc} * FF \quad (3-14)$$

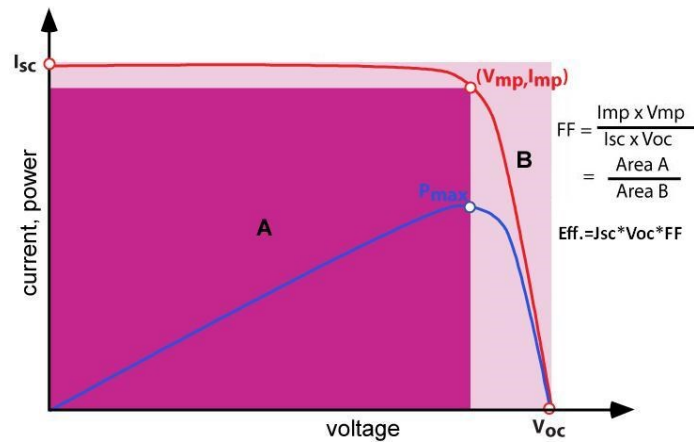


Figure 3-13 Standard Solar Cell J-V curve and power output as a function of voltage [46]

The measurement apparatus is shown in Figure 3-14 . The solar cell is measured under illumination from a solar simulator with 100 mW/cm^2 AM 1.5 spectrum provided by a spectally filtered Xe lamp, with solar cell temperature controlled at 25°C . The cells are connected with four point probes to a Keithly sourcemeter SMU which provide voltage sweep across the terminals and records current output simutanously.

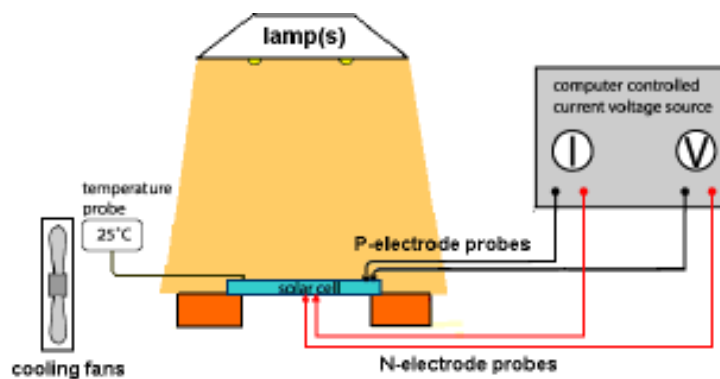


Figure 3-14 Apparatus of Solar Cell J-V measurement [46]

Chapter 4

AMORPHOUS SI FILM DEPOSITION AND SOLAR CELL WITH GAS PHASE ADDITIVE

4.1 Introduction

Hydrogenated amorphous (a-Si:H) and nano-crystalline Si (nc-Si:H) thin film are attractive materials for photovoltaic and thin film transistor application. The general challenge for the technology is simultaneous development of high throughput and high quality Si thin films. The requirements are often in conflict with each other.

Plasma enhanced chemical vapor deposition (PECVD) is the most common processing technique, where the gas precursor is a mixture of SiH_4/H_2 and high growth rate is typically reached either by using a high frequency (> 40 MHz) plasma excitation (VHF), or a high power and high pressure at an RF frequencies of 13.56 MHz. It has been reported that high efficiency solar cells have been achieved at a high growth rate of $\sim 2\text{nm/s}$ with 100 MHz discharge [47]. However, VHF and high pressure approaches have limitations, e.g. non-uniform deposition over large area for VHF and excessive dust formation and frequent chamber cleaning for high pressure conditions. Another approach to increase the growth rate is to replace the SiH_4 with Si_2H_6 where Futako et al. reported a growth rate of 20 A/s using pure Si_2H_6 [48]. Interestingly, Hammad et al. reported that addition of a small percentage of Si_2H_6 to SiH_4/H_2 gas mixture at low pressure significantly increased the growth rate [22].

However, little data was published characterizing the film properties and solar cell performance with enhanced growth rate using gas phase additive. The work of this chapter will focus on the promising approach of enhanced growth rate of high quality intrinsic a-Si:H film by gas phase additive. The effect of Si₂H₆ as an additive into SiH₄/H₂ mixtures and comparison of a-Si:H growth rates, film properties and solar cell performance with and without additive are addressed in this chapter.

4.2 Experiment

In this work, all the a-Si:H films were deposited in a multi-chamber PECVD system. The intrinsic a-Si:H layer (i layer) was deposited by capacitively coupled 13.56 MHz RF plasma with the electrode to substrate gap of 1.4 cm. RF power was applied to the powered anode and the substrates were mounted on the grounded cathode. Semiconductor grade SiH₄, Si₂H₆ and H₂ were used for i layer deposition. The physical and structural properties of the films were strongly affected by the deposition conditions, which includes RF power, pressure, H₂ dilution, temperature as well as RF frequency. For comparison, each series of experiments were done with and without the Si₂H₆ additive, while the total flow of silicon source, F_{SiH₄} + F_{Si₂H₆}, was kept as constant. The Si₂H₆ additive fraction, F_{Si₂H₆} / [F_{Si₂H₆} + F_{SiH₄}] was 0.1, for most series of experiments, i.e Si₂H₆ flow was 10% of the SiH₄ flow.

The design of deposition parameters was based on the plasma ignition test to establish stable plasma discharge. At 0.5 Torr, with power <80W the plasma became unstable with H₂ dilution due to its higher ionization threshold energy. Thus, at 0.5

Torr , a-Si:H films were deposited using SiH₄/Si₂H₆ without H₂ dilution. At higher pressure, the total flow F_{SiH₄}+F_{Si₂H₆}=10 sccm was diluted with 50 sccm of H₂. The effect of RF power and substrate temperature were also investigated for different film growth parameters and the main deposition conditions are summarized in Table 4-1.

Table 4-1 Intrinsic a-Si:H main deposition parameters with and w/o additive

Pressure (Torr)	Temperature (°C)	SiH₄/Si₂H₆/H₂ (sccm)	Power (W)
0.5	200,250	20/0/0 18/2/0	20~80
1.25 & 2.5	200,250	10/0/50 9/1/50	20~120

The i layers which were typically ~300 nm were deposited on Corning 1737 glass and polished 300μm p type c-Si wafer for Fourier transform infrared spectroscopy (FTIR) measurement. The film thickness was estimated from optical measurements using a UV-VIS spectrophotometer. Tauc plots were used to determine the optical band gap and the Si-H bond configuration was characterized by FTIR. The hydrogen content C_H and microstructure factor R_{mf}=I_{SiH₂}/(I_{SiH₂}+I_{SiH}), which is related to the quality of a-Si:H film, were calculated from the Si-H stretching mode.

To further understand the relationship between i layer properties and device performance, a-Si:H p-i-n solar cells were fabricated with a 250 nm i layer on standard textured SnO₂:F on soda lime glass (TEC8 brand) in a superstrate configuration . Devices were completed by evaporation of 500 nm Al contact using a shadow mask to define cells of either 0.4 or 1.0 cm². The p layer and n layer properties were kept constant while i layers were deposited using different process conditions. The stability

of the devices was evaluated by light soaking at 100 mW/cm^2 and 50°C , with device held at open circuit condition as is standard practice.

4.3 A-Si:H Deposition and Material Properties with and without Si_2H_6 Additive

In this section, the discussion will focus on a-Si:H material properties where growth rate, Si-H bond, and band gap are characterized to understand the effect of deposition condition which include Si_2H_6 additive, H_2 dilution, deposition pressure and temperature.

4.3.1 A-Si:H deposition without H_2 dilution

The a-Si:H films without H_2 dilution were deposited from SiH_4 and Si_2H_6 discharge at 0.5 Torr and at a substrate temperature of 200°C . The total flow of SiH_4 and Si_2H_6 were kept constant at 20 sccm, with a SiH_4 flow of 18 sccm and Si_2H_6 flow of 2 sccm. The deposition RF power was varied from 20W to 80W.

Figure 4-1 presents the deposition rate dependence on increasing power at 0.5 Torr. For the series without Si_2H_6 the growth rate increased from 2.7 A/s at 25 W to 5.4 A/s at 70 W and with 10% Si_2H_6 additive the growth rate is similar following the same trend with power. At lower power, $<50 \text{ W}$, the growth rate with Si_2H_6 was also $\sim 10\%$ higher which consisted with the 10% more Si atoms coming from Si_2H_6 . This result indicated that, at a low pressure of 0.5 Torr, the increased growth rate of gas additive may just result from the complete dissociation of Si_2H_6 resulting in 10% more Si radicals impinging onto the deposition surface. However, at higher power ($>50\text{W}$),

the growth rates were similar or even decreased compared to the growth rate without the Si_2H_6 additive. At high power a significant dust formation was observed and resulted in an un-stable plasma at 80W due to the dust formation inside discharge region. This can explain the observed reduction in film growth rate at high power.

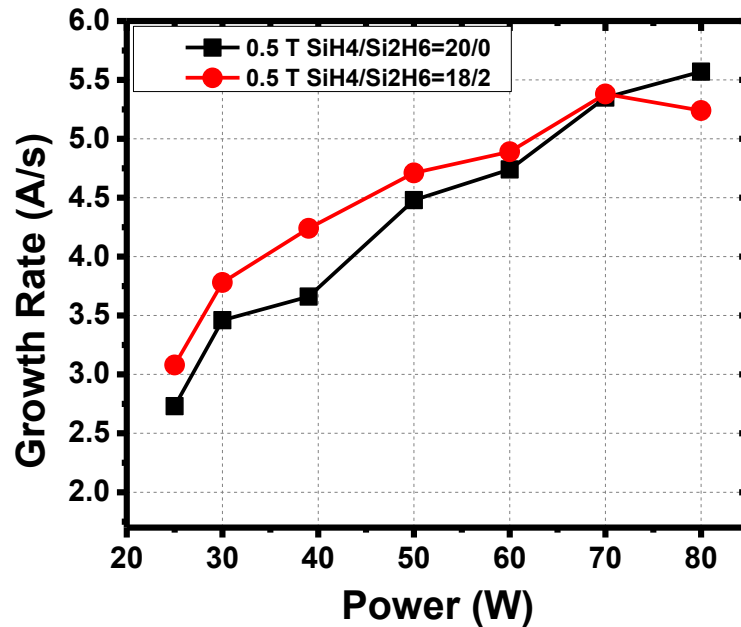


Figure 4-1 Variation of growth rate as a function of RF power at 200°C, 0.5 Torr without H_2 dilution

It is well known that a higher microstructure factor R_{mf} , the fraction of dihydride to monohydride bonding in the film from FTIR correlates with more defective a-Si:H films [41]. Figure 4-2 showed the R_{mf} as a function of RF power with and without Si_2H_6 additive. It was found that R_{mf} decreased with increasing RF power in both SiH_4 and $\text{SiH}_4/\text{Si}_2\text{H}_6$ discharges as well as with higher with higher total flow. At total flow of 20 sccm with just SiH_4 discharge, the R_{mf} decreased from 32.5% at 25

W to 13.7 % at 80 W and adding 10% Si₂H₆ additive increased the R_{mf} value compared with SiH₄ only discharge. However, the R_{mf} was also reduced by increasing RF power, from 38.5% at 25W to 17.8% at 80 W. This result suggested that better quality a-Si:H film were obtained at higher RF power, which resulted from higher H and Si radical ratio in the plasma. The detail mechanism will be discussed in Chapter 6 based on characterization of the plasma properties. .

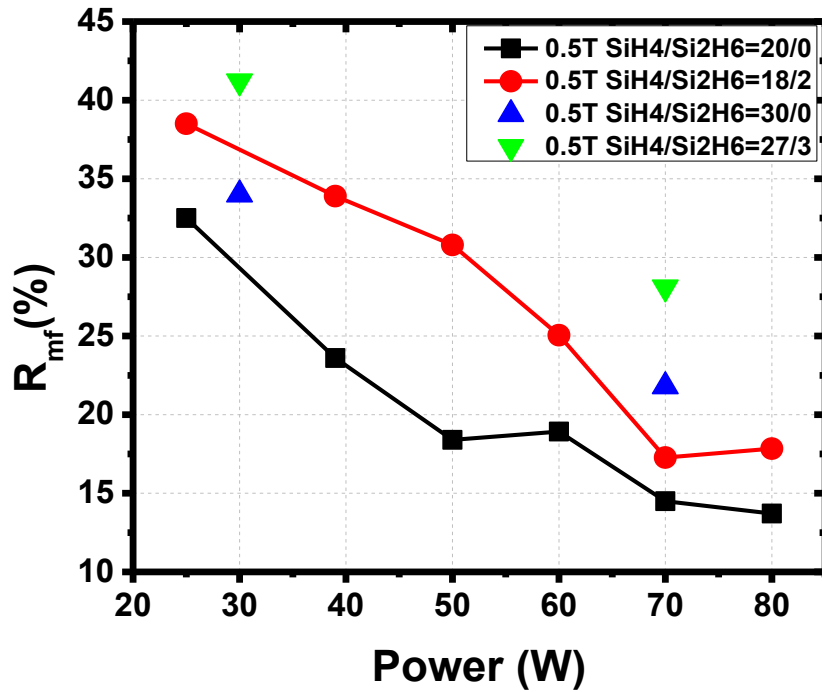


Figure 4-2 FTIR results microstructure factor R_{mf} at 200°C, 0.5 Torr without H₂ dilution

4.3.2 A-Si:H deposition with H₂ dilution

It had been widely reported that H₂ dilution in SiH₄ discharge improves the a-Si:H quality. In this section, a-Si:H films with H₂ dilution were processed from SiH₄ -

$\text{Si}_2\text{H}_6 - \text{H}_2$ mixture with total flow rate of $\text{SiH}_4 + \text{Si}_2\text{H}_6$ kept constant at 10 sccm and diluted with 50 sccm H_2 . The substrate temperature was fixed at 200°C and the films were deposited at both 1.25 Torr and 2.5 Torr and the RF power was varied from 30 to 120W.

Figure 4-3 presents the variation of deposition rate by increasing RF power at 1.25 Torr. For the series without any Si_2H_6 ($\text{SiH}_4 / \text{Si}_2\text{H}_6 / \text{H}_2 = 10/0/50$), The growth rate increases from 1.8 A/s at 30 W to 2.7 A/s at 50 W for gas composition of $\text{SiH}_4 / \text{H}_2$ (without Si_2H_6) and saturates around 2.8 A/s with higher power. By adding 10% Si_2H_6 in the gas mixture, 10% more Si atoms in the discharge, the growth rate increased by ~30% at a power of 50 W. The maximum growth rate obtained was 3.5 A/s with the Si_2H_6 additive.

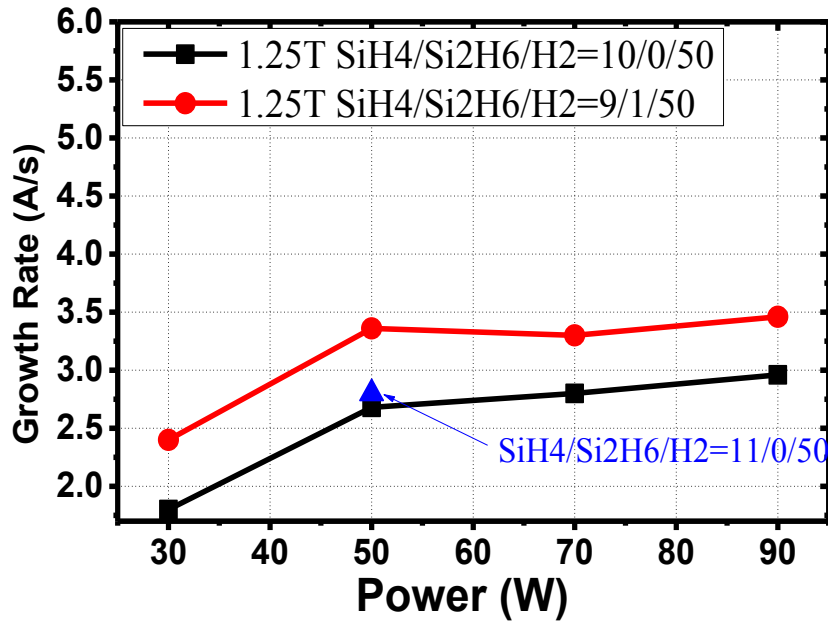


Figure 4-3 Variation of growth rate as a function of RF power at 200 °C with deposition pressure of 1.25 Torr

Figure 4-4 presents the variation of growth rate by power at 2.5 Torr. The power and growth rate has the similar trend as at 1.25 Torr. However, the growth rate increased by ~60% at 50 W RF power by adding 1 sccm of Si₂H₆. Thus, by adding 10% Si₂H₆, the absolute value of growth rate enhancement is around 1.6A/s, which is almost 2.5 times that of the low pressure case. To compare the enhancement between 10% increase in Si atoms from SiH₄ or Si₂H₆, we found that adding another 1sccm of SiH₄ (SiH₄/ Si₂H₆/ H₂=11/0/50), resulted in less than 0.2 A/s growth rate enhancement at either 1.25 Torr or 2.5 Torr. Thus, this confirms that the large increase in growth rate with the addition of small amounts of Si₂H₆ is not due to the simple increase of Si atom concentration, but might result from the enhanced SiH₄ dissociation by higher

electron density with Si_2H_6 additive [22]. The effect of Si_2H_6 additive inside plasma will be discussed in Chapter 6 using plasma characterization.

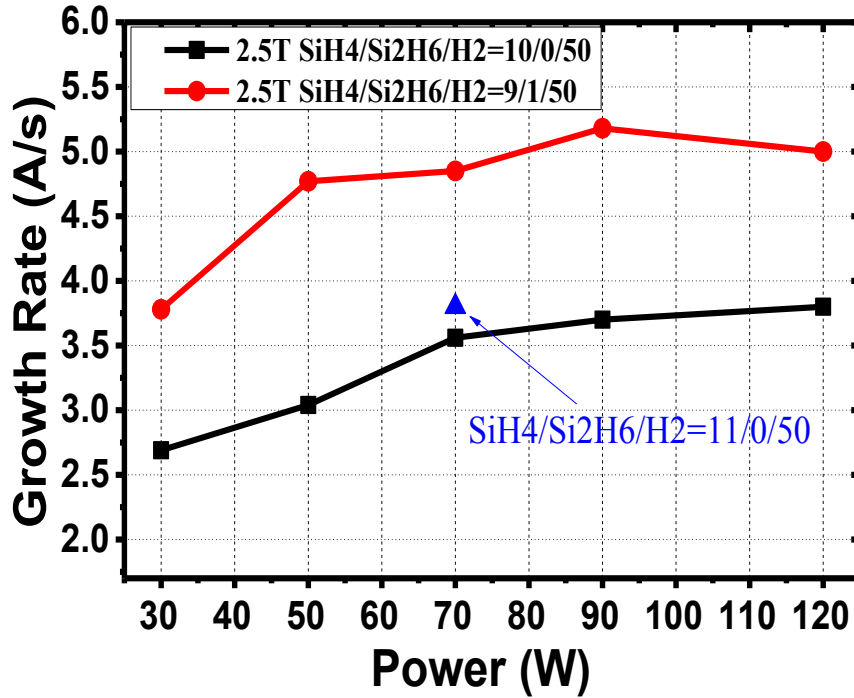


Figure 4-4 Variation of growth rate as a function of RF power at 200 °C with deposition pressure of 2.5 Torr

Figure 4-5 shows the relationship between R_{mf} and power at different pressures with and without Si_2H_6 additive at 200 °C. We found that R_{mf} decreases with increase of RF power coincident with an increase in growth rate. At 1.25 Torr without Si_2H_6 additive, the R_{mf} of the film gradually decreased from 7% to 3% while the power increased from 30 W to 70 W. By adding 10% Si_2H_6 , the R_{mf} increased to 12% at 30 W. At 70 W, the R_{mf} with Si_2H_6 additive is almost the same as the film deposited by SiH_4/H_2 . We were unable to obtain FTIR data at higher power at 1.25 Torr since the

film peeled off from c-Si substrate. By increasing the deposition pressure to 2.5 Torr, R_{mf} substantially increased. The R_{mf} increased by about 4 times at low power (30W) and shows the similar decreasing trends between power (growth rate) and R_{mf} which was observed at 1.25 Torr. At 2.5 Torr, the film at high growth rate, 5.2 A/s obtained with 10% Si_2H_6 additive, has a relatively low R_{mf} of 9%.

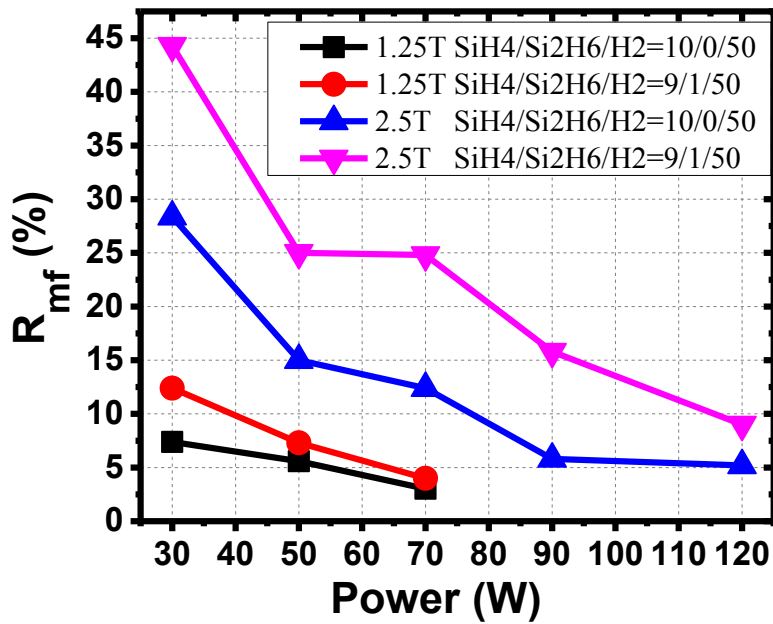


Figure 4-5 FTIR results of R_{mf} for a-Si:H films on c-Si

Figure 3-6 presents the H content of these films. The film H content with 1.25 Torr is lower compared with 2.5 Torr and it decreases with higher RF power. There is no significant change in H content by adding 10% Si_2H_6 .

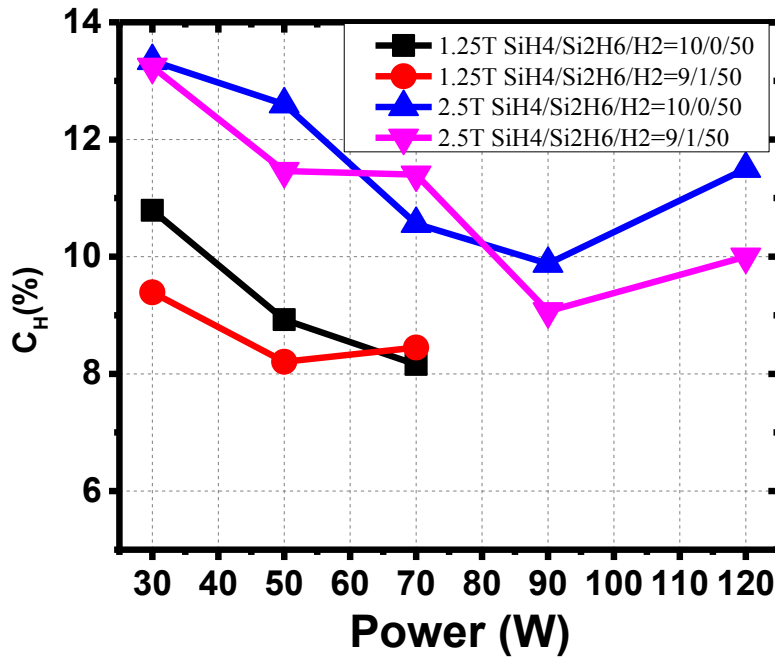


Figure 4-6 FTIR results of H content for a-Si:H films on c-Si

Figure 4-7 presents the Tauc plots obtained from VASE measurements. E_g of the films at 1.25 Torr are the same with and without 10% Si_2H_6 additive. The bandgap (E_g) at 2.5 Torr slightly shift to higher value. The relationship between E_g and device performance will be discussed in solar cell Section 4.4.3.

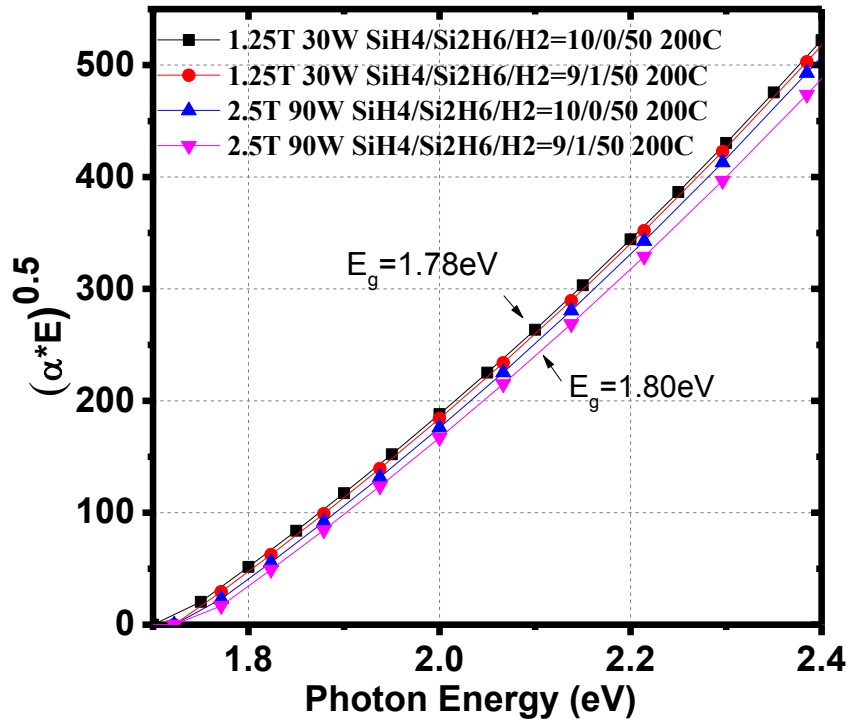


Figure 4-7 Tauc plots of a-Si:H i layers on glass at different deposition conditions.

4.3.3 Effect of deposition Temperature

Deposition temperature was another parameter having strong influence the a-Si:H film opto-electronic and structural properties. The impact of substrate temperature on structure is quantified by the H content concentration and microstructure factor, both obtained by FTIR spectra. The incorporation of H into Si matrix has major effect on band gap of a-Si:H.

Table 4-2 summarized a series of a-Si:H deposition at 200°C and 250°C with large variation in deposition parameters, including Run 1 and 2 at lower RF power and

growth rate without Si₂H₆ additive and H₂ dilution, as well as Run 3 and 4 at higher RF power and growth rate with Si₂H₆ additive and H₂ dilution.

Table 4-2 A-Si:H deposition conditions and film structural properties at substrate temperatures of 200 °C and 250 °C

Run#/ T °C	Power (W)	Pressure (Torr)	SiH ₄ (sccm)	Si ₂ H ₆ (sccm)	H ₂ (sccm)	Growth Rate (Å/s)	R _{mf} (%)	C _H (%)
1/200	25	0.5	20	0	0	2.8	22	10.5
2/250	25	0.5	20	0	0	3.1	8	6.7
3/200	90	2.5	9	1	50	5.2	15.8	9.1
4/250	90	2.5	9	1	50	5.0	5.9	8.1

The primary effect of substrate temperature is on the structural properties with negligible change in growth rate. At 250 °C, R_{mf} was reduced by nearly a factor of 3 compared to films grown at 200 °C due to reduction of dihydride bond as can be seen in Figure 4-8. The hydrogen content in films deposited in pure SiH₄ at 25W and 0.5 Torr was reduced from 10.5% to 6.7% by increasing growth temperature from 200 to 250 °C while only small changes in H₂ content were seen for films deposited at 90W and 2.5 Torr with Si₂H₆ additive and H₂ dilution.

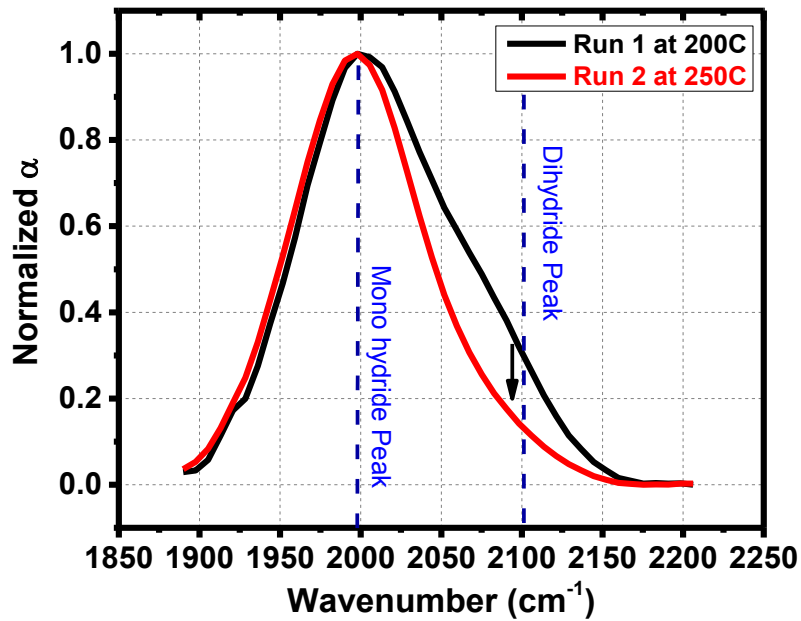
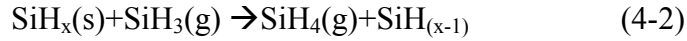


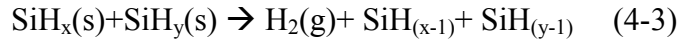
Figure 4-8 FTIR Spectra of a-Si:H deposited at 200 °C and 250 °C

The reduction of dihydride bond and hydrogen content at higher substrate temperature could be explained by either Eley-Rideal abstraction reaction or hydrogen elimination reaction which are related to hydrogen surface reactive desorption, as depicted in Figure 4-9. The Eley-Rideal abstraction reaction regarding kinetics of surface hydrogen removal by atomic hydrogen bombardment or the reaction with SiH_x radicals. For the a-Si:H growth surface terminated with SiH, SiH₂ or SiH₃, the atomic hydrogen or SiH₃ radical is absorbed then reacts with SiH_x at growth surface to form gas phase H₂ or SiH₄ by breaking Si-H bond and desorbing hydrogen atom at growth surface, leaving Si dangling bond for further Si-Si bond formation of a-Si:H network.





For the hydrogen elimination reaction, hydrogen atoms from surface SiH, SiH₂ or SiH₃ react with each other to form gas phase hydrogen by breaking Si-H bond, leaving Si dangling bond for a-Si:H network formation.



The Eley-Rideal abstraction is exothermic, while hydrogen elimination is endothermic (higher temperature, higher reaction rate). Lower dihydride and hydrogen content at higher temperature may indicate the elimination reaction mechanism dominates the hydrogen desorption in these a-Si:H deposition region.

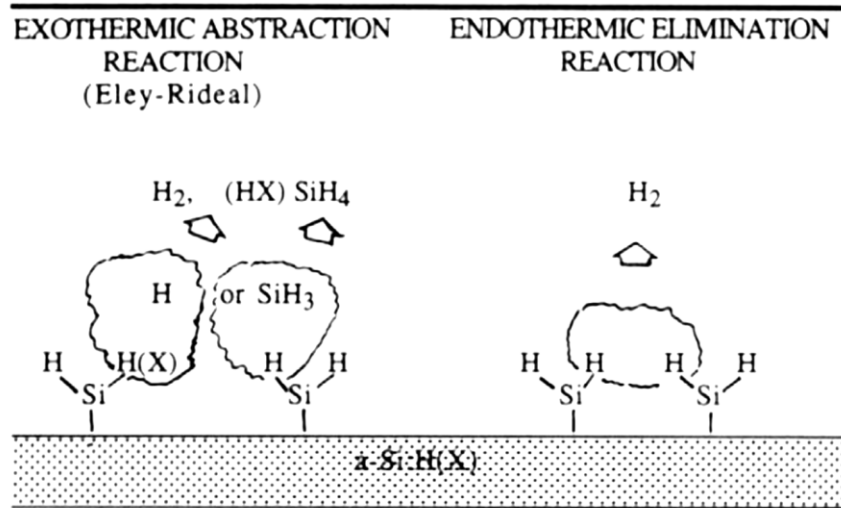


Figure 4-9 Hydrogen desorption reaction at a-Si:H growth surface [27]

It has been reported that the optical band gap is a function of hydrogen content [49]. In Figure 4-10 the Tauc Plot for the a-Si:H films grown under different growth conditions are compared. Eg of films grown at 250 °C are slightly lower than films deposited at 200 °C with band gap from 1.79 eV to 1.75 eV respectively. The band

gap change of the i-layer might be the reason for change in solar cell open circuit voltage which will be discussed in the following section.

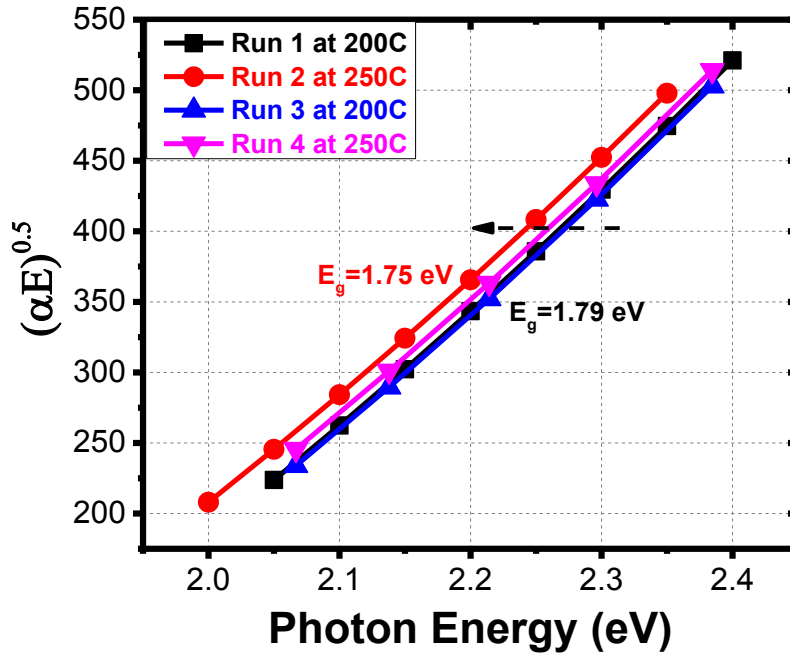


Figure 4-10 Tauc Plot of a-Si:H deposited at 200 °C and 250 °C

4.4 Device Performance of a-Si:H at Different Deposition Conditions

The properties of a-Si:H p-i-n solar cells are evaluated with respect to the growth conditions of the intrinsic a-Si:H layer with respect to , current-voltage (JV) parameter, quantum efficiency (QE) [50]and stability under light soaking (LS) conditions.

All the a-Si:H p-i-n solar cells were fabricated in the configuration shown in Figure 1-3. The p- and n-type doping layers were kept constant and consisted of a ~10

nm boron doped a-Si:HC:H p-type layer followed by ~8 nm band gap profile buffer layer and ~20 nm phosphorus doped a-Si:H n-type layer. The only variable was the ~250 nm intrinsic a-Si:H layers deposited with different Si₂H₆ additives, H₂ dilution and substrate temperature.

4.4.1 Solar cell performance: i layer with Si₂H₆ and without H₂ Dilution

Figure 4-11 and Figure 4-12 show the JV and QE data of the a-Si:H solar cells with a ~200 nm i-layer deposited at 0.5 Torr without H₂ dilution where devices with Si₂H₆ additive at a growth rate of 5.4 A/s are compared with a baseline device without additive deposited at 1.8 A/s. Table 4-3 shows the JV performance comparison of these two cells.

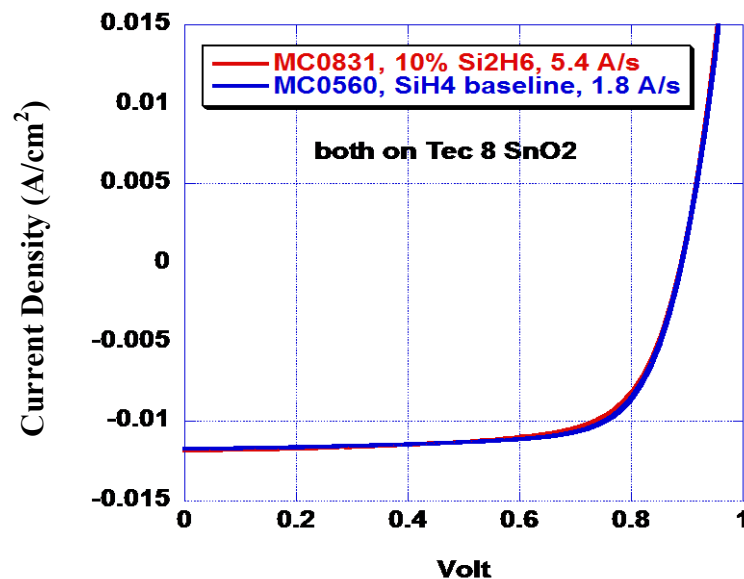


Figure 4-11 Light JV curves for devices with and without 10% Si₂H₆ additive

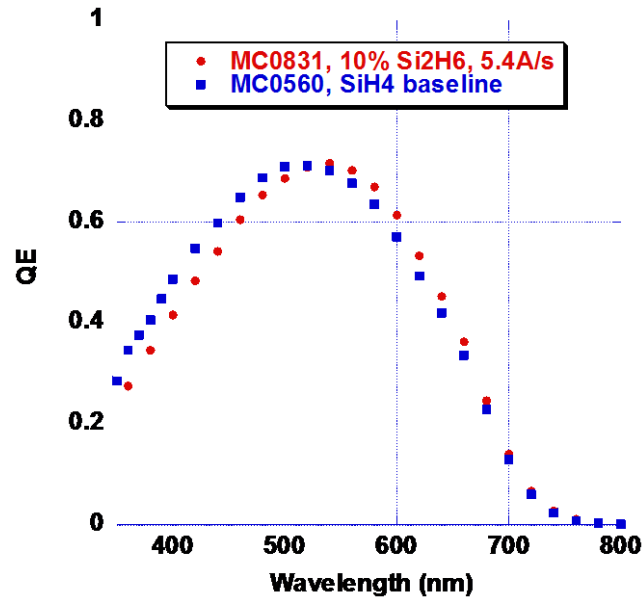


Figure 4-12 QE curves for devices with and without 10% Si₂H₆ additive

Table 4-3 JV performance comparison of devices with and without 10% Si₂H₆ additive

	SiH ₄ (sccm)	Si ₂ H ₆ (sccm)	Power (W)	GR (A/s)	V _{oc} (Volts)	FF (%)	J _{sc} (mA/cm ²)	E _{ff} (%)
(baseline)	20	0	20	1.8	0.89	72	11.7	7.5
MC0831	18	2	70	5.4	0.89	70	11.8	7.3

Both of the cells have V_{oc} ~0.89 V, FF ~70% with Efficiency ~7.5%. Clearly the addition of 10% Si₂H₆ additive has negligible influence on initial cell performance while tripling the growth rate.

4.4.2 Effect of growth temperature and H₂ dilution on solar cell without additive

As previously discussed about material properties, Figure 3-8, higher substrate temperature results lower R_{mf}. (R_{mf}=22% CH=10.5% at 200 C vs R_{mf}=8% C_H=6.7%

at 250 °C, respectively.) Two p-i-n solar cells were fabricated with i layer deposited at 200 °C and 250 °C.

Figure 4-13 shows the initial QE comparison of the cells with i layer at 200 °C and 250 °C, RF power 25W, without H₂ dilution. Considering the initial cell performance, the one with 250 °C i layer has lower V_{oc} and more red light collection, which is due to lower band gap at higher deposition temperature, as previously shown in Figure 3-10. However, during the time of i layer deposition at 250 °C, the p layer originally deposited at 200 °C would get annealed at higher temperature which also results in it having a lower band gap. The lower band gap of the window layer would increase its parasitic absorption which reduced QE collection at short wavelength as shown in Figure 3-14. The window layer could be optimized with higher band gap at 250 °C to improve the current collection.

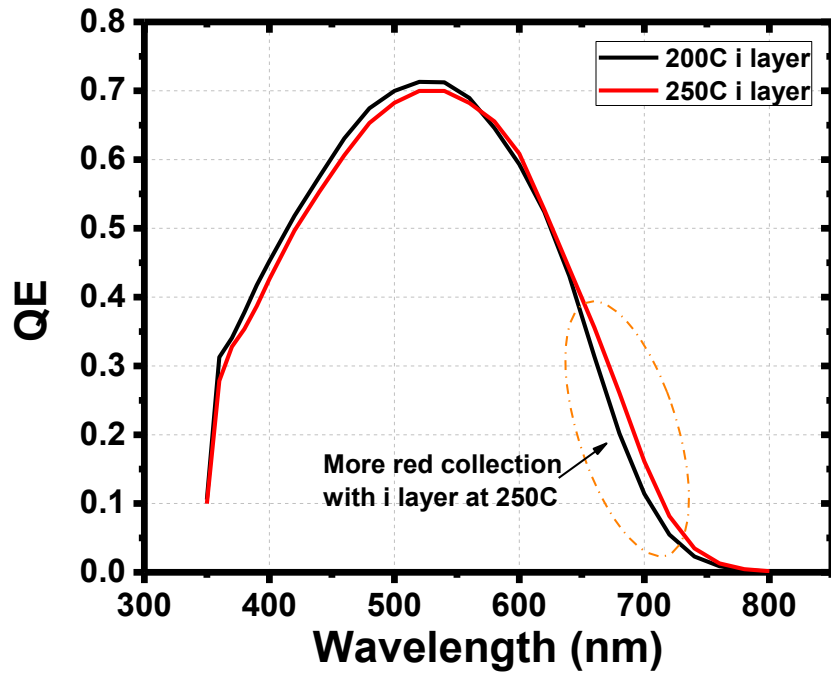


Figure 4-13 QE curves of devices with 200 °C and 250 °C i layer, before light soaking

Besides the i layer at higher temperature, lower R_{mf} could also be reached by H_2 dilution. A baseline p-i-n solar cell was fabricated with intrinsic layer deposited with H_2 dilution $R=5(H_2/SiH_4= 50/10)$. The film was deposited at 1.25 Torr with H_2 dilution, instead of 0.5 Torr, to achieve uniform plasma and reasonable growth rate. Such process condition also leads to relatively good Si-H bonding properties for cell stability, with $R_{mf}= 7.4\%$ and $C_H=10.8\%$. The solar cell stability results are shown in Appendix A.

4.4.3 Effect of growth temperature and H₂ dilution with Si₂H₆ additive and stability performance

This section will show the solar cell results of i layers deposited with Si₂H₆ additive and H₂ dilution. The main discussion focus on device performance correlating with materials characterization results which have been presented in 4.3.2.

Table 4-4 list the initial J-V results of the p-i-n solar cells with i layer properties shown from Figure 4-3 to 4-6. H concentration in the i-layer was 9~13%.

Table 4-4 A-Si:H p-i-n cell results with different i layer conditions. Initial cell performance and % degradation after LS shown. Cells without Si₂H₆ (SiH₄/Si₂H₆/H₂=10/0/50) are in bold. All others are with SiH₄/Si₂H₆/H₂=9/1/50. All devices deposited at 200°C except for the last entry deposited at 250°C. i layer deposited at 1.25 Torr (white background) or 2.5 Torr (tan background)

Cell	SiH ₄ / Si ₂ H ₆ /H ₂ (sccm)	RF (W)	GR (A/s)	R _{mf} (%)	V _{oc} (V)	J _{sc} (mA/ cm ²)	FF (%)	Eff (%)	Eff Degad %
1	10/0/50	30	1.8	7.4	0.882	11.6	72.5	7.4	20%
2	9/1/50	30	2.3	12.4	0.891	11.7	73.3	7.7	22%
3	9/1/50	70	3.3	4	0.877	11.9	70.9	7.4	26%
4	10/0/50	90	3.5	5.8	0.922	10.7	71.5	7.0	23%
5	9/1/50	90	5.2	15.9	0.929	10.6	71.4	7.1	22%
6	9/1/50	30	3.8	44.3	0.896	10.4	68.2	6.3	43%
7	9/1/50	90	5.0	5.9	0.882	11.4	73.4	7.4	22%

Regarding initial performance, the runs with 2.5 Torr have higher V_{oc} and lower J_{sc} due to higher i-layer E_g as shown in Figure 4-7. But for deposition at 250°C

and 2.5 T, V_{oc} decreases and J_{sc} increases due to the reduction in i layer E_g . An initial efficiency of 7.4% is achieved for i-layer deposited with Si_2H_6 additive at a growth rate of $> 5A/s$, which is similar to the baseline cell grown at 1.8 A/s without Si_2H_6 additive. Regarding efficiency degradation after 250 hours light soaking, Cell #6 with very high dyhydride bonding concentration $R_{mf}=44.3\%$ has the worst initial performance and largest degradation. Comparing with degradation of $>30\%$ for the un-optimized devices with no H_2 dilution, the optimized devices in Table 3-5 with H_2 dilution degrade $\sim 20-25\%$ while the growth rate is high $>5 A/s$. The result above indicates that cells with Si_2H_6 additive, besides the enhanced growth rate, behave the same as cell without additive regarding effect of E_g and substrate temperature.

4.5 Summary

In this chapter, enhanced growth rate and high quality deposition of a-Si:H with gas phase additives had been introduced. Materials properties such as E_g , R_{mf} , C_H , and deposition rate were presented to understand the effect of variable deposition conditions, such as Si_2H_6 additive, H_2 dilution, deposition temperature, pressure and RF power. The key result from this chapter indicates the benefit of Si_2H_6 additive for higher growth rate results in comparable initial or stabilized device behavior as without additive. Gas phase additive has thus been proven to be a promising approach of enhanced growth rate of high quality a-Si:H film deposition.

It had been found that:

- Simultaneous increase in growth rate and low microstructure factor (R_{mf}) in a-Si:H films can be achieved by increasing plasma power. The low R_{mf} obtained at high power and high growth rate is due to the role of atomic H, which would be further discussed in Chapter 6 of plasma diagnostic.
- With H_2 dilution, a large increase $\sim 60\%$ in growth rate was observed by addition of a small amount of 10% Si_2H_6 additive (1.7% in SiH_4+H_2 gas mixtures). The enhanced growth rate is more than the excess Si atoms which indicates the introduction of Si_2H_6 additive enhanced the dissociation of SiH_4 . Higher pressure results in more effective GR enhancement by Si_2H_6 additive. Thus Si_2H_6 additive beneficial might be more effective at high power and high pressure region. Lower R_{mf} could also be reached by using higher growth temperature or H_2 dilution.
- Considering the initial, as well as after light soaking performance of the a-Si:H p-i-n solar cells, the addition of 10% Si_2H_6 additive has no negative or positive influence even when tripling the growth rate.

Chapter 5

NANOCRYSTALLINE SILICON FILM DEPOSITION AND CHARACTERIZATION

5.1 Introduction

Compared to amorphous silicon, nanocrystalline silicon (nc-Si:H) has lower band gap, better stability performance as well as higher mobility, which make the materials suitable for many opto-electronic device applications such as photo voltaic (PV) cells, thin film transistors (TFT) and image sensors. Nc-Si:H films are normally deposited by Plasma Enhanced CVD (PECVD), which allows the cost-effective large area manufacturability with low temperature process. Additionally, the growth of nc-Si:H films requires high discharge power combined with high hydrogen dilution in standard RF (13.56 MHz) PECVD process, which results in low growth rate. The nc-Si:H has also been deposited by Very High Frequency (VHF) plasma discharge in the frequency range of 40 to 100 MHz [21].

For PV application, nc-Si:H solar cell is typically used as bottom cell in Tandem structure. Due to the indirect band gap of nc-Si:H, relatively large thickness required for efficient light absorption, so growth rate is critical for high throughput industrial processing. nc-Si:H films are commonly processed by Silane (SiH_4) diluted with Hydrogen (H_2) discharge. The deposition of high growth rate nc-Si:H films is typically accomplished under high power and high pressure condition or higher

frequency plasma discharge, which benefits from higher electron density for SiH₄ dissociation. Considering the nc-Si:H device application especially for the solar cell application, the material properties is determined by the structure of the nc-Si:H, such as the crystalline volume fraction (X_c) or crystal orientation. The best intrinsic nc-Si:H film for solar cell is deposited at close to the amorphous/nanocrystalline transition region with crystalline volume fraction of ~50% [16]. It has been reported that better nc-Si:H cell performance is obtained with (220) oriented film with grain size ~25nm [17]. It is important to realize that the goal for a high efficiency solar cell is not 100% crystalline fraction but a nearly equal mixture of a-Si:H and nc-Si:H material. But for high throughput manufacturing of tandem a-Si:H/nc-Si:H cells, it must be deposited at $GR > 5$ A/s since the thickness of the nc-Si:H bottom cell is ~3 times thicker than the a-Si:H top cell.

The topic of this chapter will focus on the development of nc-Si:H deposition, materials characterization and solar cell application. First, the process condition such as SiH₄/H₂ dilution, RF power, Pressure, Plasma Frequency as well as gas phase additive will be explored and correlated with deposited nc-Si:H film properties such as growth rate, X_c , crystal size and crystal orientation. Second, the nc-Si:H solar cell application from the deposited film will be discussed, which will also include optimization of doping layer, back contact and texturing of TCO substrate. The insights provided by plasma analysis of nc-Si:H growth will be correlated with the material properties in Chapter 6.

5.2 Experiment

All the intrinsic nc-Si:H films discussed in this chapter were deposited in a capacitively coupled PECVD system either using RF 13.56 MHz or VHF 40.68 MHz plasma. SiH₄ and H₂ were delivered into the reactor through a gas showerhead, where the area of the powered electrode is 1100 cm² and the discharge gap is 1.4 cm. Films were deposited at different excitation frequency, plasma power and pressure. Also, the H₂ dilution was varied by changing the SiH₄ flow rate while keeping the H₂ flow rate fixed. The films were deposited on Corning 1737 glass at a temperature of 200 °C at a thickness ~1 μm. It has been reported that the structure of nc-Si:H is inhomogeneous at different thickness. Typically the crystalline volume fraction increases with film thickness at a given deposition condition as the grains coalesce [51]. However, the films deposited on a seed layer were found to minimize such thickness dependence of crystalline fraction [52]. The seed layer was processed with higher H₂ diluted SiH₄/H₂ discharge compared with nc-Si:H bulk deposition. Prior to each intrinsic nc-Si:H film deposition discussed in this chapter, a short (2mins) H₂ plasma treatment was followed by deposition of a thin (10nm) seed layer to avoid film peeling and to improve nc-Si:H structural homogeneity respectively.

The film thickness was estimated from a Dektak stylus profiler to calculate growth rate (GR). Raman spectroscopy was performed with 532 nm laser excitation to characterize the film structure. The Raman crystalline volume fraction (X_c) was calculated from three peaks deconvolution method [43]:

$$X_c = \frac{I_{510}+I_{520}}{I_{510}+I_{520}+I_{480}} \quad (5-1)$$

X-ray Diffraction was used to investigate the crystal growth and grain size.

The growth orientation was estimated by peak intensity ratio of Si (111), (220) and (311). The grain size (GS) was calculated by the full width of half maximum (FWHM) of different peaks using Scherrer Equation [45].

nc-Si:H p-i-n solar cells, with p type nc-Si:H /i nc-Si:H/n type a-Si:H, were fabricated to further understand the properties of nc-Si:H with a superstrate configuration on TEC 8 or textured Al doped ZnO (AZO) substrates, typically mixing each type in the same run. TEC 8 were coated with 2 nm ZnO to avoid reduction of Tin Oxide by atomic H, which is typically abundant in plasma discharge for nc-Si:H p layer deposition [53]. Al doped ZnO was textured at room temperature in a 0.1% HCl solution for 180 seconds. The substrate surface morphology was monitored by Atomic Force Microscopy (AFM) to investigate film structure and solar cell performance dependence on surface morphology. Al and ITO/Al were used as back contact of the p-i-n solar cell for comparison of their effect on solar cell performance.

5.3 Nc-Si:H Thin Film Deposition with Variable Parameters

In this section, the effect of H₂/SiH₄ dilution, RF power, deposition pressure, discharge frequency and gas phase additive (10% Si₂H₆ in SiH₄) were evaluated with respect to film growth rate and crystallinity of nc-Si:H films, where the substrate temperature was kept constant at 200°C.

5.3.1 Effect of H₂ dilution on nc-Si:H film deposition

The nc-Si:H thin film in this series was deposited at different H₂/SiH₄ dilution with fixed deposition pressure of 3 Torr, plasma frequency of 13.56 MHz and RF power of 300W. The H₂ flow was kept constant at 500 sccm, while SiH₄ varied from 7 sccm to 14 sccm. Since the SiH₄ was <3% of the total the pumping speed was relatively constant. Figure 5-1 presents the Growth Rate and Raman Crystal Volume Fraction (X_c) of Si thin films deposited under different H₂/SiH₄ dilution. When the SiH₄ flow increases from 7 sccm to 14 sccm, (with R=H₂/SiH₄ decrease from 71.4 to 35.7 respectively) the Growth Rate increases from 1.7A/s to 3.2 A/s, while X_c decreases from 68% (nc-Si:H) to 0% (a-Si:H).

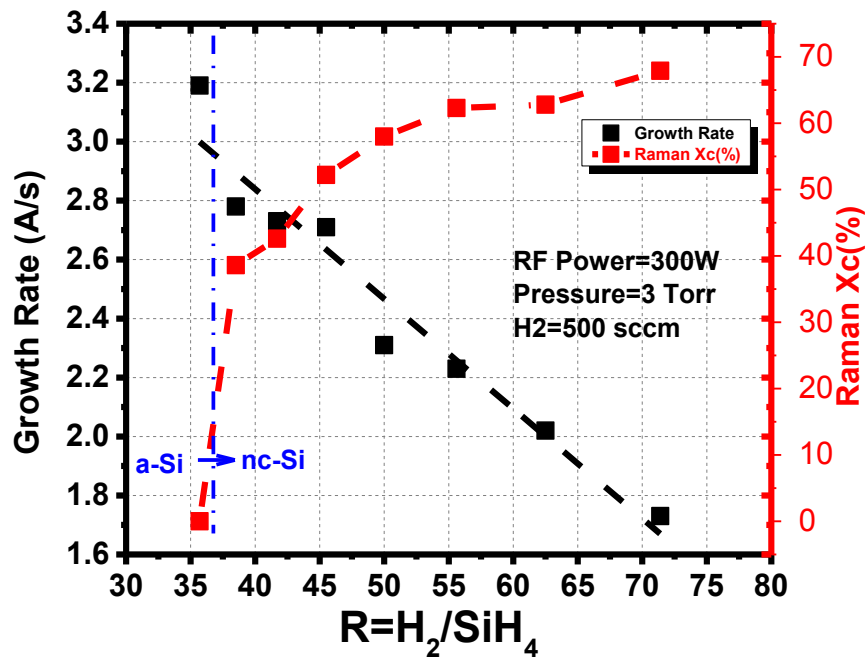


Figure 5-1 Growth Rate and X_c of films deposited with variable H₂/SiH₄ Dilution

Figure 5-2 shows the Raman Spectra of the films deposited with different SiH₄ flows showing the evolution of a-Si:H peak at 480 cm⁻¹ to the c-Si peak at 520 cm⁻¹ as the SiH₄ flow rate is changed. As the SiH₄ flow increases, the Raman peak shifts from the c-Si peak at 520 cm⁻¹ to lower wavenumber which might correlate with the smaller crystal size of the nc-Si:H structure [54, 55] and increase of a-Si:H phase. For SiH₄ flow at 14 sccm, the peak is centered at 480 cm⁻¹ indicating the film is completely a-Si:H.

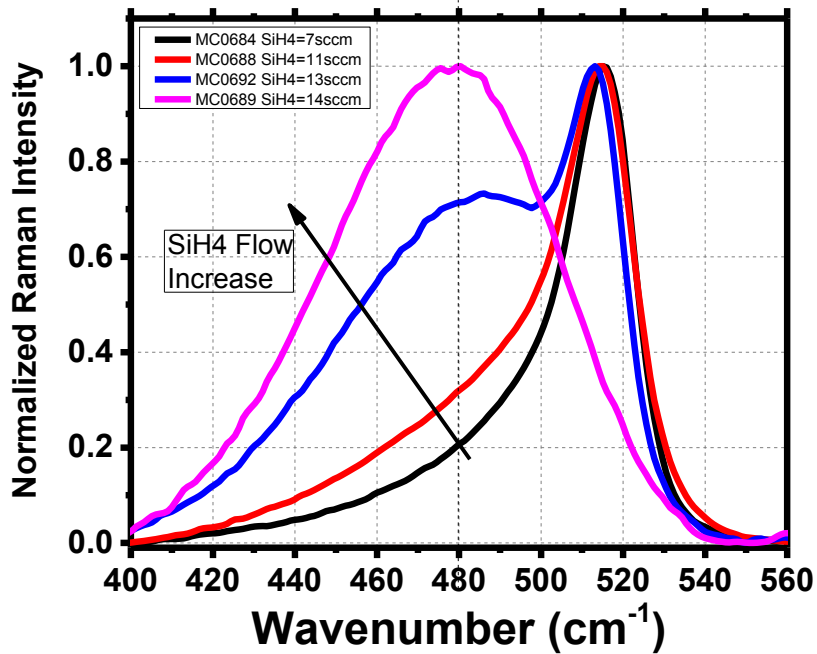
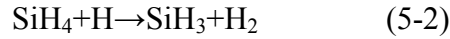


Figure 5-2 Raman Spectra of Si films deposited with different SiH₄ flow at H₂=500 sccm 3 Torr and RF power of 300W. The H₂/SiH₄ ratio varied from 71 to 36.

The results indicates that the structure of the Si film is strongly related to the H₂/SiH₄ ratio and that nc-Si:H film is formed at the high H₂/SiH₄ ratio when the

atomic H in the discharge is relatively high. By increasing SiH₄ flow, the atomic H flux to the surface of the growing film is reduced due to the H annihilation by reaction with SiH₄ at gas phase:



which results in an increase in the Si radical concentration due to higher SiH₄ dissociation, and thus higher growth rate of the film deposition.

5.3.2 Effect of RF Power on nc-Si:H deposition

To evaluate the effect of RF Power on nc-Si:H deposition, a series of films were deposited by varying the power from 100W to 400W keeping the H₂/SiH₄=500/7 and 3 Torr constant. Figure 5-3 shows the Growth rate and X_c of the films in RF Power series.

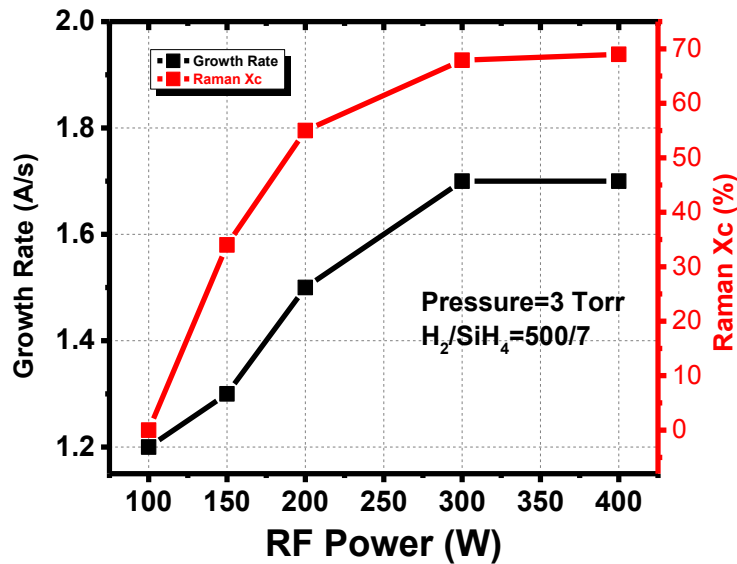


Figure 5-3 Growth Rate and X_c of Si films deposited at different RF power at H₂/SiH₄=500/7, 3 Torr

The film deposited 100W is completely a-Si:H with growth rate at 1.2 A/s. At 150W, the structure of Si film transitions from a-Si:H to nc-Si:H. Both growth rate and X_c increased with higher power up to 300 W. No significant increase of growth rate or X_c is found by increasing RF power beyond 400W. From 100W to 300W, the higher power results in an increase in electron density from ionization, which leads to higher Si radical concentration from the enhancement dissociation of SiH_4 , thus higher growth rate. However, as the SiH_4 gets completely depleted, further increasing power did not result in higher Si radical flux to deposition surface, which could explain the growth rate saturation from 300 W to 400 W as shown in Figure 5-3. Higher X_c at high power may result from relatively larger H concentration. The mechanism will be investigated by plasma characterization discussed in Chapter 6.

5.3.3 Effect of Deposition Pressure on nc-Si:H film deposition

The films in this series were deposited with pressure varying from 3 Torr to 8 Torr at constant $\text{H}_2/\text{SiH}_4=300/8.5$ and constant RF Power of 515 W. Based on Paschen's Curve, the plasma breakdown voltage of the gas is a function of the product of pressure times discharge gap. So, the RF power of 515 W was chosen to achieve plasma ignition and maintain uniform plasma in the pressure range from 3 to 8 Torr

Figure 5-4 shows the growth rate and X_c of the nc-Si:H films deposited at different pressures. The nc-Si:H film deposited at 3 Torr has growth rate 2.7 A/s with Raman X_c at 67%. With higher deposition pressure, both growth rate and Raman X_c

increase and maximized at 5 Torr with 4.1 A/s and $X_c \sim 80\%$ respectively. Further increasing the deposition pressure results lower growth rate as well as lower Raman X_c . The initial increase in growth rate when the pressure increases from 3 to 5 Torr can be due to enhanced dissociation due to more electron- molecule impact at higher pressure. However, it's not straight forward to explain the simultaneous reduction of growth rate and X_c at high pressure (>5 Torr). To further understand this observation, the deposition plasma has been characterized by variable parameters which will be discussed in Chapter 6.

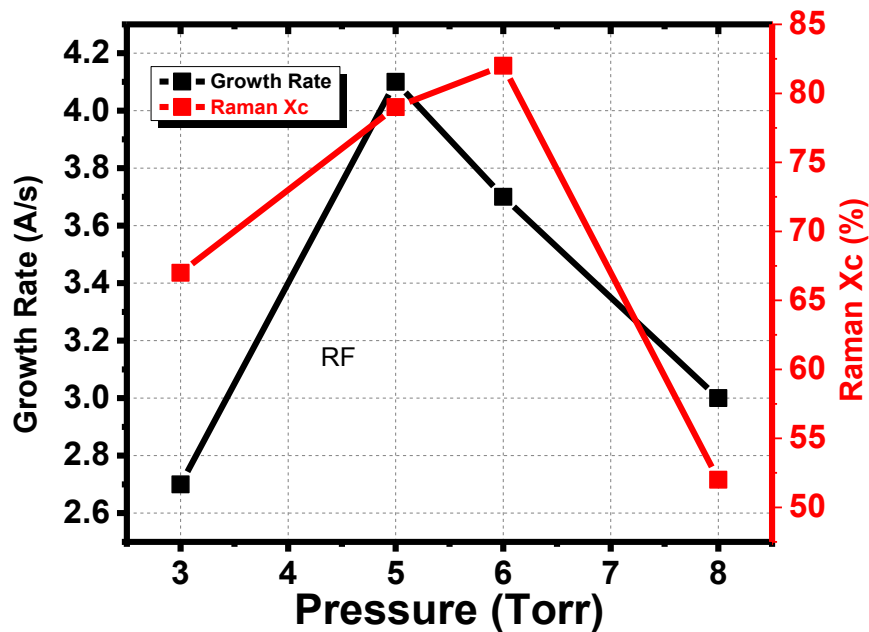


Figure 5-4 Growth Rate and Xc of Si films deposited at different Pressure at $H_2/SiH_4=500/8.5$, RF 515W

5.3.4 Effect of RF Frequency on nc-Si:H film deposition

In this section, nc-Si:H film grown at 40.68 MHz (VHF) are compared to films grown at 13.56 MHz (RF) where it is well known that the benefits of VHF for deposition of nc-Si:H films includes higher electron density, lower electron temperature and higher growth rate.

Table 5-1 lists the deposition conditions and Figure 5-5 shows the film Growth Rate and crystalline volume fraction for nc-Si:H films grown by VHF plasma as a function of H dilution ratio (H_2/SiH_4). For films deposited at RF plasma at 300 W and pressure of 3 Torr, the film structure becomes amorphous for $R < 35$ (Figure 5-1). However, in VHF plasma, the film remains nano-crystalline with $X_c > 70\%$ even when the R reduced down to 10 (Table 5-1). When R is reduced from 35 to 11 by keeping a constant SiH_4 flow of 8.5 sccm and reducing the H_2 flow from 300sccm to 100sccm, the growth rate increases linearly from 2.6 A/s to 3.9 A/s, while X_c does not change appreciably, remaining $>70\%$ as shown in Fig.4-5. At a H_2 flow of 100 sccm, the growth rate increases to 4.6 A/s when SiH_4 flow is increased to 10 sccm while maintaining the film crystallinity, $X_c > 70\%$. By comparing MC 1249 and MC 1258, it can be concluded that combination of increasing SiH_4 partial pressure and reducing total gas flow of $SiH_4 + H_2$ is more beneficial for increasing growth rate.

Over all, VHF has 53% higher growth rate than RF (2.6A/s vs 1.7A/s) for nc-Si:H deposition with similar process conditions and the a-Si:H to nc-Si:H phase transition threshold occurs at $R < 10$ for VHF films compared to $R > 35$ for RF films. Thus nc-Si:H deposited by VHF requires a relatively lower H_2 flow for high growth

rate due to longer radical residence time and higher SiH₄ partial pressure. The highest nc-Si:H growth rate achieved in this research is 7.2A/s with X_c=73% by VHF at 450W with H₂/SiH₄=100/20 at 3 Torr.

Table 5-1 Nc-Si:H growth rate, X_c with different H₂/SiH₄ ratio by VHF at 3 Torr 250W

Sample ID	SiH ₄ (sccm)	H ₂ (sccm)	Ratio (H ₂ /SiH ₄)	Growth Rate (A/s)	X _c (%)
MC1249	8.5	300	35.3	2.6	73.4
MC1253	8.5	200	23.5	3.4	76.9
MC1255	8.5	150	17.6	3.7	83.5
MC1256	8.5	100	11.8	3.9	82.2
MC1258	10	100	10	4.6	75.0

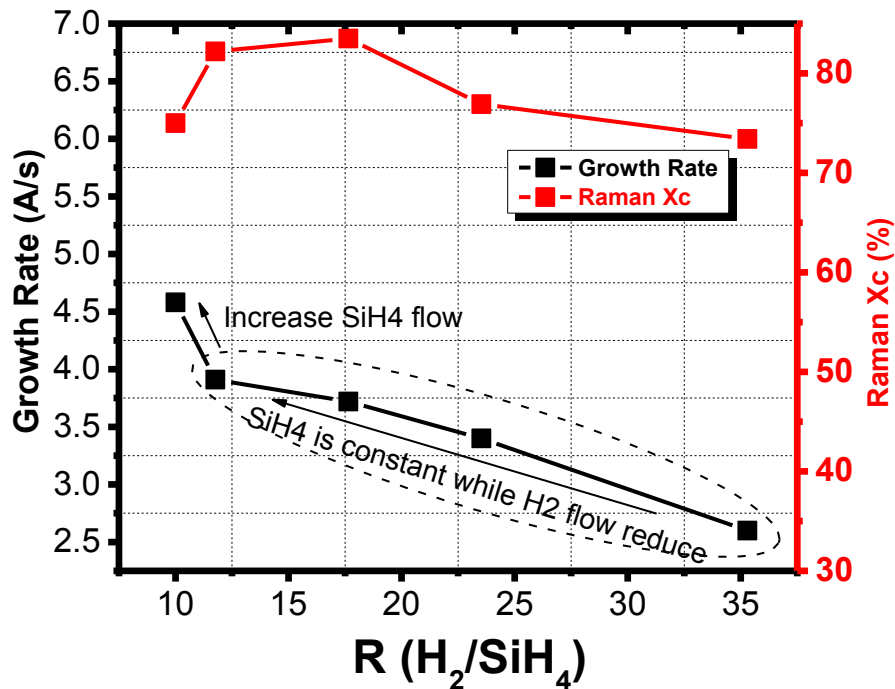


Figure 5-5 Growth Rate and Raman X_c of nc-Si:H deposited by VHF as a function of H₂/SiH₄ ratio

5.3.5 nc-Si:H film deposition with Si₂H₆ additive

In this section, effect of the addition of small amounts of Si₂H₆ to the H₂/SiH₄ gas mixture on the growth rate and crystalline fraction of the nc-Si:H film are evaluated. Figure 5-6 shows the Raman Spectra of nc-Si:H baseline film deposited by RF discharge with H₂/SiH₄ and with the addition of 20% Si₂H₆, that is $F_{\text{Si}_2\text{H}_6}/[F_{\text{Si}_2\text{H}_6}+F_{\text{SiH}_4}]=0.2$ where F represents the flow in sccm. The Raman Spectra shows the similar Si-Si bond peaks from 310 to 520 cm⁻¹, two-phonon excitation peak ~960cm⁻¹ as well as Si-H bond from 1800cm⁻¹ to 2200⁻¹, indicating nc-Si:H deposited with and without Si₂H₆ have similar chemical bonding.

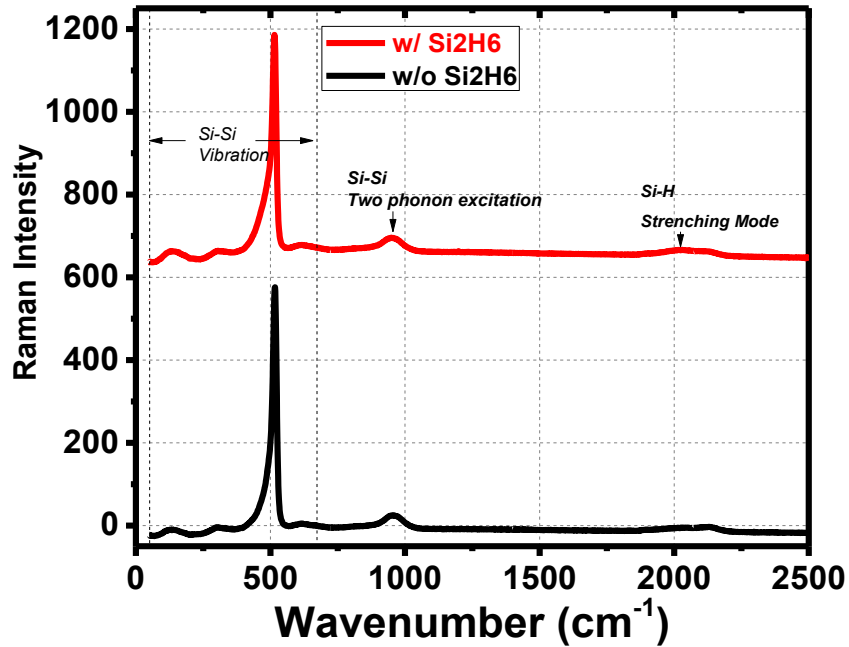


Figure 5-6 Raman Spectra of nc-Si:H deposited by H₂/SiH₄ with and without Si₂H₆

Table 5-2 presents the Growth Rate and Raman Xc of nc-Si:H films deposited both RF and VHF plasma at powers of 250 & 300W at 3 Torr using different gas compositions and flows with and without Si₂H₆ additive. There is no significant increase in growth rate with the adding Si₂H₆ additive for films grown using RF and ~20% increase in growth rate for films deposited by VHF plasma. The 20% or 10% Si₂H₆ additive in gas mixture results in ~10% growth rate enhancement, which is proportional to the more Si atoms inside plasma by adding Si₂H₆. The Raman Xc decreases with Si₂H₆ additive, which might result from lower H and Si radical ratio inside plasma to be shown in Chapter 6.

As mentioned in Chapter 4, Si₂H₆ has lower ionization threshold energy than SiH₄ and H₂. The electron density is expected to be increased with Si₂H₆ additive. Thus the SiH₄ dissociation rate would increase due to higher electron density. In nc-Si:H deposition region, the growth rate enhancement by adding Si₂H₆ is just proportional to excess Si atoms from Si₂H₆ additive. First, considering the Si₂H₆ reaction rate constant $k_{\text{diss}}/k_{\text{ion}} > 10$ [56], however, larger percentage of Si₂H₆ molecule is depleted rather than ionized within the SiH₄/Si₂H₆ with high power. Second, the SiH₄ is close to depletion in nc-Si:H deposition region. (e.g. Power > 300W in Figure 5-3) Thus less beneficial effect has been observed for growth rate enhancement by Si₂H₆ additive in nc-Si:H growth region.

Table 5-2 RF and VHF Growth Rate and Raman Xc of nc-Si:H deposited by H₂/SiH₄ with and without Si₂H₆

Plasma	SiH₄ (sccm)	Si₂H₆ (sccm)	H₂ (sccm)	Growth Rate (Å/s)	X_c (%)
RF 3T, 300W	10	0	500	2.6	69%
	8	2	500	2.8	56%
VHF 3T, 350W	15	0	100	6	73%
	13.5	1.5	100	6.7	65%

5.4 Nc-Si:H Film Structural Properties

Most of the literature on nc-Si:H solar cells indicate that the cell efficiency becomes maximum when the nc-Si:H film has grain size of ~20nm with preferential (220) orientation. In this section, nc-Si:H films are characterized by XRD, to determine the grain size and orientation and correlated with the deposition conditions and film properties.

5.4.1 Raman Crystal Volume Fraction and XRD Grain Size

Raman Spectra is the most common method to characterize the crystal volume fraction of the nc-Si:H. It is important to understand the correlation between Raman Xc of the structure and Grain Size.

Figure 5-7 presents the Raman Spectra of 2 different nc-Si:H baseline films deposited by Hot-Wire CVD (HWCVD) and PECVD, which was grown by RF Power=300W, H₂/SiH₄=500/9 at 3 Torr. Both films have similar crystal volume fraction. However, the XRD Spectra Intensity of nc-Si:H by PECVD is much weaker

compared with HWCVD nc-Si:H, as shown in Figure 5-8. The grain size of the film deposited by HWCVD is ~20 nm but only ~ 2 nm for the film grown by PECVD.

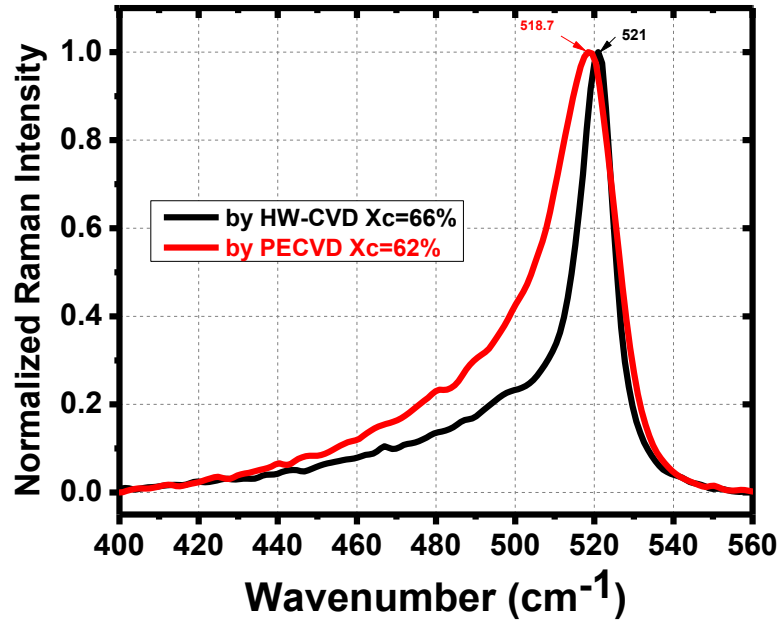


Figure 5-7 Raman Spectra of nc-Si:H deposited by HWCVD and PECVD with similar X_c

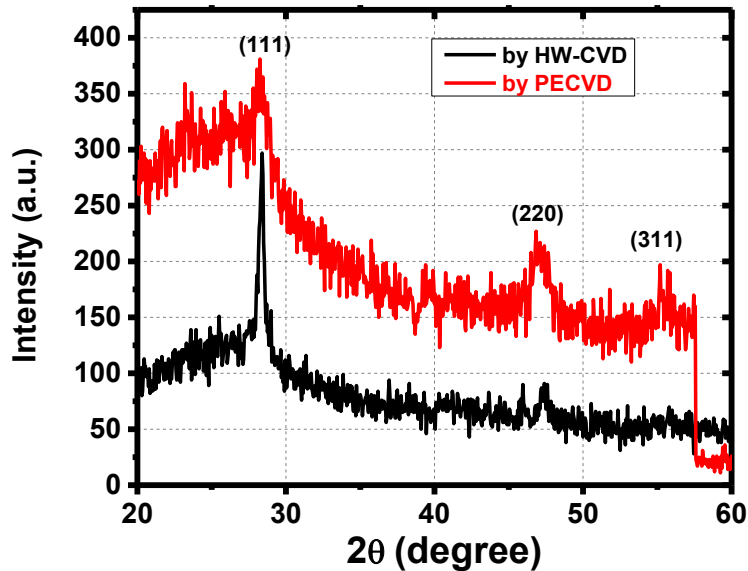


Figure 5-8 XRD Spectra of nc-Si:H deposited by HW-CVD and PECVD

By comparison of these 2 films with similar Raman X_c , it is clear that high X_c does not necessarily imply large grain size of nc-Si:H. The Strong Raman Crystal Peak but weak XRD signal may suggest the Raman signal is from the large amount of small size sub-grain, which has negligible contribution to XRD signal.

5.4.2 Grain Size and Growth Orientation of nc-Si:H by RF

As discussed above, nc-Si:H structure properties are highly dependent with the deposition conditions. In order to explore the process condition and the film structure, a further series of nc-Si:H are deposited and characterized.

Figure 5-9 shows the XRD pattern of the nc-Si:H films grown at different pressure from 3 Torr to 8 Torr with $H_2/SiH_4=300/8.5$ and RF power 515W. Table 5-3

lists the XRD analysis results as well as the growth rate and Raman X_c of the nc-Si:H films.

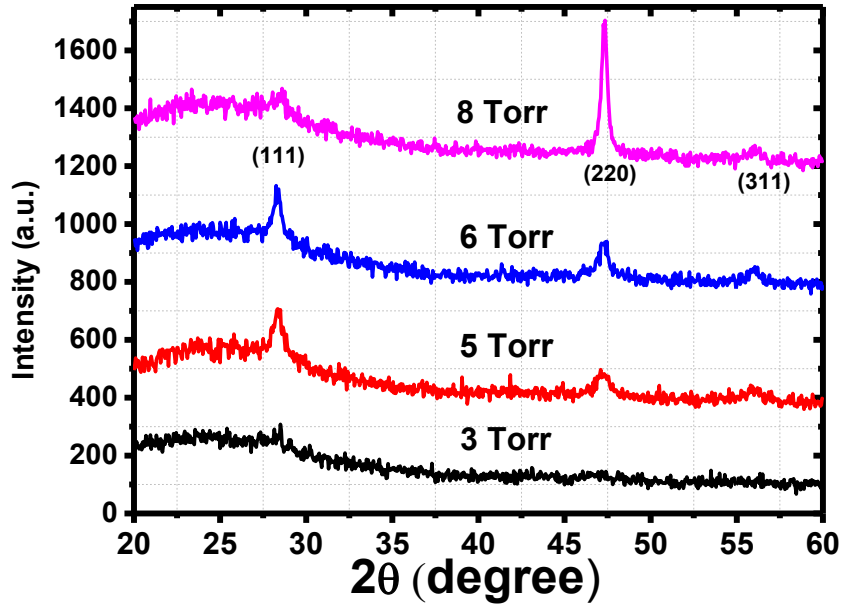


Figure 5-9 XRD pattern of nc-Si:H deposited at different pressure by RF 515W

Table 5-3 Raman X_c , growth rate, XRD analysis results for nc-Si:H film deposited by RF

Pressure (Torr)	X_c (%)	GR (Å/s)	(111) Height	(220) Height	$I_{(220)}/I_{(111)}$	(111) GS (nm)	(220) GS (nm)
3	67	2.7	NA	NA	NA	NA	NA
5	79	4.1	98	49	0.67	13	10
6	82	3.7	100	84	1.43	16	14
8	52	3	35	312	7.9	16	24

For the nc-Si:H deposited at 3 Torr, there is no significant XRD peak observed, indicating small crystal grain size $<2\text{nm}$. By increasing the pressure to 5 Torr, grain size calculated from both (111) and (220) peaks increases. The integrated intensity ratio $I_{(220)}/I_{(111)}=0.67$ indicates the film is almost random orientated. The gain

size keeps increasing with higher deposition pressure. At 8 Torr, The film is deposited near the amorphous/crystalline phase transition region with X_c around 50%. The grain size achieves 24 nm calculated from (220) peak with strong preferential (220) orientation.

Figure 5-10 presents Raman spectra comparison of three films deposited by RF at 515W. Two of them are listed in Table 5-3. A film with higher H-dilution is shown as well. A strong crystalline phase peak ($\sim 520 \text{ cm}^{-1}$) is confirmed for the film deposited at 3 Torr, even though there was no XRD peaks detected as discussed above. By increasing the pressure from 3 Torr to 8 Torr, the Raman peak shifts from 517 cm^{-1} to 519 cm^{-1} correlating with larger grain size at 8 Torr. The FWHM of crystalline peak ($\sim 520 \text{ cm}^{-1}$) decreases from 15 cm^{-1} to 10 cm^{-1} . The larger FWHM may indicate the wider size distribution inside the film.

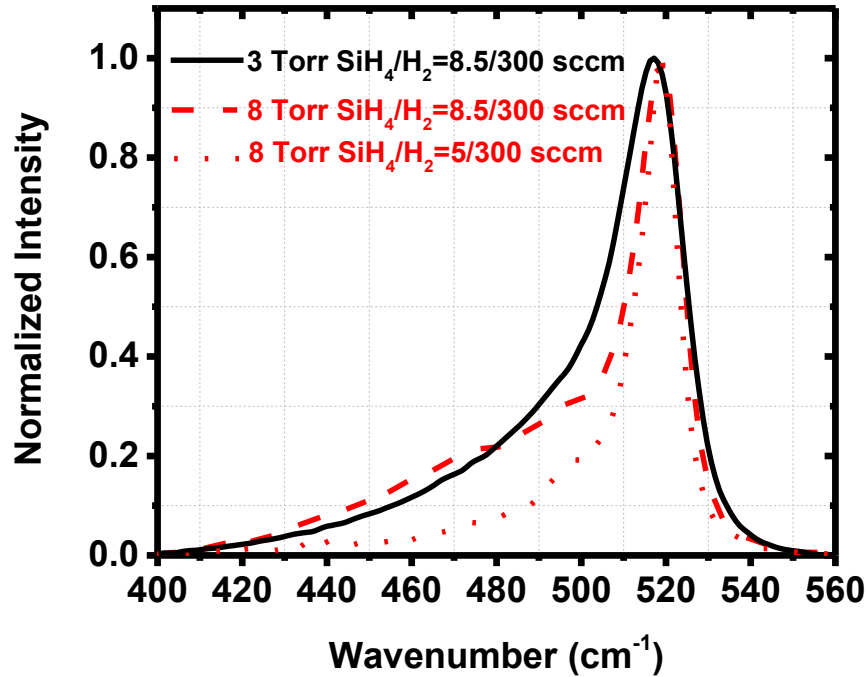


Figure 5-10 Raman spectra of nc-Si:H film at 3 Torr and 8 Torr by RF 515W

The above experiment confirms that the deposition pressure is the key parameter to control the grain size of the nc-Si:H by RF plasma. The film grown at lower pressure shows small grain size in structure even with high crystal volume fraction. Larger grain sizes are achieved at high deposition pressure with RF plasma.

5.4.3 Evolution of nc-Si:H growth orientation

Figure 5-11 presents the XRD pattern of nc-Si:H films deposited with different H_2/SiH_4 dilution at 8 Torr by RF 515W. By reducing H_2/SiH_4 , the preferential growth change from (111) to (220) orientation, which is consistent with the results reported by other group [17, 57]. It's possible that H etches <220> plane faster than <111>. Such

<220> preferential etch process with H is eliminated by adding SiH₄ thus the film show (220) orientated with lower H₂/SiH₄. The mechanism of relationship between H₂/SiH₄ dilution and growth orientation is still under investigation.

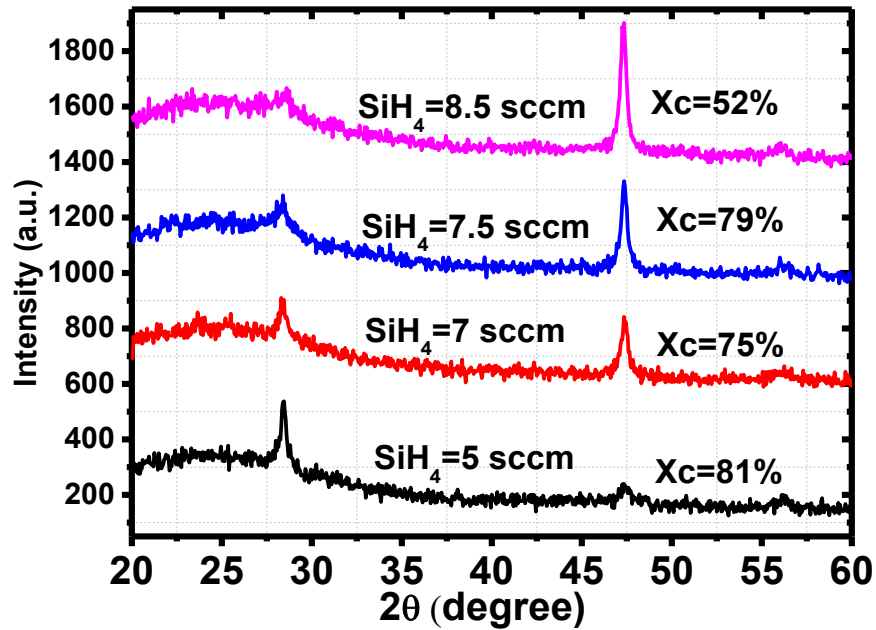


Figure 5-11 XRD pattern of nc-Si:H films different dilution at 8 Torr H₂=300sccm by RF 515W

5.4.4 Grain Size and Growth Orientation of nc-Si:H by VHF

Another series of nc-Si:H films were deposited by VHF at 3 Torr, 250W, H₂=300sccm while the SiH₄ flow was varied from 8.5 sccm to 17 sccm. Figure 5-12 presents the XRD pattern of the films in this series at different dilution. The grain size for VHF films (calculated with FWHM of (220) peak) is ~27 nm, while for RF films no significant peak is observed with comparably high X_c ~ 75%. Unlike the trend

shown in Figure 5-11, films deposited by VHF have all (220) preferential orientation, which is independent with H_2/SiH_4 ratio.

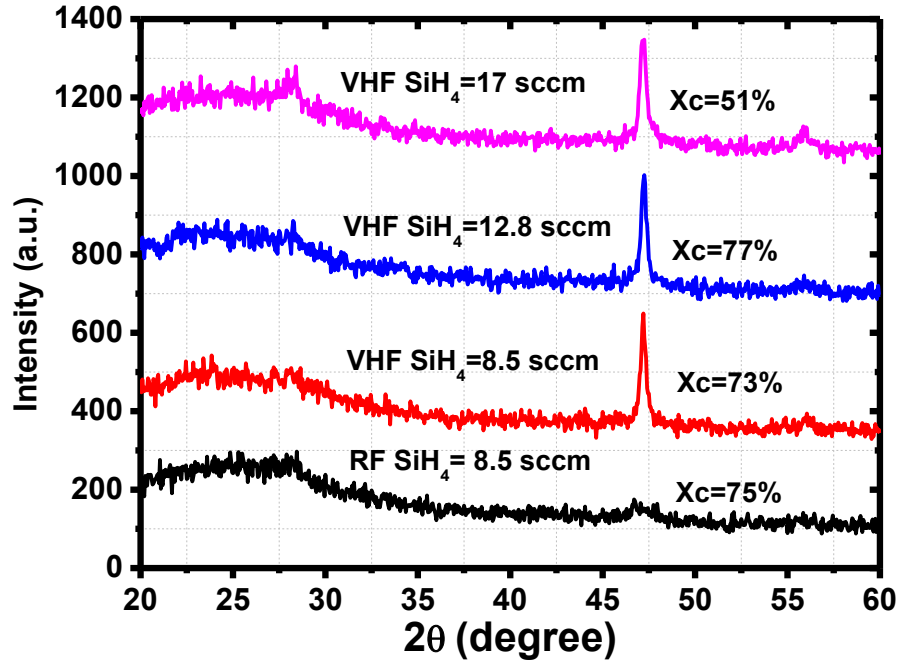


Figure 5-12 XRD pattern of nc-Si:H by RF and VHF at 3 Torr with different SiH_4 flow

5.4.5 Structural properties of nc-Si:H deposited with Si_2H_6 additive

Table 5-4 lists the deposition parameters of nc-Si:H deposited by RF at 515W, 8 Torr and $H_2=300$ sccm, and VHF at 350W, 3 Torr and $H_2=100$ sccm with and without Si_2H_6 additive. Raman Spectra confirms all films have a high crystal volume fraction. Figure 5-13 presents the XRD patterns of the four films. Compared with nc-Si:H deposited by RF H_2/SiH_4 , adding 10% Si_2H_6 change the growth orientation from (111) to (220), which might result from the effect of H/Si on preferential growth orientation discussed in 5.4.2 However, with VHF, there is no significant change of growth orientation with Si_2H_6 additive since the films were already highly (220)

oriented without additive, with no discernible differences in grain size (~28 nm).

Therefore the Si₂H₆ additive in VHF plasma increased the film growth rate and achieved 6.7 A/s without any apparent differences in film structure (grain size, crystal fraction or orientation)

Table 5-4 Nc-Si:H deposited by RF and VHF with and without Si₂H₆ additive

Condition	SiH₄ (sccm)	Si₂H₆ (sccm)	H₂ (sccm)	Raman X_c	GR (A/s)
RF 515W 8 Torr	5	0	300	81%	2.0
	4.5	0.5	300	81%	2.6
VHF 350W 3 Torr	15	0	100	73%	6
	13.5	1.5	100	65%	6.7

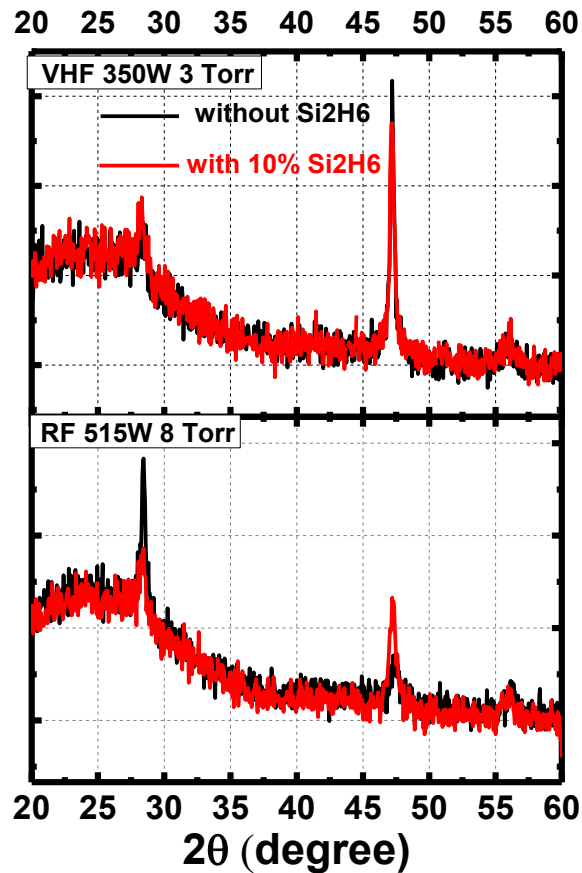


Figure 5-13 XRD pattern of nc-Si:H deposited by RF and VHF with and without Si₂H₆

5.5 Nc-Si:H Solar Cell Device Performance

To further understand the nc-Si:H materials properties, p-i-n nc-Si:H solar cells were fabricated for comparison of different nc-Si:H film process conditions. Figure 5-14 shows the configuration of the device. nc-Si:H p type layer is deposited at high H₂ dilution with H₂/SiH₄/B₂H₆=300/2/0.8 with RF power of 200W at 1.5 Torr. A 20nm nc-Si:H p-layer deposited under above condition has with X_c=40% and conductivity 0.1S/cm. A nc-Si:H i-layer, with growth rate of 4Å/s and X_c~50% with

(220) orientation (when deposited on glass) is deposited with $H_2/SiH_4/Si_2H_6=7.7/0.8/300$ by VHF 250W 3Torr. An a-Si:H n type layer is deposited by DC, which is the same n layer used for a-Si:H p-i-n cells in Chapter 4. Two different back contacts, Al and ITO/Ag are used for comparison. The Al is simpler to deposit but the ITO/Ag has higher reflection and is known to enhance the long wavelength response of a-Si:H and nc-Si:H solar cells.

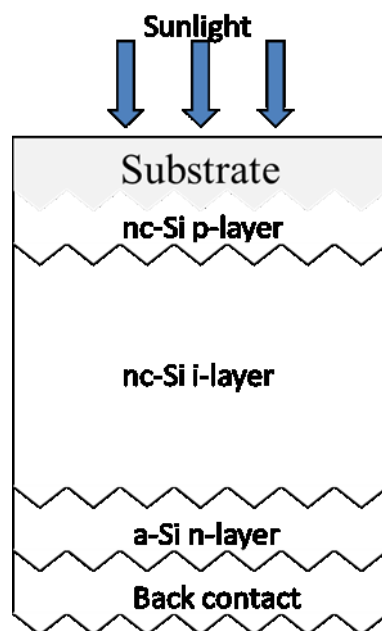


Figure 5-14 nc-Si:H p-i-n solar cell configuration

5.5.1 Solar cell performance on ZnO-coated SnO₂:F/glass (TEC 8 brand) and Al doped ZnO/glass substrates

nc-Si:H solar cells are fabricated on ZnO coated TEC8 (Z-TEC8) and Textured Al doped ZnO (AZO) for comparison. Table 5-5 lists the JV performance of two solar cells processed with same condition but different substrates. On ZnO coated textured

SnO₂:F TEC8 substrate, the V_{oc} is close to 0.4 V and FF is about 61%. However, V_{oc} and FF is much higher on AZO for the same cell fabrication condition.

Table 5-5 JV performance of nc-Si:H p-i-n solar cell with Al back contact on different substrates

Substrate	V_{oc} (V)	J_{sc} (mA/cm ²)	FF (%)	E_{ff} (%)
Z-TEC8	0.392	14.7	60.6	3.5
AZO	0.452	12.2	69	3.8

In order to further understand the effect of different substrate, AFM is used to characterize the surface morphology and the nc-Si:H film structure on the solar cell substrates is investigated by XRD.

Figure 5-15 presents the XRD pattern of 2 solar cells, with p-i-n layers on Z-TEC8 and AZO, compared with glass substrate. Table 5-6 lists the grain size from XRD measurement.

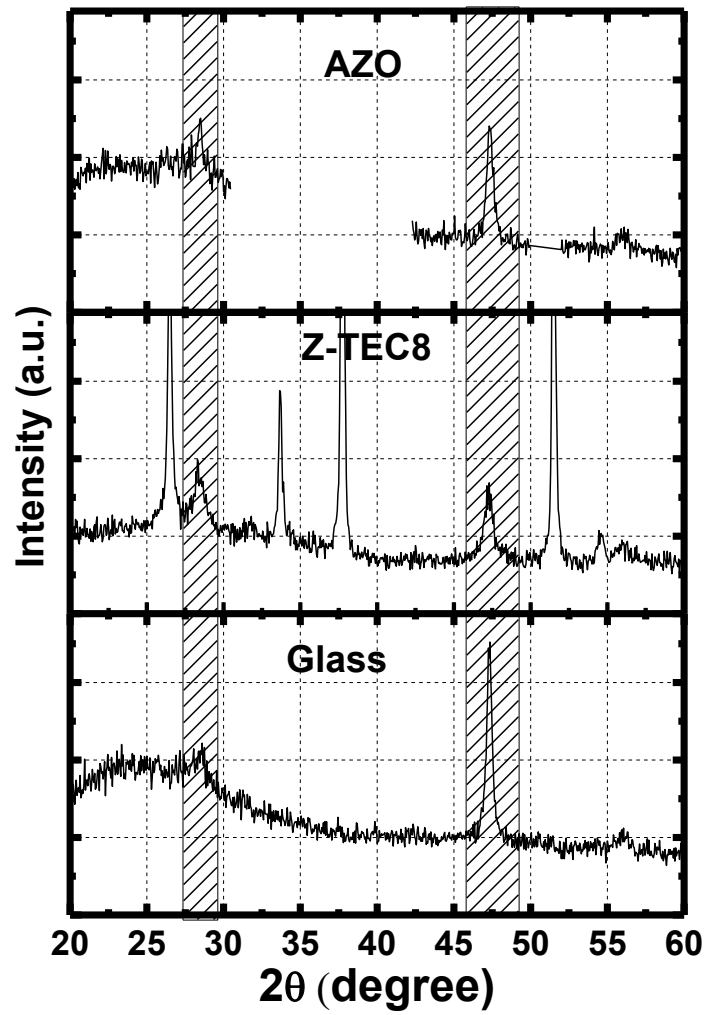


Figure 5-15 XRD pattern of nc-Si:H solar cell on Glass, Z-TEC8 and AZO

Table 5-6 Grain Size of nc-Si:H on different substrates

Substrate	(111) Peak Grain Size (nm)	(220) Peak Grain Size (nm)
Glass	10	24
Z-TEC8	12	15
AZO	13	21

It has been observed that the substrates significant influence on growth orientation. XRD measurement shows nc-Si:H grown on glass and AZO are both (220) orientation but randomly oriented on Z-TEC8. Moreover, the grain size of nc-Si:H, calculated from FWHM of XRD peaks, has significant difference on Z-TEC8, AZO or Glass. The nc-Si:H solar cell grown on AZO shows larger (220) peak grain size compared with Z-TEC8, with 21nm and 15nm respectively.

Figure 5-16 shows the tilted Top view image of Z-TEC8 and AZO surface by AFM measurement and Figure 5-17 presents the line scan profile of top surface of these two substrates prior to any deposition. The surface of Z-TEC8 is rougher than AZO, with R_{ms} 25.2 nm and 17.6 nm. Moreover, the line scan indicates that Z-TEC8 shows a rough V shape while AZO is relatively smooth U shape. As shown in Table 5-5, the solar cell grown on the V shape Z-TEC8 has lower V_{oc} and FF compared with the one on U shape AZO. The lower V_{oc} and FF indicates worse i layer bulk quality and more electron-hole recombination inside i layer for the nc-Si:H solar cell grown on V shape substrate. Note that the TEC-8 SnO₂:F texture was optimized for commercial production of large a-Si:H solar modules. It is now known that nc-Si:H devices require a different texture for best performance.

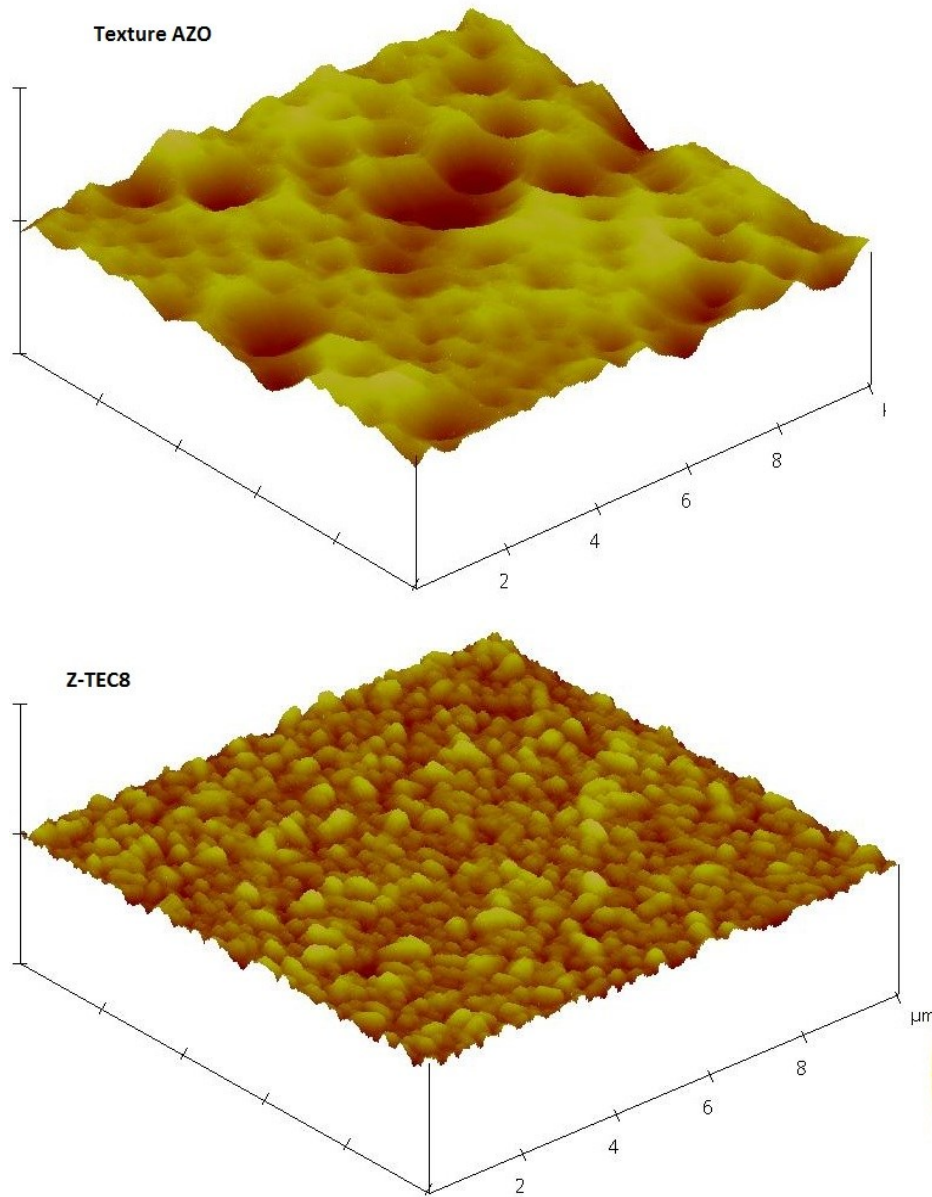


Figure 5-16 AMF Tilt Top View of AZO and Z-TEC8 surface prior to any nc-Si:H film deposition

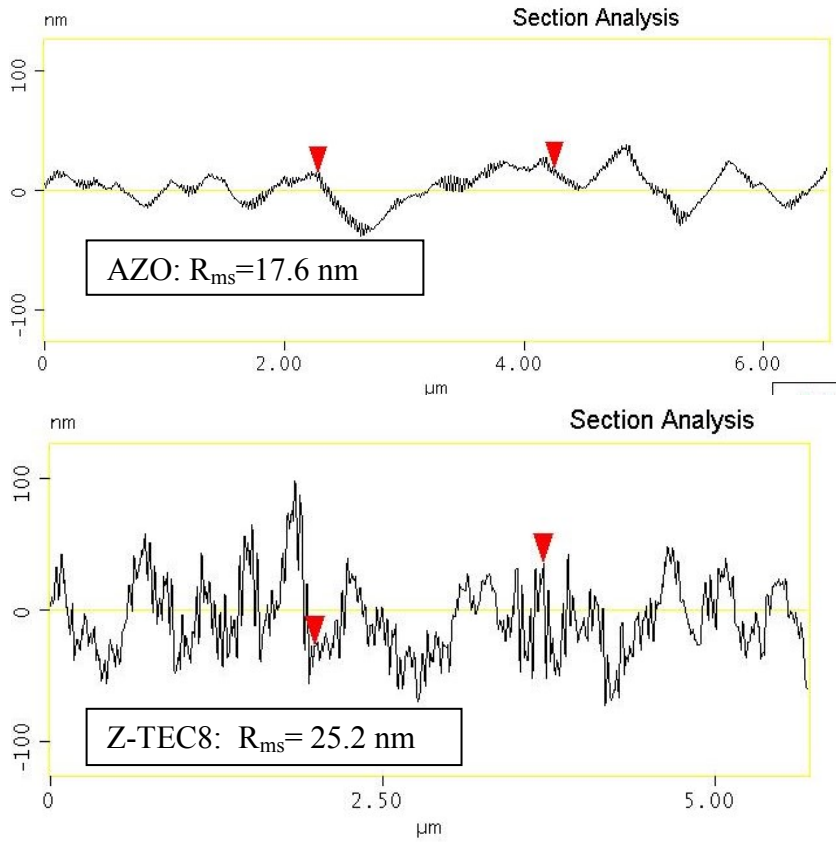


Figure 5-17 AFM line scan profile of AZO and Z-TEC8

One of the possible reasons for difference in structural defects might be from the different Si growth at trenches. Z-TEC8 substrate shows higher aspect ratio and narrow trench compared with AZO. The incident angle of Si radicals from peak to valley has relatively large variation on V shape Z-TEC8, compared with relatively smoother U shape AZO. The upper peak surface has higher localized growth rate than the bottom valley. During the deposition the upper surface film grows faster to meet the film nearby before the bottom is filled, leaving voids inside bulk. Meanwhile, V shape profile increase the possibility of crystal column collision during nc-Si:H growth, which results in the crack formation and smaller grain size [58].

Table 5-7 for shows JV performance of nc-Si:H solar cell on different substrate with $\sim 0.9\mu\text{m}$ i layer deposited by VHF 250W at 3 Torr with $\text{SiH}_4/\text{Si}_2\text{H}_6/\text{H}_2=7.7/0.8/300$ (3.9A/s , $X_c=63\%$) . The solar cell grown on Z-TEC8 has higher $J_{sc}=14.7\text{ mA/cm}^2$ compared with the one on AZO with $J_{sc}=12.2\text{ mA/cm}^2$. QE measurement is carried out to understand the collection performance at different wavelength, presented in Figure 5-18.

Table 5-7 JV performance of nc-Si:H p-i-n solar cell with Al back contact on different substrates

Substrate	V_{oc} (V)	J_{sc} (mA/cm^2)	FF (%)	E_{ff} (%)
Z-TEC8	0.392	14.7	60.6	3.5
AZO	0.452	12.2	69	3.8

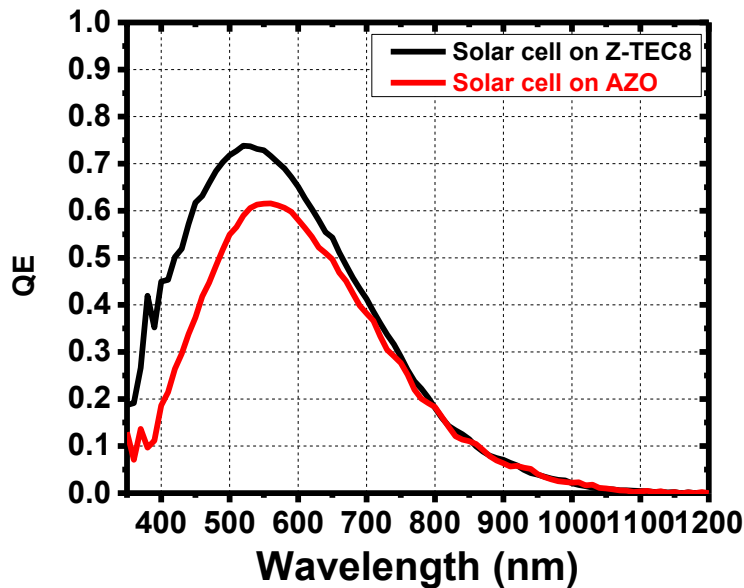


Figure 5-18 QE of nc-Si:H solar cells on Z-TEC8 and AZO

The major difference in QE on Z-TEC8 and AZO occurs at short wavelengths. This means it is not due to difference in scattering or optical enhancement related to

the different texture morphology. The QE at 400nm is about 40% on Z-TEC8 substrate compared with 20% on AZO. The lower short wavelength collection with AZO might result from the more front reflection due to less textured compared with Z-TEC8. The QE at 800nm is relatively low for both substrates, only about 20%, which may result from the poor optical properties of Al back reflector.

5.5.2 nc-Si:H solar cell with different back reflector contact

Table 5-8 lists the JV performance of nc-Si:H solar cells deposited in the same process run, hence same conditions, on AZO with Al and ITO/Ag back reflector contact. Using ITO/Ag as back reflector significantly increases the J_{sc} of the solar cell, which result from improvement of light trapping of longer wavelength light, as show in Figure 5-19. Figure 5-20 presents JV curve of nc-Si:H solar cell fabricated on AZO with ITO/Ag .

Table 5-8 JV comparison of nc-Si:H solar cells with different Back Contact

Substrate	Back Contact	Voc (V)	Jsc (mA/cm²)	FF (%)	Eff (%)
AZO	Al	0.452	12.2	69	3.8
AZO	ITO/Ag	0.44	15.2	67.1	4.5

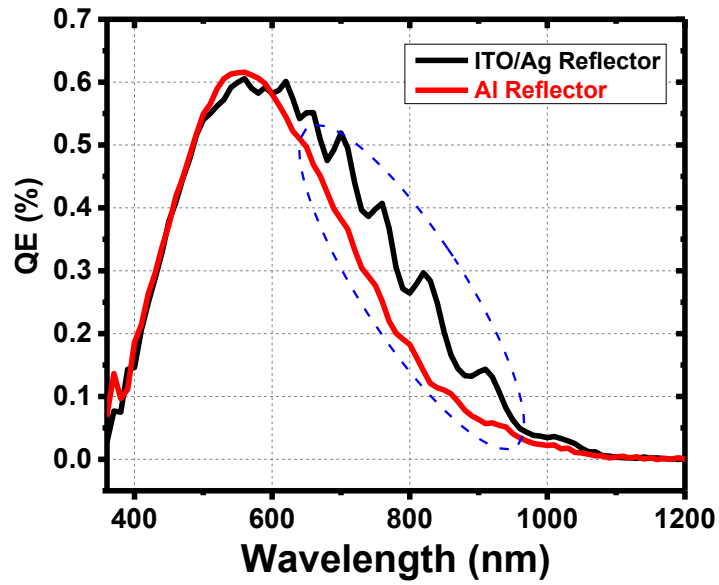


Figure 5-19 QE Comparison of the nc-Si:H solar cell fabricated on AZO with Al Back Reflector and ITO/Ag Reflector

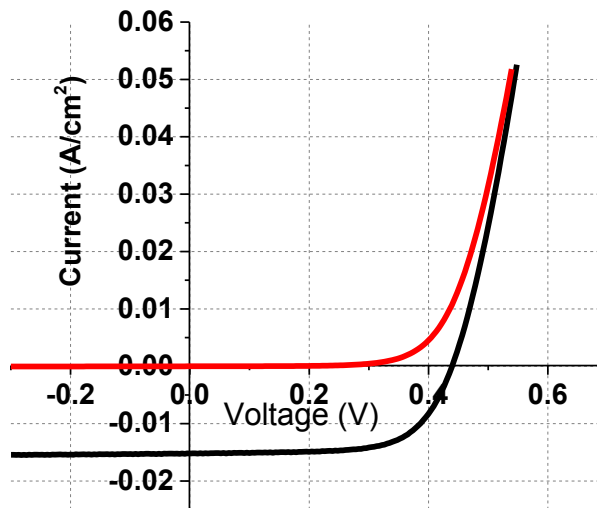


Figure 5-20 JV curve of nc-Si:H solar cell on AZO with ITO/Ag back reflector

5.6 Summary

In the chapter, the exploration of nc-Si:H deposition conditions and correlation with structural characterization have been discussed. Compared with a-Si:H, the nc-Si:H is deposited with H_2/SiH_4 at higher power and larger H_2 dilution region.

Increasing the H_2/SiH_4 ratio or increasing RF power results in higher crystalline volume fraction of nc-Si:H films. The grain size and growth orientation are very sensitive to the process conditions. It has been observed that large grain size is not necessarily implied by high X_c . There is no XRD peak detected for the nc-Si:H films deposited by RF plasma at low pressure despite their having $X_c > 50\%$. The grain size of nc-Si:H increases at higher deposition pressure. The preferential growth orientation with RF plasma depends on H_2/SiH_4 ratio. The nc-Si:H growth orientation could be tuned from (111) to (220) by increasing SiH_4 flow. Compared to RF, nc-Si:H films deposited by VHF require lower power and H_2 dilution to get similar X_c which is beneficial for high growth rate. Larger grain size could be obtained by VHF at lower pressure and the H_2/SiH_4 has negligible impact on growth orientation. In nc-Si:H deposition region, there is no significant growth rate increase with Si_2H_6 additive beyond that expected from having more Si atoms inside plasma, in direct contrast to the large growth rate enhancement observed with Si_2H_6 additive in a-Si:H deposition region. VHF plasma enhanced the growth rate much more than the additive.

nc-Si:H solar cell performance strongly depends on the surface geometry of the substrate. The solar cell fabricated on U shape Al doped ZnO has higher V_{oc} and FF than the one on V shape TEC8. Rough surface may result in structure defects such as

cracks or voids, hence worse i layer bulk quality. The short current of nc-Si:H solar cell increased significantly by using ITO/Ag, which has better light trapping performance compared with Al.

Chapter 6

INSIGHT OF SILICON FILM DEPOSITION BY PLASMA DIAGNOSTICS

6.1 Introduction

High quality a-Si:H and nc-Si:H thin films by PECVD have applications in various fields such as large area and low cost solar cells and thin film transistors. As discussed in the previous two chapters, however, a-Si:H and nc-Si:H electrical and structural properties are highly sensitive to process conditions of SiH₄/H₂ discharge. In order to understand the relationship of the process conditions and film properties in the 'chamber black box' several plasma characterization technologies have been currently used, including Mass Spectroscopy, Optical Emission Spectroscopy (OES) and Langmuir Probe [27].

OES is noninvasive diagnostic tool used to identify the radiative species such as Si*, SiH* and H* inside plasma where the intensity of the optical signal for each species is related to the excitation rates and species concentrations [59]. Langmuir Probe, on the other hand, is a simple and powerful tool to analyze the electric properties of plasma such as Electron density, plasma potential and Electron Energy Distribution (EEDF) [60], which are calculated from voltage-current measurement. The electron energy and density determines the dissociation pathway and reaction rates as well as the species concentration. As mentioned, the species from gas phase

plasma dissociation is important for film deposition. Thus the characterization of plasma discharge correlating with the film properties becomes critical to understand silicon thin film deposition by PECVD.

This chapter focuses on the $\text{SiH}_4/\text{Si}_2\text{H}_6/\text{H}_2$ plasma characterization and understanding the relationship between the plasma parameter and material properties. In order to correlate the material properties with the plasma parameters, the plasma is characterized during the film growth. OES is used to correlate Si and H species with the growth rate, microstructure factor, crystalline volume fraction of a-Si:H and nc-Si:H films. To characterize the plasma properties, a Langmuir Probe was installed in the deposition system. However, it is difficult to use Langmuir Probe in silane plasma due to the resistive coating on metal probe surface, which results in additional resistance loss into the probe circuit. The plasma properties during growth of nc-Si:H were evaluated since it has higher signal and shorter acquisition time compared with a-Si:H deposition region. The growth mechanism of a-Si:H and nc-Si:H are related to the plasma properties and are discussed in this chapter.

6.2 Experiment

Figure 6-1 shows the experimental apparatus for the OES and Langmuir Probe measurement used for plasma characterization of a-Si:H and nc-Si:H deposition using PECVD in either capacitively coupled 13.56 MHz (RF) or 40.68 MHz (VHF) plasma excitation. SiH_4 , Si_2H_6 , H_2 are delivered into the reactor through a gas shower head

with electrode area of $\sim 1100\text{cm}^2$ and 1.4 cm gap between the powered electrode and grounded substrate.

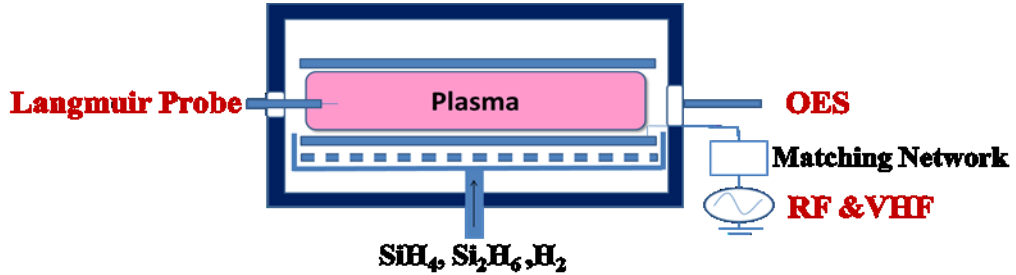
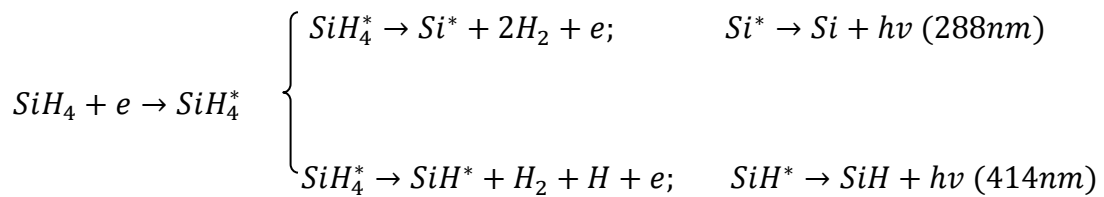


Figure 6-1 Experimental Apparatus of OES and Langmuir Probe

Optical Emission Spectroscopy (OES) spectra are recorded externally from the plasma emission through quartz window using optical fiber. The spectra collection system is located at the plasma close to substrate. The optical signal is guided through optical fiber into a spectrometer and the spectra are recorded.

Figure 6-2 shows a typical OES spectrum of SiH_4/H_2 plasma in a-Si:H deposition region. The emission lines of interest include $\text{Si}^*(288\text{nm})$, $\text{SiH}^*(414\text{nm})$, $\text{H}_\alpha(656\text{nm})$ and $\text{H}_\beta(486\text{nm})$ where the emission species results from the impact between electron and molecules and for Si^* and SiH^* the reactions are:



The H_α is a spectra line of the Balmer series from transition from $n=3$ to $n=2$, which results from excitation through electron and atomic H impact. Thus the SiH^* and H_α , H_β intensity is proportional to the Si and H species inside plasma. An estimation of

relative dissociation rates and concentration of the species can be made from spectra line intensity of OES measurement.

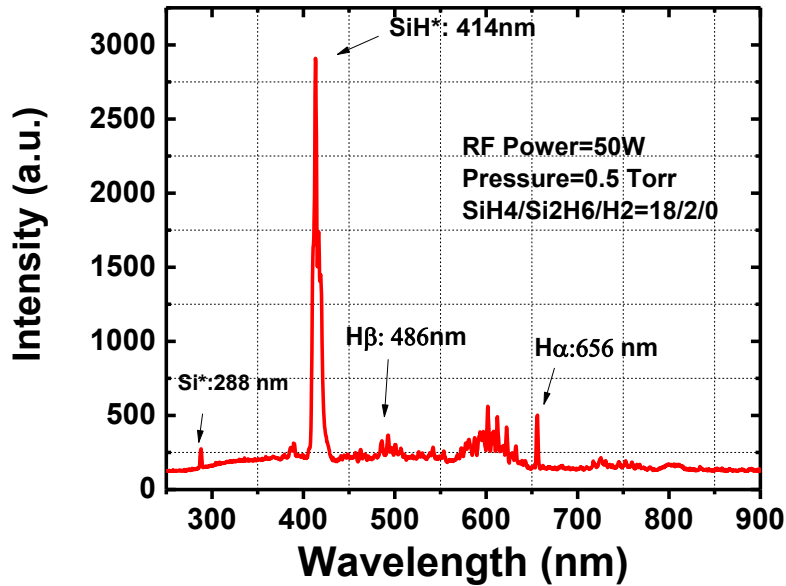


Figure 6-2 OES of SiH_4/H_2 plasma for a typical a-Si:H deposition condition

A Langmuir Probe system as discussed in Chapter 2 was used, where a Tungsten Wire with a 0.15mm diameter and 10 mm length was inserted into plasma to measure current with fast voltage sweep from -50V to +50V. To improve the probe measurement repeatability, the probe was heated and cleaned by high electron current with 70V bias in Ar plasma. The J-V curve from the Langmuir Probe was analyzed by Hiden Espssoft software. Sheath potential was obtained by subtraction of plasma potential (V_p) from the floating potential (V_f). The electron energy distribution function (EEDF), $f(E)$, was obtained from the Druyvesteyn expression, as mentioned

with Equation 2-9 in Chapter 2. Electron density (n_e) and mean electron energy ($\langle E_e \rangle$) were calculated from $f(E)$ by Equation 2-10 and 2-11 in Chapter 2

6.3 Plasma Characterization in a-Si:H Deposition Regime by OES

The a-Si:H materials properties discussed in Chapter 4 are related to the OES plasma characterization of SiH₄/H₂ discharge with and without Si₂H₆ additive for the a-Si:H deposition.

Figure 6-3 presents the OES spectra of a-Si:H deposition baseline plasma at 0.5 Torr, 30W with SiH₄ flow at 20 sccm without H₂ dilution, compared with 10% Si₂H₆ additive condition. As shown in the figure, the dominant peak at 414 nm indicates the main radiative species of SiH*. The weak H_α peak at 656 nm presents the relatively low concentration of atomic H inside plasma. By adding 10% Si₂H₆, there is no significant new peak observed, which indicates the similar radiative species produced by SiH₄ or Si₂H₆ discharge.

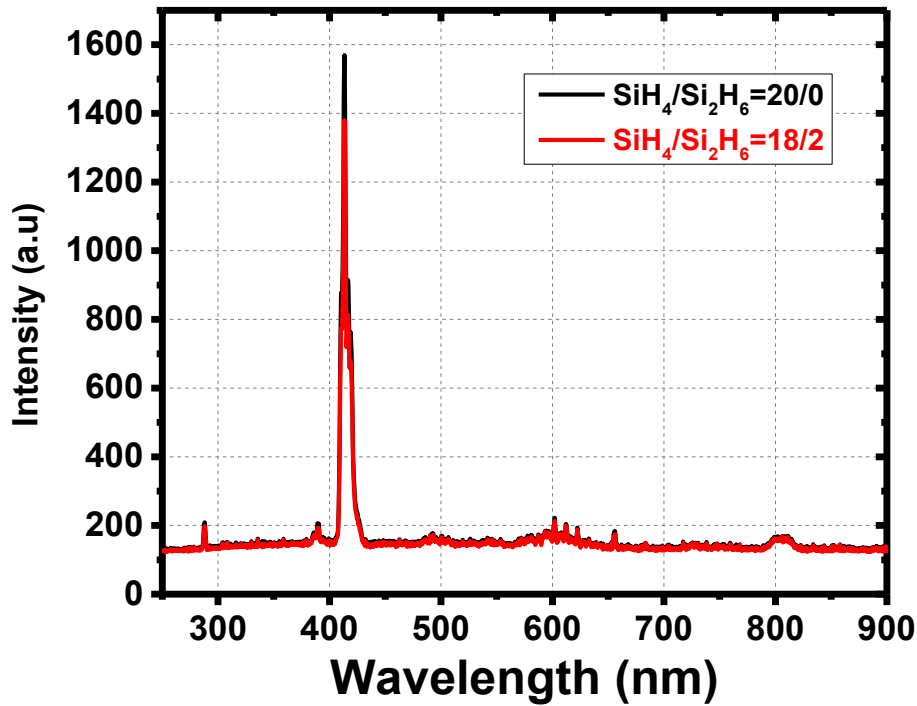


Figure 6-3 OES Spectra of a-Si:H deposition plasma at 0.5 Torr, 30W without H₂ dilution comparing pure SiH₄ and 10% Si₂H₆ in SiH₄

6.3.1 Relationship between SiH* and a-Si:H Growth Rate

Figure 6-4 presents the relationship between normalized SiH* intensity vs a-Si:H film growth rate with and without Si₂H₆ additive. The OES was measured for the plasma condition listed in Table 4-1 in Chapter 4: at 0.5 Torr, the plasma is discharged with SiH₄/Si₂H₆ only, while at 1.25 Torr, the plasma is measured with H₂ dilution R5: H₂/(SiH₄+Si₂H₆)=50/10. Different SiH* intensity was measured for the condition with increasing RF power.

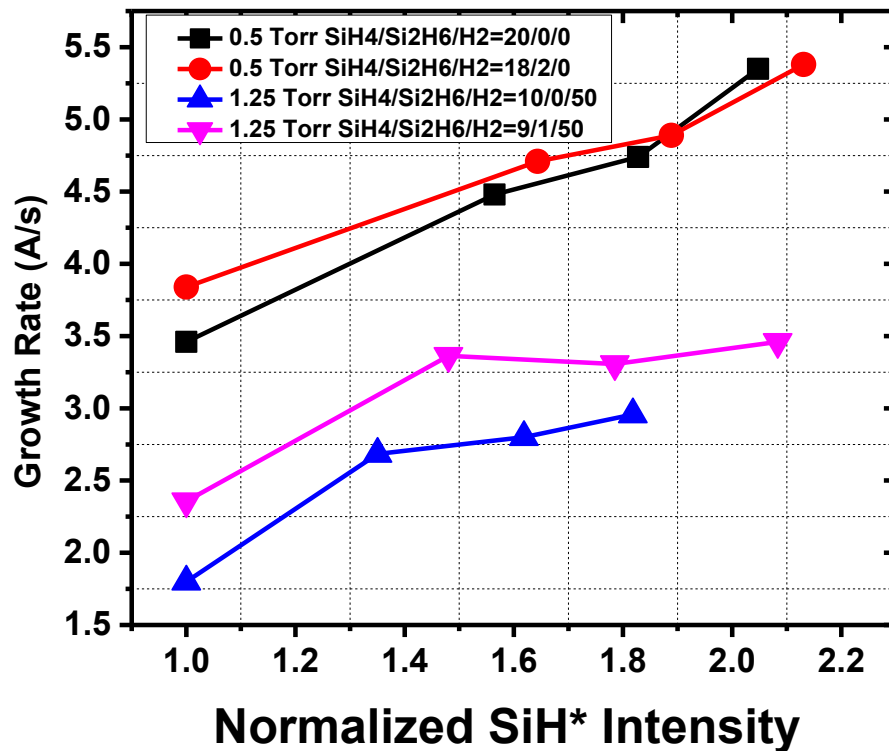


Figure 6-4 Growth Rate vs. SiH* intensity normalized to the lowest SiH* intensity for each series

For the gas mixture without H₂ dilution, the growth rate increases almost linearly with SiH* intensity. The SiH* intensity is determined by the amount of electron and SiH₄ impact dissociation and excitation reaction. Higher SiH* indicates higher dissociation percentage of SiH₄, which increases concentration of SiH₃ and SiH₂ the primary species for a-Si:H film growth. Thus, the growth rate shows linear relationship with OES SiH* intensity when a-Si:H is deposited by the gas mixture without H₂ dilution.

However, for the case of H₂ dilution, higher SiH* by increasing RF power doesn't lead to a higher growth rate which suggest that the growth rate is not solely dependent on Si species density for H₂ diluted plasma.

6.3.2 OES Analysis: Effect of RF Power for a-Si:H deposition and film properties

As discussed in Chapter 4, the growth rate and film structure are highly dependent on the RF Power and we speculate that the observed decrease in R_{mf} with increasing power is due to the role of atomic hydrogen (H) on film growth mechanism. It has been reported that high concentrations of H at the film surface are expected to reduce the growth rate and decrease R_{mf} by structural relaxation [61, 62]. Further OES analysis is carried out to understand the effect of RF Power on the role of H for a-Si:H deposition.

Figure 6-5 presents H_α and SiH* intensity at 1.25 Torr discharge as a function of RF power with and without Si₂H₆ additive. Both H_α and SiH* intensity increase at higher RF power, indicating more H₂ and SiH₄ dissociation at higher power resulting in higher H and Si species concentration inside the plasma. It has been shown in Figure 4-3 that a-Si:H growth rate saturates at higher power with H₂ dilution. It would be possible that the saturation of growth rate at higher power is due to SiH₄ depletion. However, the higher SiH* suggests the growth rate saturation at higher power is not limited by the SiH₄ flow. On the other hand from the OES signals, the H_α signal increases more rapidly than SiH* intensity with increase of power and hence H

concentration at the growth surface is relatively larger at higher power. Thus in high RF power growth region, there is more atomic H diffuse to the film growing surface. The atomic H preferentially reacts with the SiH_n group which weakly bonded to surface, forming gas phase SiH₄, Si₂H₆ or H₂ followed by a desorption from the deposition surface. In other words, the atomic H plays a role to preferentially etch weak and strained bonds. Thus the relatively more H flux to the substrate surface at high power region can explain saturation of growth rate as observed in Figure 4-3 and the monotonic decrease in R_{mf} shown in Figure 4-5 as the RF power is increased.

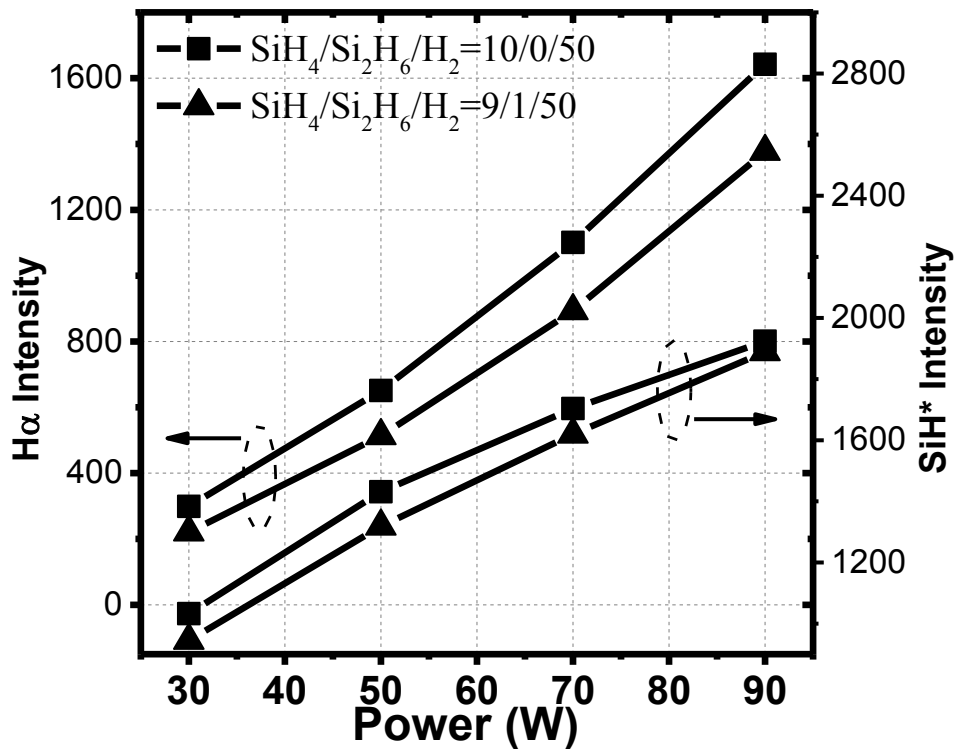


Figure 6-5 OES H α emission intensity at 656 nm and SiH* emission intensity at 414 nm as a function of RF power at 1.25 Torr

6.3.3 OES Analysis: Effect of Si₂H₆ Additive

Figure 6-6 shows OES value at 414 nm due to SiH* at different power with different fraction of Si₂H₆ additive at 1.25 Torr with H₂ dilution. The SiH* intensity increases with RF power for each SiH₄/Si₂H₆/H₂ mixture. At each RF power, the SiH* intensity decrease as Si₂H₆ fraction increase.

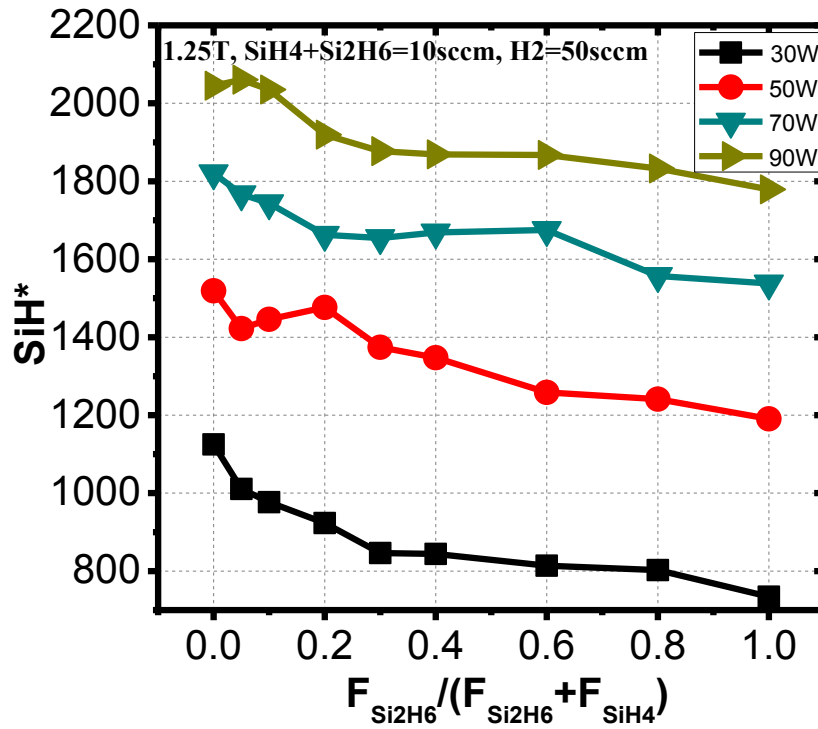


Figure 6-6 SiH* emission intensity at 414 nm as a function of Si₂H₆ fraction and RF power

Compared with SiH₃ which is major growth species from SiH₄ dissociated by electron threshold energy ~8.7eV, the Radiative species SiH* is formed by the relatively higher energy impact between electron (>10.3eV) and SiH₄. The reduction

in SiH* intensity by adding Si₂H₆ may indicate the reduction of high energy electron impact, in other words, probably lower electron temperature.

As shown in Figure 6-4, for the same SiH* intensity, the Si₂H₆ additive films have higher growth rate than without Si₂H₆ in gas phase. The ionization threshold energy of Si₂H₆ is ~10.5 eV which is lower than SiH₄ at 13.7eV. Figure 6-7 presents the Ionization Cross Section Comparison for SiH₄ and Si₂H₆ [63]with a typical EEDF curve for eye guide. The shallow area indicates the energy range of electrons which contribute to ionization. Si₂H₆ has lower ionization threshold energy and larger cross section compared with Si₂H₆. By adding Si₂H₆ into gas mixture, more electrons are produced by ionization of Si₂H₆ which benefits from the lower ionization threshold energy. The higher electron density enhances the SiH₄ dissociation leading to higher growth rate. However, the high energy electron concentration was also reduced due to the Si₂H₆ ionization collisions, resulting lower SiH* intensity. Thus, the discharge with Si₂H₆ additive has lower SiH* intensity but higher growth rate.

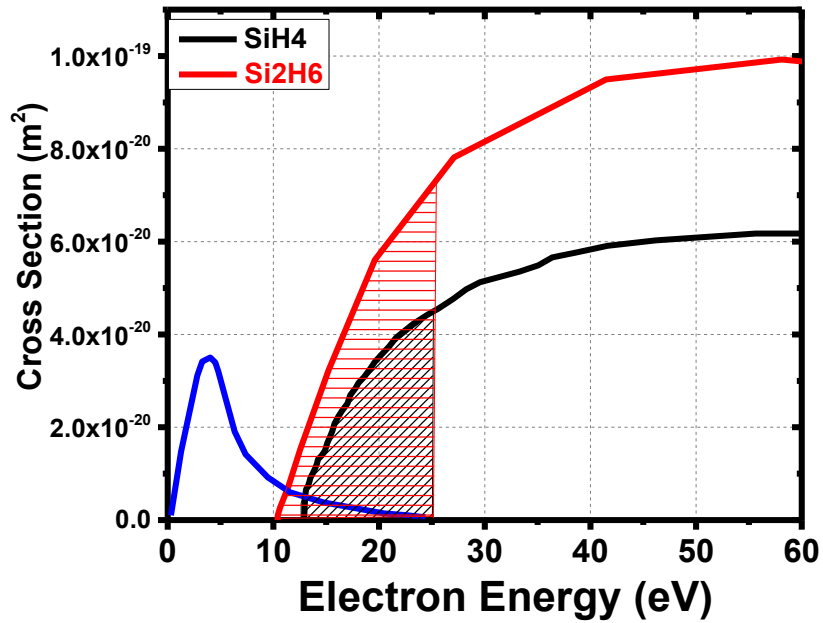


Figure 6-7 Ionization Cross Section Comparison of SiH₄ and Si₂H₆, with EEDF curve in blue for eye guide

6.3.4 OES Analysis: Effect of H₂ dilution for a-Si:H deposition

Figure 6-8 shows H α /SiH* intensity of SiH₄/ Si₂H₆ discharge with and without H₂ dilution as a function of RF power. The OES of without H₂ dilution is measured under 0.5 Torr with RF power 20W to 70W, while the series of H₂ dilution is processed at 1.25 Torr with H₂/SiH₄+Si₂H₆=5 with RF power 30W to 120W.

Both with and without H₂ dilution conditions, H α /SiH* increases at higher RF power. Thus H concentration at growth surface is larger at higher power which explains the lower R_{mf} with higher power as shown in Figure 4-5. With H₂ dilution, a higher H α /SiH* signal ratio is observed by OES measurements, which correlates with the materials properties that the a-Si:H film deposited with H₂ dilution has relatively

lower R_{mf} compared with $\text{SiH}_4/\text{Si}_2\text{H}_6$ discharge only. By adding 10% Si_2H_6 additive to the gas mixture with or without H_2 dilution, the $\text{H}\alpha/\text{SiH}^*$ ratio decreases which may lead to the higher R_{mf} of the film as discussed in Chapter 4.

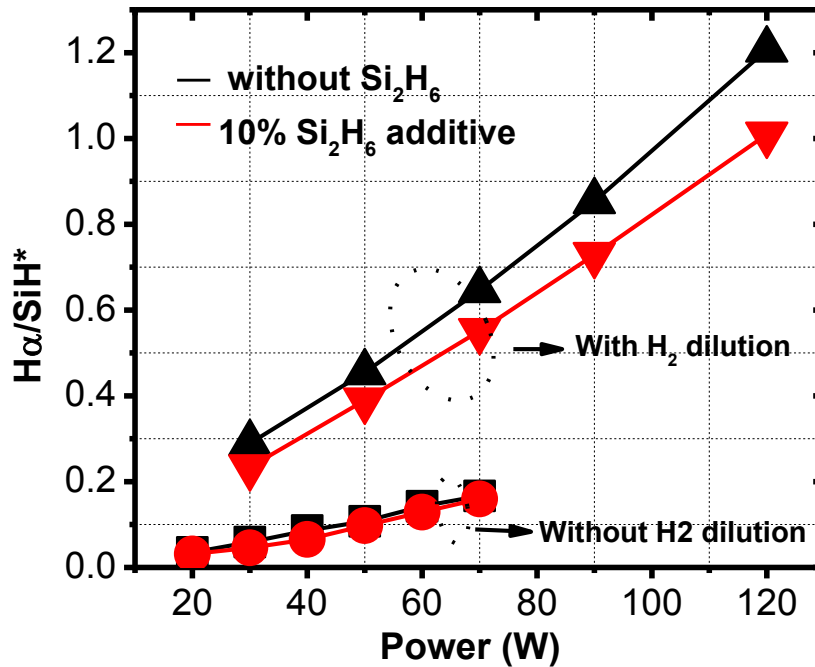


Figure 6-8 Ratio of $\text{H}\alpha/\text{SiH}^*$ as a function of RF power with and without H_2 dilution

6.4 Plasma Characterization in nc-Si:H Deposition by OES

Compared with a-Si:H deposition, nc-Si:H is deposited under relatively high power and high H_2 dilution discharge region. Figure 6-9 presents the normalized OES spectra of SiH_4/H_2 discharge in typical a-Si:H deposition regime and nc-Si:H regime with $X_c=60\%$.

The dominant OES peak for discharge in nc-Si:H region is H α (656nm) which results from the excitation of atomic H inside plasma. Thus, it is very different than the discharge in a-Si:H region where the majority species detected by OES is SiH* from the excitation of silane species. The OES measurement indicates that the atomic H concentration in nc-Si:H deposition plasma is higher compared with a-Si:H regime, consistent with high H₂ dilution requirement for nc-Si:H deposition.

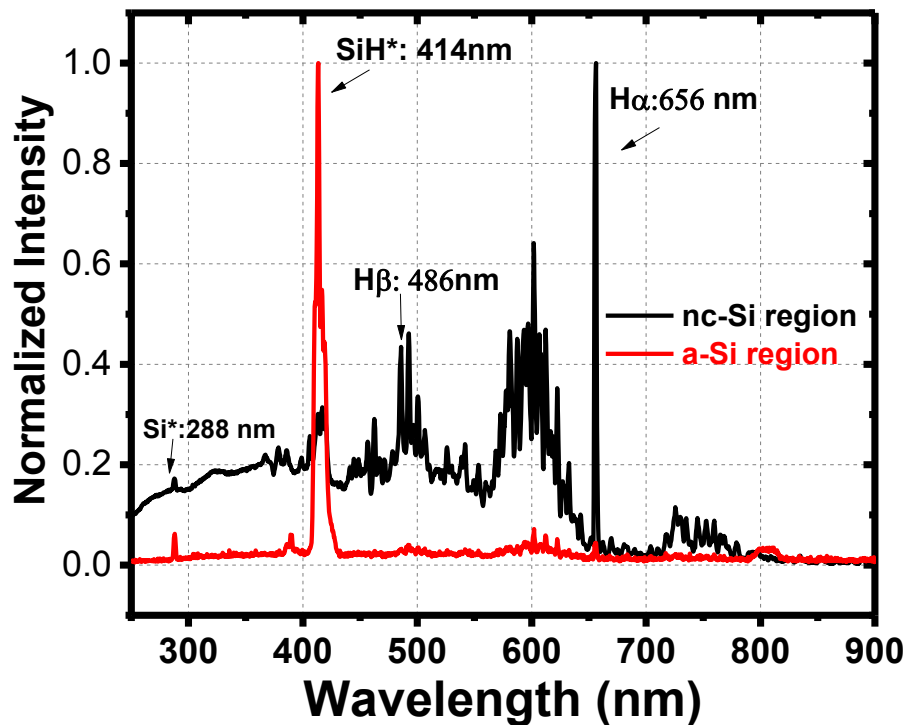


Figure 6-9 Normalized OES Spectra of a-Si:H and nc-Si:H deposition plasma

6.4.1 Effect of SiH₄ Flow and Partial Pressure

Figure 6-10 presents the intensity of SiH* and H α as function of SiH₄ flow rate for a constant H₂ flow rate of 450 sccm where the H₂/SiH₄ ratio varied from 32 to 65 at 3Torr with RF power 250W. Note, the partial pressure, or concentration of the SiH₄ increases with higher SiH₄ flow. The OES SiH* intensity increases linearly with SiH₄ flow, which is consistent with the OES SiH* intensity given by:

$$I_{SiH^*} \propto n_e * [SiH_4] \tag{6-1}$$

The H α intensity is almost constant since the change of H₂ concentration inside plasma is negligible with small amount SiH₄ variation.

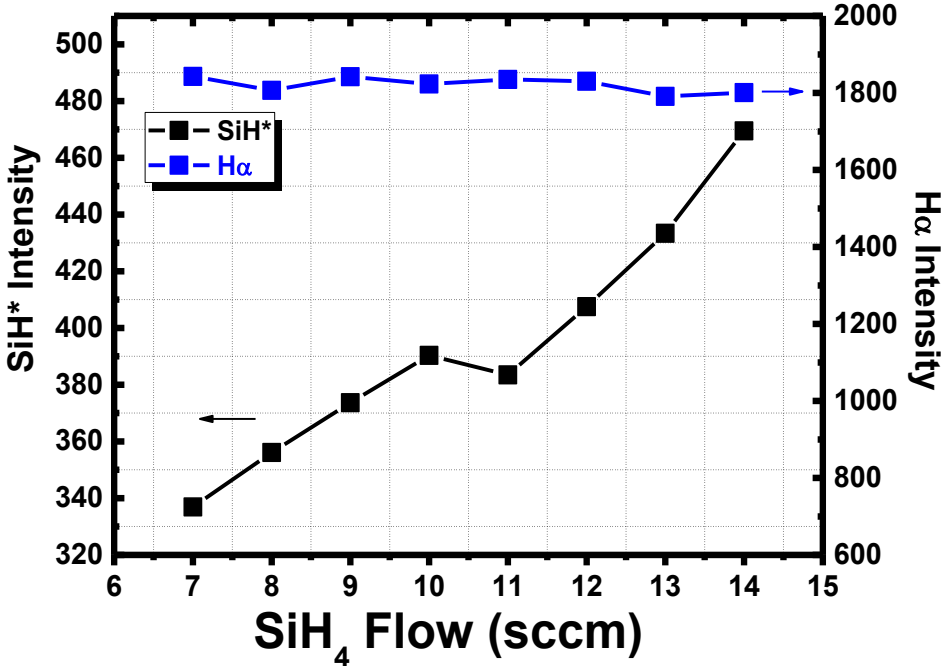


Figure 6-10 OES SiH* and H α as a function of SiH₄ flow with H₂ 450 sccm at 3 Torr with RF power 250W

6.4.2 SiH* and nc-Si:H growth Rate

In this section, nc-Si:H thin films were grown using by: 1) RF plasma at 3 Torr, with power of 250W at constant H₂ flow of 450 sccm where the SiH₄ flow rate was varied from 7 sccm to 14 sccm; and 2) VHF plasma at 3 Torr with power of 250W at constant H₂ flow of 300 sccm where the SiH₄ flow rate was varied from 8.5 sccm to 25 sccm. The OES SiH* and H α emission intensities were collected simultaneously to correlate with the growth rate.

Figure 6-11 presents the variation of the film growth rate with SiH* intensity in RF and VHF plasma, respectively. It is observed that the growth rate of nc-Si:H film strongly correlates with the OES SiH* intensity in both RF and VHF plasma. The SiH* intensity is proportional to the dissociation rate of SiH₄, thus the relationship between SiH* and growth rate can be expected.

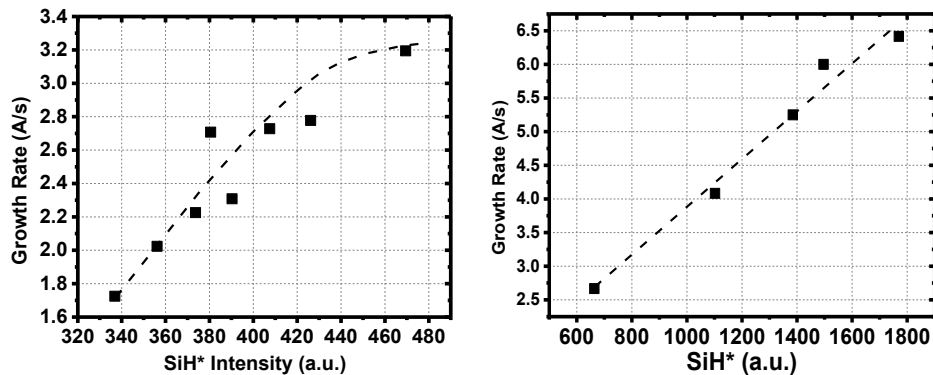


Figure 6-11 OES SiH* and Growth Rate by RF (left) and VHF (right)

6.4.3 $H\alpha/SiH^*$ and Raman X_c

As discussed in Chapter 5, the crystalline volume fraction is highly dependent on the H_2 dilution for the growth of nc-Si:H films and in this section, the ratio of OES $H\alpha$ and SiH^* signal are used to evaluate the H and Si species inside plasma.

Figure 6-12 presents the ratio of $H\alpha/SiH^*$ and the Raman Crystalline Volume Fraction X_c of the films deposited by RF and VHF, respectively. Higher $H\alpha/SiH^*$ indicates relatively high atomic H concentration inside plasma compared with silane species which diffuse to growth surface results in the film deposition with higher Raman X_c . Additionally, there is a threshold value of $H\alpha/SiH^*$ for RF plasma to grow nc-Si:H films is higher than VHF.

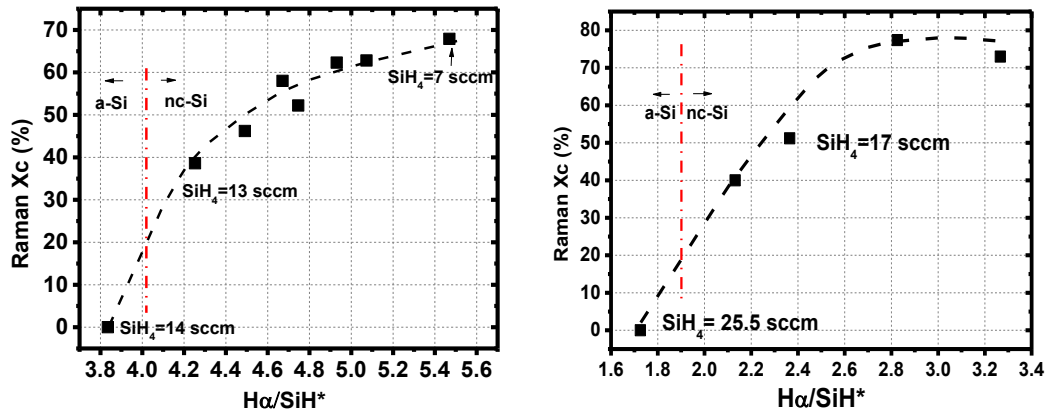


Figure 6-12 OES $H\alpha/SiH^*$ and Raman X_c by RF(left) and VHF (right)

6.4.4 OES measurement at different Pressure

As discussed in Chapter 5, the deposition pressure has significant effect on the film properties, especially for nanocrystalline Si films, and in this section OES measurements are performed to characterize the plasma properties at different pressures. Figure 6-13 presents the SiH* and H α as a function of pressure from 2 Torr to 8 Torr where the SiH $_4$ and H $_2$ flow were fixed at 8.5 sccm and 300 sccm respectively with an RF power of 515W.

The SiH* and H α intensity decreases with increase of pressure which is counter-intuitive since the SiH $_4$ and H $_2$ concentration increases with higher pressure. At relatively high RF power of 515W, the ionization collision rate between the electron and both the SiH $_4$ and H $_2$ molecule is enhanced resulting higher electron density. However, due to the increasing number of collisions between electrons and different radicals, the Electron Energy Distribution shifts to lower energy. Thus the formation of SiH* and H* decreases as the electron cools to a energy lower than the threshold value needed to form the SiH* and H*. The results will be discussed further in next section based on Langmuir Probe measurement in next section where the change in Electron Energy Distribution is confirmed.

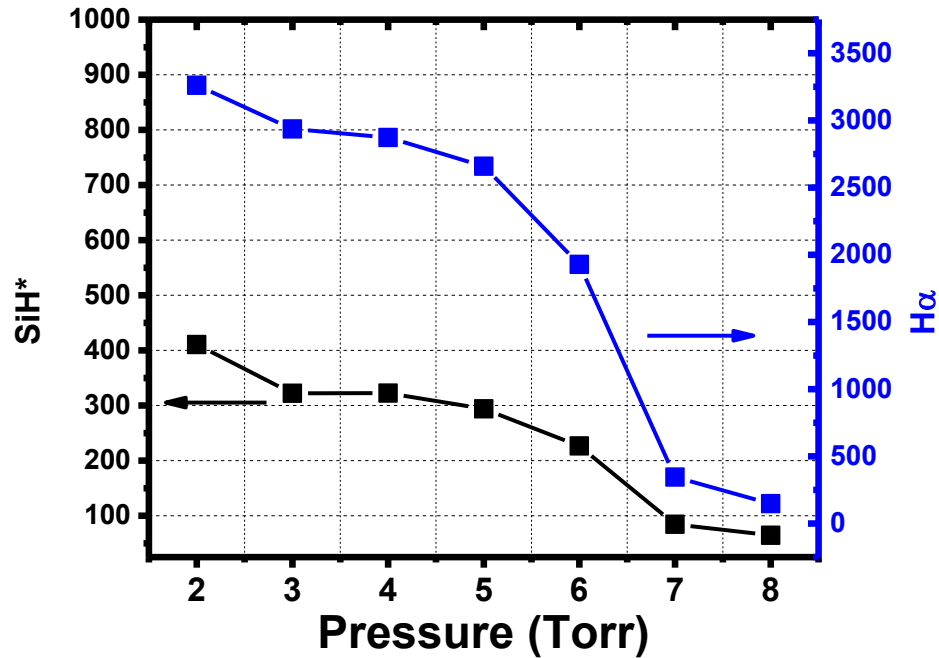


Figure 6-13 OES SiH* and H α intensity as a function of pressure with SiH₄/H₂=8.5/500, RF Power 515W

The results of SiH* and H α intensity as a function of pressure could not be simply interpreted by Equation 6-1. We believe that the SiH* and H α signal reduction at higher pressure is not due to the lower electron density but the electron energy distribution shifting to lower energy. SiH* and H α excitation result from the relatively high energy impact between electron and SiH₄ or H₂ molecule. At higher pressure, the more frequent collision reduces the electron energy, resulting lower concentration of the electron which has higher energy than SiH* and H α excitation threshold energy. The results from the Langmuir Probe measurement in next section would help to prove the theory mentioned above.

6.4.5 Effect of RF Power on SiH* and H α /SiH*

Figure 6-14 presents OES SiH* and H α /SiH* as a function of RF power with SiH₄/H₂=7/300 at 3 Torr for the growth of nc-Si:H films where the variation of SiH* and H α /SiH* as a function of power follows the similar trend as observed in a-Si:H region shown in Figure 5-5 and 5-7. Both SiH* intensity and H α /SiH* increases with power which is consistent with higher growth rate and X_c-observed with higher power for nc-Si:H materials properties. The higher H α /SiH* at higher power suggest H₂ dissociation rate is relatively faster at higher power, mostly due to the electron energy drift to higher values.

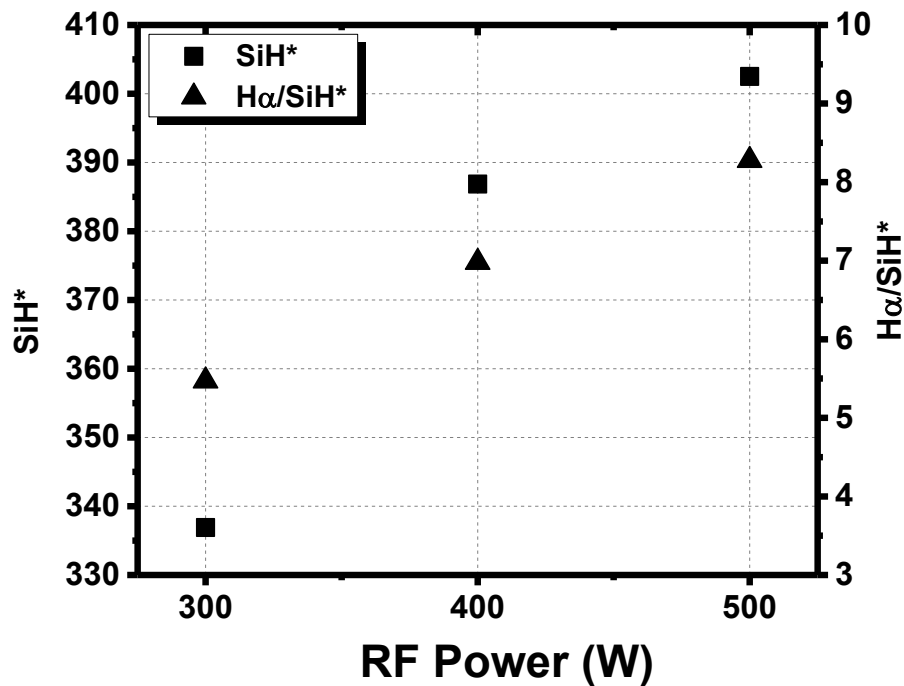


Figure 6-14 OES SiH* and H α /SiH* as a function of RF Power for nc-Si:H deposition SiH₄/H₂=7/300 at 3 Torr

6.5 Nc-Si:H Deposition Plasma Properties by Langmuir Probe Measurement

The growth of a-Si:H and nc-Si:H films depends of plasma discharge properties and in this section the electric properties of the plasma are characterized using a Langmuir Probe to evaluate the electron density and the energy distribution and the results are coupled with the optical properties of the plasma and the material properties of the film. The use of Langmuir Probe in a reactive plasma requires a short acquisition time as well as high signal to noise ratio, since the probe will degrade in the plasma during the measurement. The only reasonable and valid results were obtained in nc-Si:H deposition region.

6.5.1 EEDF at Different Pressure measured by Langmuir Probe

Langmuir Probe was used to characterize the RF Plasma in nc-Si:H growth region using a $H_2/SiH_4=8.5/300$ at RF Power 515W where the process pressure was varied from 2.5 Torr to 8 Torr. Figure 6-15, Figure 6-16 and Figure 6-17 show the EEDF, electron density and average electron energy at different pressure in plasma, respectively.

By increasing the pressure from 3 Torr to 5 Torr, the electron density is more than doubled from $1.4 \times 10^{15} \text{ m}^{-3}$ to $3.3 \times 10^{15} \text{ m}^{-3}$ where the higher electron density may result from increasing number of collision between the electron and molecule such that the ionization level is enhanced. As a result, the higher electron density results in the higher dissociation rate of SiH_4 which enhanced the growth rate. As shown in

Chapter 5 before, the nc-Si:H growth rate at 5 Torr is 4.1 A/s compared with 2.7 A/s at 3 Torr, which is consistent with the electron density variation at these pressures.

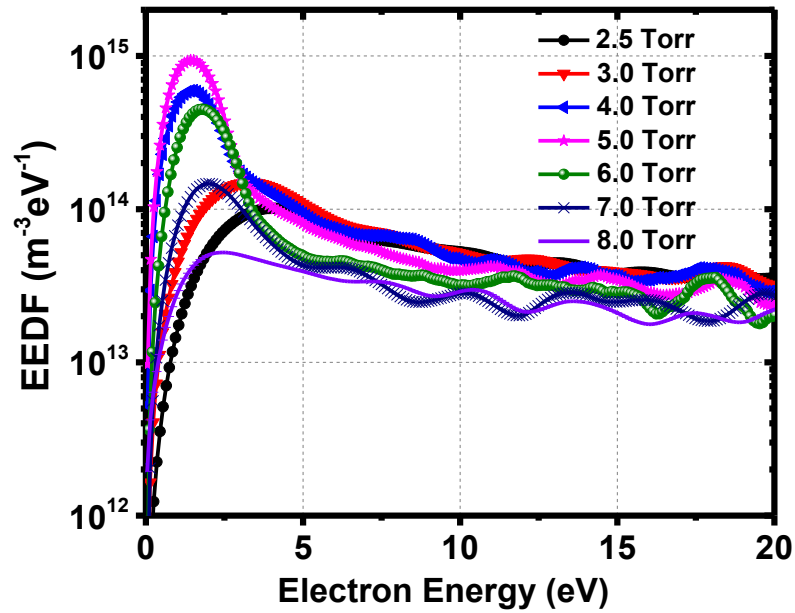


Figure 6-15 Langmuir Probe Results: EEDF at different pressure with RF Plasma

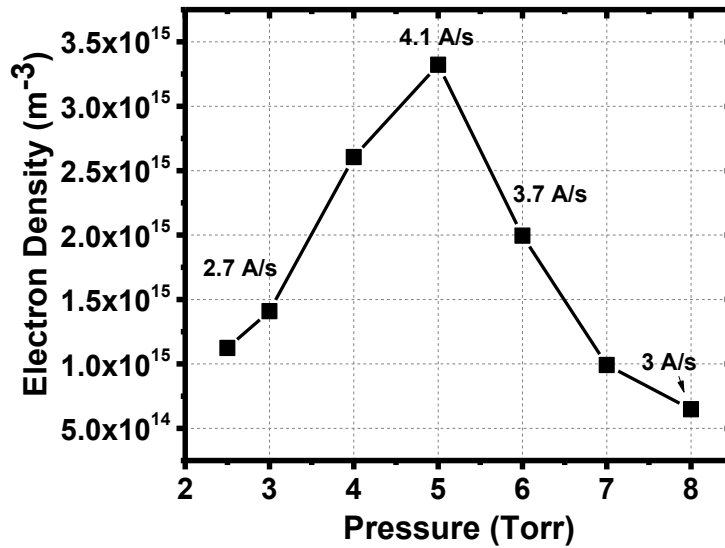


Figure 6-16 Langmuir Probe Results: Electron Density at different Pressure with RF Plasma

The EEDF curve indicates the lower energy electron dominates the electron population at high pressure up to 5 Torr which is due to more frequent collision between the electron with molecule and species, reducing the average electron energy. As the pressure is increased from 3 Torr to 5 Torr, the $\langle E_e \rangle$ is significantly reduced from 8.0 eV to 3.8 eV, primarily due to the energy loss during electron-molecule or radical impact interaction. Further increasing pressure results electron-radical attachment which eliminates the low energy free electrons inside plasma. Thus, the average electron energy measured by Langmuir Probe increases.

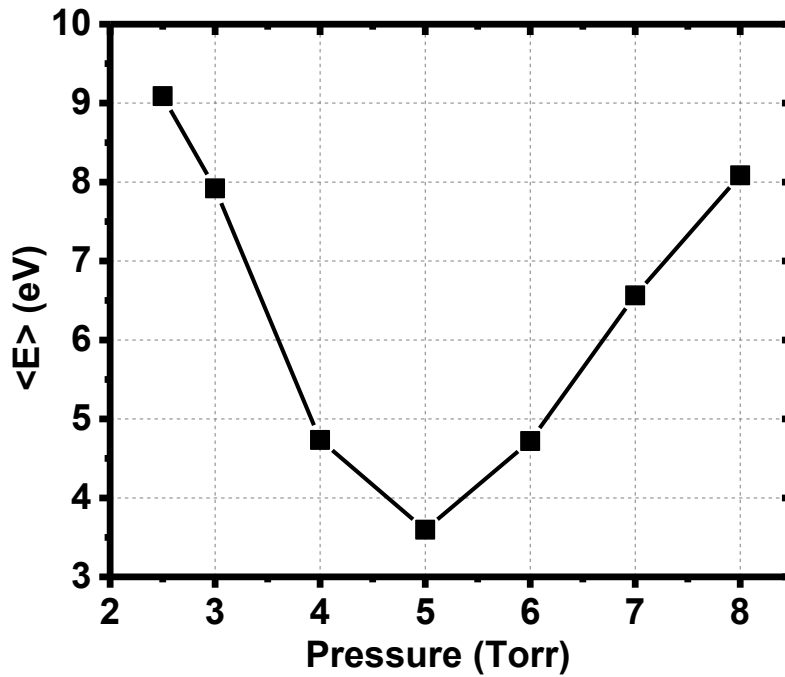


Figure 6-17 Langmuir Probe Results: Mean Electron Energy at different Pressure with RF Plasma

Further increasing the deposition pressure from 5 Torr to 8 Torr, the low energy electrons have much higher chance of attachment to the neutral particles so that the free electron density is decreased which reduces SiH_4 dissociation rate resulting in lower growth rate. The growth rate reduces from 4.1 A/s at 5 Torr to 3 A/s at 8 Torr.

6.5.2 Sheath Potential of the plasma and Effect on Grain Size

Figure 6-18 presents the sheath potential as a function of deposition pressure. The sheath potential decreases from 24 V at 3 Torr to 14 V at >5 Torr.

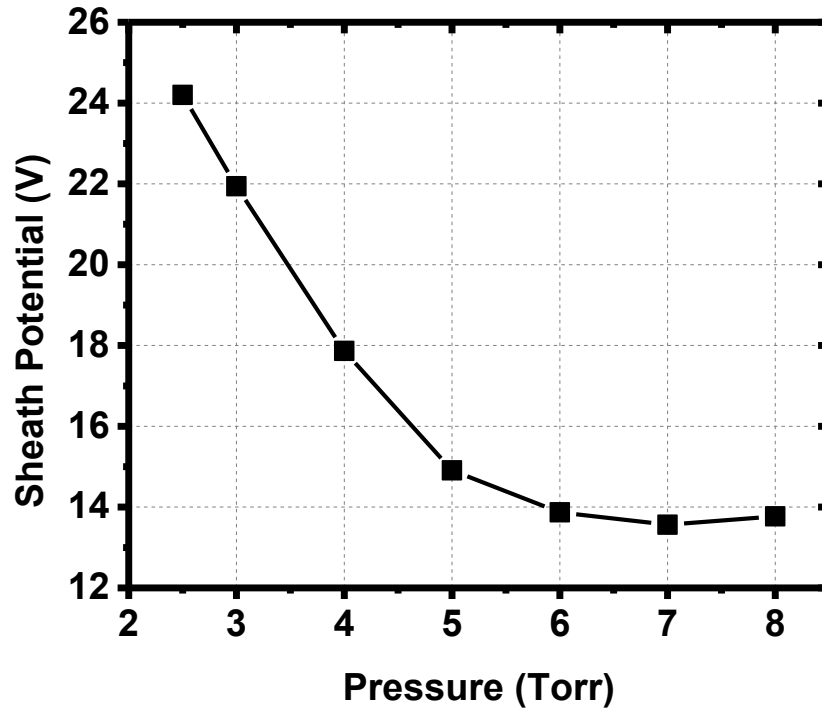


Figure 6-18 Langmuir Probe Results: Sheath Potential at different Pressure with RF Plasma

It has been reported that the ion energy is a more important parameter for nc-Si:H crystallinity rather than ion flux density and the nc-Si:H grain size could be reduced by the excess ion bombardment in the high power regime [21]. During the film deposition, the positive ions are accelerated by the sheath potential drifting from plasma region to substrate where the ion energy is primarily determined by the sheath potential between the substrate the plasma zone. Moreover, the lower electron density might indicate the lower ion density at 8 Torr. It has been presented in Chapter 4 that no XRD peaks was observed for nc-Si:H deposited at 3 Torr by RF while the grain size kept increasing with higher pressure 8 Torr. The larger grain size at higher

pressure by RF may result from the combination of low energy electron-molecule impact and less ion bombardment damage.

6.5.3 Interpretation of OES results at different pressure by Langmuir Probe Analysis

Higher deposition pressure up to 5 Torr results larger electron density as shown in Figure 6-16. However, both OES SiH* and H α intensity keep decreasing with deposition pressure increasing from 3 Torr to 8 Torr, as shown in Figure 6-13. The OES intensity decrease with higher electron density could be explained by high energy electron density analysis by Langmuir Probe.

As show in Figure 6-15, the deposition pressure significantly suppresses the electron energy distribution at high energy range. The density of the electrons with energy higher than the threshold of SiH* or H α excitation should be considered to interpret the OES intensity, rather than the entire electron density. Therefore, the lower SiH* and H α intensity could not be explained by Equation 6-1 since only the electrons with energy larger than the excitation threshold contributes to the OES SiH* or H α signal intensity.

The SiH* species result from the SiH₄ dissociative excitation with a threshold energy of 10.3 eV.

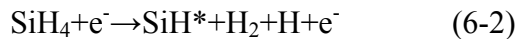


Figure 6-19 presents the comparison of entire electron density as well as electron density with energy above 10.3 eV, which are calculated from EEDF analyzed by

Langmuir Probe. Although the entire electron density increases from 3 Torr to 5 Torr, it's clear that the density of the electron with energy higher than the SiH* excitation threshold kept decreasing at higher pressure, resulting in lower OES SiH* intensity.

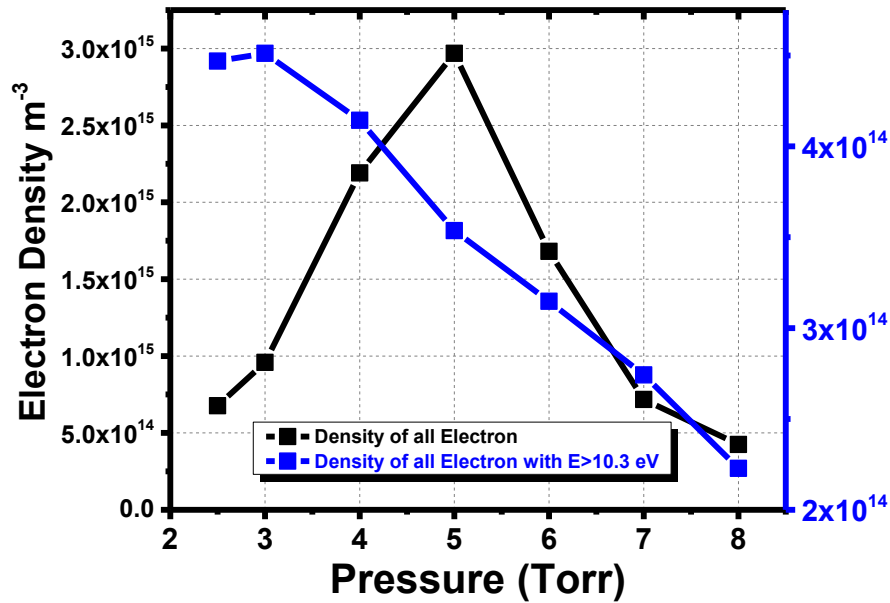
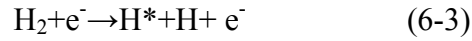


Figure 6-19 Electron Density, both total and that with energy larger than SiH* excitation threshold, as a function of Pressure

6.5.4 Effect of RF Power and EEDF inside Plasma

It has been observed that by increasing RF Power for either a-Si:H or nc-Si:H growth, the OES H α signal intensity increases faster than SiH* intensity resulting higher H α / SiH*. In Figure 6-20, the EEDF at SiH₄/H₂=8.5/300 at 3 Torr with different RF Power is shown. The H α species results from the electron and H₂

dissociative excitation which has a threshold energy at 16.6 eV, much larger than for the Si species.



By increasing RF power, the electron density at higher energy tail of the EEDF significantly increase, which leads to more H₂ dissociation and excitation. Thus higher power results larger H concentration inside plasma.

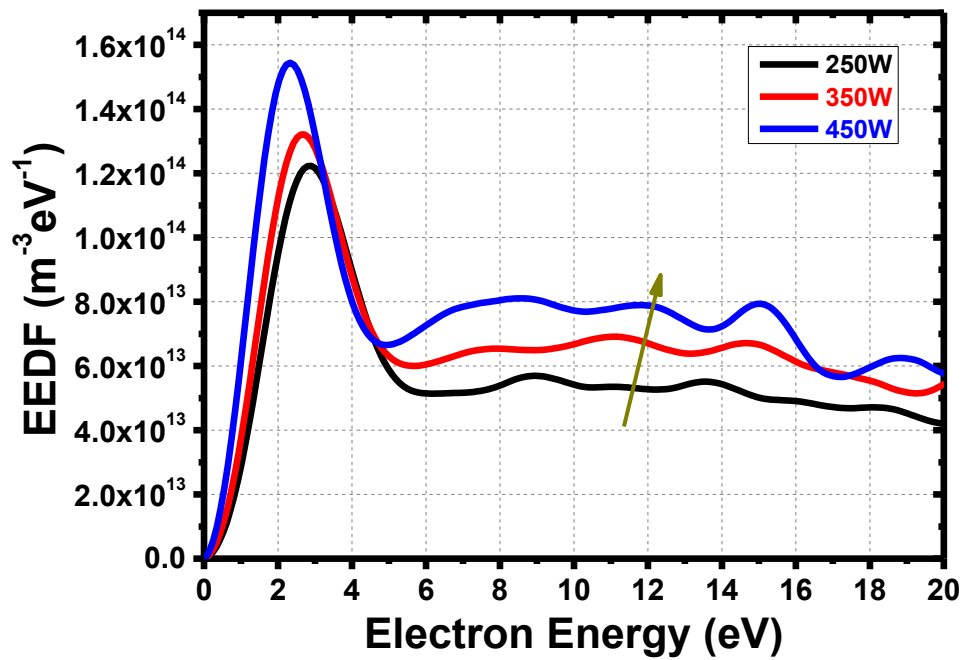


Figure 6-20 EEDF of RF plasma at different Power

6.5.5 Comparison of RF and VHF Plasma with Langmuir Probe Measurement

Figure 6-21 shows the EEDF for RF and VHF at 3 Torr, 250W. The $\langle E_e \rangle$ is 5.6 eV for VHF (large grain size~20nm) and 9.2 eV for RF (small grain size<2nm).

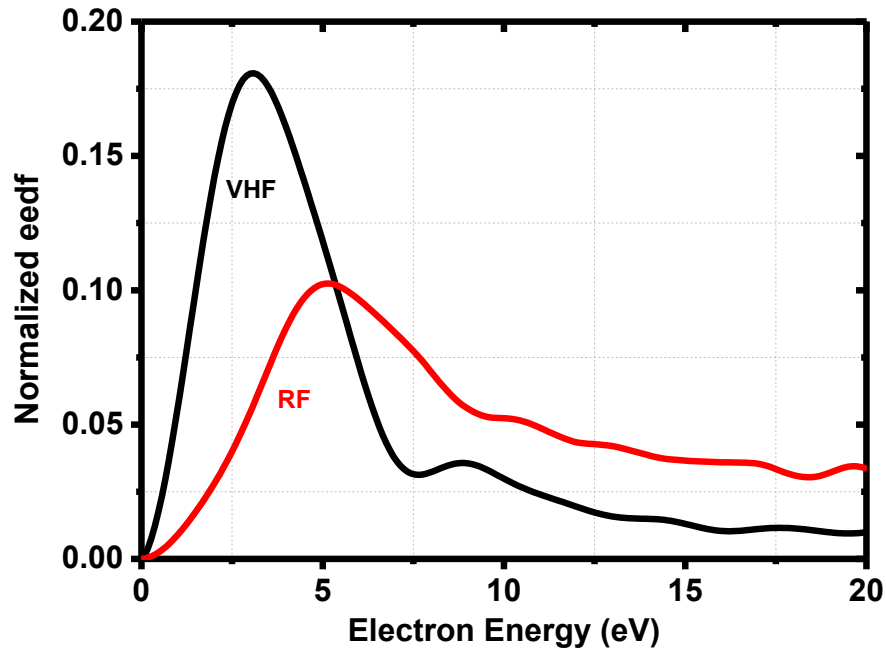


Figure 6-21 Normalized EEDF by RF and VHF Plasma, normalized to unity integrated area

6.6 Summary

In this chapter, the the properties of the plasma used to grow a-Si:H and nc-Si:H have been characterized by OES and Langmuir Probe and correlated with the film properties. It has been found that, the OES SiH* intensity is proportional to the growth rate if there is no significant change in EEDF. The reduction of SiH* intensity with Si₂H₆ additive indicates that there is less high energy impact between electron

and Si species by introducing Si_2H_6 . Deposition conditions leading to higher $\text{H}\alpha/\text{SiH}^*$ shows low R_{mf} for a-Si:H or higher Raman X_c for nc-Si:H films, respectively. Increasing deposition pressure significantly suppress the high energy electron, as well as the sheath potential of the plasma, which leads to less surface ion bombardment correlating with larger grain formation. Conditions of Si_2H_6 additive, higher pressure or higher plasma frequency all reduce the density of high energy electrons and shift the EEDF towards low energy, while high power increases the electron density uniformly in the entire range of energy spectra. Low energy plasma is conducive for large grain nc-Si:H films. Similarly, high power leads to severe ion bombardment to the film growing surface and reduction of grain size. The OES SiH^* and $\text{H}\alpha$ intensity could be interpreted by high energy electron density analyzed by Langmuir Probe.

Chapter 7

SUMMARY AND OUTLOOK

In this thesis, amorphous silicon (a-Si:H) and nanocrystalline silicon (nc-Si:H) thin films deposited by plasma enhanced chemical vapor deposition have been systematically studied to understand the correlation of their deposition conditions, and plasma characteristics with their material properties and device performance. In particular, the role of higher order silane gas (Si_2H_6) on deposition rate and film properties was studied.

1. For a-Si:H deposition development, it has been found that lower dihydride SiH_2 bond concentration (R_{mf}), correlates to more stable i layer, and can be achieved by increasing RF power, deposition temperature and/or H_2 dilution. The growth rate was increased by ~60% with the addition of only 1.7% Si_2H_6 into SiH_4/H_2 mixture. Such high growth rate a-Si:H solar cells exhibit comparable device performance to the baseline solar cells deposited without additive. The optimization of a-Si:H process indicated that lower R_{mf} could be achieved at high RF power and high growth rate with Si_2H_6 additive. A solar cell with initial efficiency of 7.4% was fabricated with i-layer deposited with Si_2H_6 additive at a high growth rate of $> 5\text{A/s}$. The stabilized performance after light exposure was similar to the baseline cell grown at 1.8 A/s without Si_2H_6 additive.

2. The process window transition from a-Si:H deposition to nc-Si:H deposition could be reached by increasing H_2/SiH_4 ratio or discharge power. Larger grain size was obtained at higher deposition pressure with RF discharge. The nc-Si:H preferential growth orientation could be tuned from (111) to (220) by changing H_2/SiH_4 ratio. The transition from a-Si:H to nc-Si:H required lower H_2/SiH_4 ratio in VHF discharge which is beneficial for high growth rate process. Larger grain size was also achieved by VHF at lower pressure compared to RF discharge.

3. The plasma discharge for a-Si:H and nc-Si:H had been characterized *in-situ* by OES and Langmuir Probe, correlating with the material properties. It had been found that OES SiH* intensity was proportional to the growth rate. The film deposited by discharge plasma with higher $H\alpha/SiH^*$ shows lower R_{mf} for a-Si:H and higher Raman X_c for nc-Si:H films, respectively. The EEDF analysis from Langmuir probe I-V measurement showed an increase of higher energy electron percentage at higher RF power, resulting higher H_2 dissociation level for larger $H\alpha/SiH^*$ detected by OES. The electron temperature and plasma potential decreased at higher process pressure resulting less ion-surface bombardment for larger grain size formation. The VHF plasma had one order of magnitude higher electron density compared with RF discharge leading to higher H_2/SiH_4 utilization.

This thesis has developed a knowledge base to understand the relationship between a-Si:H and nc-Si:H deposition conditions, material properties and plasma characterization. From the point view of the deposition, it is critical to develop high quality a-Si:H and nc-Si:H processing with an increased growth rate for cost

reduction. It would be interesting to test other silicon source gases with lower threshold energy and larger cross section for dissociation and ionization. The development of high density plasma process is also necessary for growth rate enhancement and better gas utilization. More detailed understanding of the correlation between the deposition condition and plasma properties are recommended for future work. Theoretical plasma modeling might provide guidance to further establish the relation between process condition, material properties and in-situ plasma diagnostic results.

REFERENCES

- [1] J. Walsh, "Projectin of Cumulative World Conventional Oil Production, Remaining Resources and Reserves to 2050," March 2000.
- [2] G. Research/SEIA, "Solar Market Insight Report 2014 Q1," 2014. [Online]. Available: www.seia.org/research-resources/solar-market-insight-report-2014-q1.
- [3] J. Rath, M. Brinza, Y. Liu, A. Borreman and R. Schropp, "Fabrication of thin film silicon solar cells on plastic substrate by very high frequency PECVD," *Solar Energy Materials and Solar Cells*, vol. 94, no. 9, pp. 1534-1541, 2010.
- [4] B. Yan and G. Yue, "Status of nc-Si:H Solar Cells at United Solar and Roadmap for Manufacturinga-Si:H and nc-Si:H Based Solar Panels," *MRS Proceedings*, vol. 989, 2007.
- [5] L. Antonio and S. Hegedus, *Handbook of Photovoltaic Science and Engineering*, Wiley, 2011.
- [6] D. Carlson and C. Wronski, "Amorphous silicon solar cell," *Applied Physics Letter*, vol. 28, p. 671, 1976.
- [7] S. Kim, J.-W. Chung, H. Lee, J. Park, J. Park, Y. Heo and H.-M. Lee, "Remarkable progress in thin-film silicon solar cells using high-efficiency triple-junction technology," *Solar Energy materials & Solar Cells*, vol. 119, p. 26, 2013.
- [8] D. Staebler and C. Wronski, "Reversible conductivity changes in discharge-produced amorphous Si," *Applied Physics Letters*, vol. 31, p. 292, 1977.
- [9] S. Shimizu, M. Kondo and A. Matsuda, "A highly stabilized hydrogenated amorphous silicon film having very low hydrogen concentration and an improved Si bond network," *Journal of Applied Physics*, vol. 97, no. 3, 2005.

- [10] J.-H. Yoon and K.-T. Lee, "Light-induced effects in hydrogenated amorphous silicon films grown from high hydrogen dilution of silane," *Journal of Non-Crystalline Solids*, Vols. 299-302, pp. 487-491, 2002.
- [11] A. Mahan, J. Carapella, B. Nelson, R. Crandall and I. Balberg, "Deposition of device quality, low H content amorphous silicon," *Journal of Applied Physics*, vol. 69, no. 9, p. 6728, 1991.
- [12] V. L. Dalal, E. X. Ping, S. Kaushal, M. K. Bhan and M. Leonard, "Growth of high quality amorphous silicon films with significantly improved stability," *Applied Physics Letters*, vol. 64, no. 14, p. 1862, 1994.
- [13] J. Yang, X. Xu and S. Guha, "Stability Studies of Hydrogenated Amorphous Silicon Alloy Solar Cells Prepared with Hydrogen Dilution," *Materials Research Society Proceedings*, vol. 336, pp. 687-692, 1994.
- [14] H. Keppner, J. Meier, P. Torres, D. Fischer and A. Shah, "Microcrystalline silicon and micromorph tandem solar cells," *Applied Physics A*, vol. 69, no. 2, pp. 169-177, 1999.
- [15] K. Yamamoto, A. Nakajuma and e. al., "A high efficiency thin film silicon solar cell and module," *Solar Energy*, vol. 77, no. 6, pp. 939-949, 2004.
- [16] O. Vetterl, F. Finger, R. Carius, P. Hapke, L. Houben, O. Kluth, A. Lambertz, A. Muck, B. Rech and H. Wagner, "Intrinsic microcrystalline silicon: A new material for photovoltaics," *Solar Energy Materials and Solar Cells*, vol. 62, no. 1-2, pp. 97-108, 2000.
- [17] K. Saito and M. Kondo, "Control of preferential orientation of microcrystalline silicon and its impact on solar cell performance," *Progress in Photovoltaics: Research and Applications*, vol. 19, p. 858-864, 2010.
- [18] A. Shah, J. Meier, E. Vallat-Sauvain, C. Droz, U. Kroll, N. Wyrsh, J. Guillet and U. Graf, "Microcrystalline silicon and 'micromorph' tandem solar cells," *Thin Solid Films*, Vols. 403-404, pp. 179-187, 2002.
- [19] M. Vanecek, A. Poruba, Z. Remes, N. Beck and M. Nesladek, "Optical properties of microcrystalline materials," *Journal of Non-Crystalline Solids*, Vols. 227-230, pp. 967-972, 1998.

- [20] J. Meier, U. Kroll, E. Vallat-Sauvain, J. Spitznagel, U. Graf and A. Shah, "Amorphous solar cells, the micromorph concept and the role of VHF-GD deposition technique," *Solar Energy*, vol. 77, pp. 983-993, 2004.
- [21] M. Kondo, M. Fukawa, L. Guo and A. Matsuda, "High rate growth of microcrystalline silicon at low temperatures," *Journal of Non-Crystalline Solids*, Vols. 266-269, pp. 84-89, 2000.
- [22] A. Hammad, E. Amanatides, D. Mataras and D. Rapakoulias, "PECVD of hydrogenated silicon thin films from $\text{SiH}_4 + \text{H}_2 + \text{Si}_2\text{H}_6$ mixtures," *Thin Solid Films*, Vols. 451-452, pp. 255-258, 2004.
- [23] E. Katsia, E. Amanatides, D. Mataras, A. Soto and G. Voyiatzis, "Total SiH_4/H_2 pressure effect on microcrystalline silicon thin films growth and structure," *Solar Energy Materials & Solar Cells*, vol. 87, pp. 157-167, 2005.
- [24] T. Nishimoto, M. Takai, H. Miyahara, M. Kondo and A. Matsuda, "Amorphous silicon solar cells deposited at high growth rate," *Journal of Non-Crystalline Solids*, Vols. 299-302, pp. 1116-1122, 2002.
- [25] Y. Yamauchi, T. Baba, T. Yamane, Y. Takeuchi, H. Takatsuka, H. Muta, K. Uchino and Y. Kawai, "Dominant ion species in VHF SiH_4/H_2 plasma," *Physics Status Solidi C*, vol. 7, no. 3-4, pp. 549-552, 2010.
- [26] H. Wiesmann, A. Ghosh, T. McMahan and M. Strongin, "a-Si:H produced by high-temperature thermal decomposition of silane," *Journal of Applied Physics*, vol. 50, no. 5, p. 3752, 1979.
- [27] P. Capezzuto, A. Madan and G. Bruno, in *Plasma Deposition of Amorphous Silicon-Based Materials*, Academic Press, 1995, p. 9.
- [28] P. Capezzuto, A. Madan and G. Bruno, in *Plasma Deposition of Amorphous Silicon-Based Materials*, Academic Press, 1995, p. 6.
- [29] D. Hess, "Plasma-Surface Interactions in Plasma-Enhanced Chemical Vapor Deposition," *Annual Review of Materials Science*, vol. 16, pp. 163-183, 1986.
- [30] R. Schropp and M. Zeman, *Amorphous and Microcrystalline Silicon Solar Cells: Modeling, Materials and Device Technology*, Springer, 1998.

- [31] A. Gallagher, "Neutral radical deposition from silane discharges," *Journal of Applied Physics*, vol. 63, no. 7, p. 2406, 1988.
- [32] W. Kessels, Y. Barrell, P. van den Oever, J. Hoefnagels and M. van de Sanden, "The a-Si:H growth mechanism: Temperature study of the SiH₃ surface reactivity and the surface silicon hydride composition during film growth," *MRS Proceedings*, vol. 762, 2003.
- [33] M. Lieberman and A. Lichteberg, *Principles of Plasma Discharges and Materials Processing*, Wiley-Interscience, 2005.
- [34] A. Matsuda and K. Tanaka, "Plasma spectroscopy-Glow discharge deposition of hydrogenated amorphous silicon," *Thin Solid Films*, vol. 92, no. 1-2, pp. 171-187, 1982.
- [35] E. Shun'ko, *Langmuir Probe in Theory and Practice*, Universal Publishers, 2009.
- [36] M. Druyvesteyn and F. Penning, "The mechanism of electrical discharges in gases of low pressure," *Review of Modern Physics*, vol. 12, no. 2, pp. 87-174, 1940.
- [37] C. Wadhwa, *High Voltage Engineering*, New Age Science, 2010.
- [38] E. Centurioni, "Generalized matrix method for calculation of internal light energy flux in mixed coherent and incoherent multilayers," *Applied Optics*, vol. 44, no. 35, p. 7532, 2005.
- [39] J. Tauc, "Optical properties and electronic structure of amorphous Ge and Si," *Materials Research Bulletin*, vol. 3, no. 1, pp. 37-46, 1968.
- [40] S. Kageyama, A. Masataka and F. Hiroyuki, "Dielectric function of a-Si:H based on local network structures," *Physical Review B*, vol. 83, no. 19, 2011.
- [41] N. Nakamura, T. Takahama, M. Isomura, M. Nishikuni, K. Yoshida, S. Tsuda, S. Nakano, M. Ohnishi and Y. Kuwano, "The influence of the Si-H₂ bond on the light-induced effect in a-Si:H films and a-Si:H solar cells," *Japanese Journal of Applied Physics*, vol. 28, no. 10, pp. 1762-1768, 1989.

- [42] G. Amato, G. Mea, F. Fizzotti, R. Marchisio and A. Paccagnella, "Hydrogen bonding in amorphous silicon with use of the low-pressure chemical-vapor-deposition technique," *Physical Review B*, vol. 43, p. 6627, 1991.
- [43] C. Smit, R. van Swaaij, H. Donker, A. Petit, W. Kessels and M. van de Sanden, "Determining the material structure of microcrystalline silicon from Raman spectra," *Journal of Applied Physics*, vol. 94, no. 5, p. 3582, 2003.
- [44] E. Bustarret, M. Hachicha and M. Brunel, "Experimental determination of the nanocrystalline volume fraction in silicon thin films from Raman spectroscopy," *Applied Physics Letters*, vol. 52, no. 20, p. 1675, 1988.
- [45] P. A., "The Scherrer Formula for X-Ray Particle Size Determination," *Physical Review*, vol. 56, p. 978, 1939.
- [46] C. Honsberg and S. Bowden, "PVCROM," [Online]. Available: www.pveducation.org.
- [47] A. Matsuda, M. Takai, T. Nishimoto and M. Kondo, "Control of plasma chemistry for preparing highly stabilized amorphous silicon at high growth rate," *Solar Energy Materials and Solar Cells*, vol. 78, no. 1-4, pp. 3-26, 2003.
- [48] W. Futako, T. Takagi, T. Nishimoto, M. Kondo, I. Shimizu and A. Matsuda, "Gas Phase Diagnosis of Disilane/Hydrogen RF Glow Discharge Plasma and Its Application to High Rate Growth of High Quality Amorphous Silicon," *Japanese Journal of Applied Physics*, vol. 38, p. 4535, 1999.
- [49] C. Cody, B. Abeles, R. Wronski, R. Stephens and B. Brooks, "Optical characterization of amorphous silicon hydride films," *Solar Cells*, vol. 2, p. 227, 1980.
- [50] V. Dalal, M. Leonard, J. Booker, A. Vaseashta and S. Hegedus, "Quantum Efficiency of Amorphous Alloy Solar Cells," *Proceeding of 18th IEEE Photovoltaic Specialists Conference*, p. 837, 1986.
- [51] B. Yan, G. Yue, J. Yang, S. Guha and D. Williamson, "Hydrogen dilution profiling for hydrogenated microcrystalline silicon solar cells," *Applied Physics Letters*, vol. 85, p. 1955, 2004.

- [52] C. Ross, Y. Mai, R. Carius and F. Finger, "Use of seed layers for structure, optical, and electronic transport measurements on microcrystalline silicon on glass," *Progress in Photovoltaics*, vol. 19, no. 6, pp. 715-723, 2011.
- [53] S. Hegedus, "Effect of Plasma and Thermal Annealing on Optical and Electronic Properties of SnO₂ Substrates Used for a-Si:H Solar Cells," *Journal of Applied Physics*, vol. 92, no. 1, p. 620, 2002.
- [54] Z. Hu, X. Liao, H. Diao, Y. Cai, S. Zhang, E. Fortunato and R. Martins, "Hydrogenated p-type nanocrystalline silicon in amorphous silicon solar cells," *Journal of Non-Crystalline Solids*, vol. 352, pp. 1900-1903, 2006.
- [55] Y. Fu, J. Luo, S. Milne, A. Flewitt and W. Milne, "Residual stress in amorphous and nanocrystalline Si films prepared by PECVD with hydrogen dilution," *Materials Science and Engineering B*, Vols. 124-125, pp. 132-137, 2005.
- [56] M. Kushner, "A model for the discharge kinetics and plasma chemistry during plasma enhanced chemical vapor deposition of amorphous silicon," *Journal of Applied Physics*, vol. 63, p. 2532, 1988.
- [57] H. Moutinho, C. Jiang, J. Perkins, Y. Xu, B. Nelson, K. Jones, M. Romero and M. Al-Jassim, "Effects of dilution ratio and seed layer on the crystallinity of microcrystalline silicon thin films deposited by hot-wire chemical vapor deposition," *Thin Solid Films*, vol. 430, pp. 135-140, 2003.
- [58] M. Python, O. Madani, D. Domine, F. Meillaud, E. Vallat-Sauvain and C. Ballif, "Influence of the substrate geometrical parameters on microcrystalline silicon growth for thin-film solar cells," *Solar Energy Materials and Solar Cells*, vol. 93, no. 10, pp. 1714-1720, 2009.
- [59] P. Ray, N. Gupta and P. Chaudhuri, "Calculation of the Precursor Flux from Optical Emission Spectroscopy Data in Plasma Enhanced Chemical Vapour Deposition of Silane and its Correlation with the Deposition Rate," *Japanese Journal of Applied Physics*, vol. 41, pp. 3955-3960, 2002.
- [60] T. Moiseev, G. Isella, D. Chrastina and C. Cavallotti, "Langmuir probe plasma parameters and kinetic rates in a Ar-SiH₄-H₂ plasma during nc-Si:H films deposition for photovoltaic applications," *Journal of Physics D: Applied Physics*, vol. 42, p. 225202, 2009.

- [61] W. Du, X. Yang, H. Povolny, X. Liao and X. Deng, "Impact of hydrogen dilution on microstructure and optoelectronic properties of silicon films deposited using trisilane," *Journal of Physics D: Applied Physics*, vol. 38, no. 6, p. 838, 2005.
- [62] R. Platz, S. Wagner, C. Hof, A. Shah, S. Wieder and B. Rech, "Influence of excitation frequency, temperature, and hydrogen dilution on the stability of plasma enhanced chemical vapor deposited a-Si:H," *Journal of Applied Physics*, vol. 84, no. 7, p. 3949, 1998.
- [63] "Compilation of electron cross sections," LXCAT, [Online]. Available: <http://www.lxcat.laplace.univ-tlse.fr>.

Appendix

A-Si:H P-I-N SOLAR CELL STABILITY

The a-Si:H solar cell performance degrades with light exposure, which is well known named Staebler-Wronski effect. The device stability is highly correlated with the bulk material properties such as low microstructure factor and hydrogen content of intrinsic layer. In this thesis, the deposition with hydrogen dilution and high substrate temperature has been studied to improve baseline solar cell stability.

Table A-1 presents J-V results of the initial and after 380 hrs light soaking for the three cells including baseline condition, higher growth temperature and H₂ dilution. The baseline solar cell with i layer at 200 °C without H₂ dilution degrades more than 28% after 380 hrs light soaking, mainly on Fill Factor. By increasing growth temperature or using H₂ dilution, the stability is much improved with degradation around 15% to 17%. The two most stable ones have the lowest R_{mf} while the least stable one has the highest R_{mf}, which indicating R_{mf} is an important material properties relating with solar cell stability.

Table A-1 Device stability performance of p-i-n solar cells fabricated at: 1. 200C and 2. 250C, RF 25W, 0.5 Torr with pure SiH₄; 3. 200C, RF 30W, 1.25 Torr with H₂ dilution R=5

Cell #	i layer	LS Time (hr)	V _{oc} (Volts)	J _{sc} (mA/cm ²)	FF (%)	E _{ff} (%)	Degradation % of E _{ff}
a	200 C 0.5T;R=0 R _{mf} =22%	0	0.899	11.9	73.8	7.8	28.2%
		380	0.845	11.4	58.2	5.6	
b	250 C 0.5T;R=0 R _{mf} =8%	0	0.845	11.9	73	7.4	17.5%
		380	0.820	11.7	63.9	6.1	
c	200 C 1.25T;R=5 R _{mf} =7%	0	0.88	11.4	71.4	7.2	15.2%
		380	0.87	11.1	63.7	6.1	

Figure A-1 shows the efficiency degradation curve of the three cells during light soaking. The baseline Cell 1 is still degrading after 380 hrs light soaking, while the cell efficiency of Cell b and c with higher growth temperature or H₂ dilution respectively have much better performance, which got stabilized after ~200 hrs light soaking. The better stability could be explained by the less dihydride bonding concentration inside i layers with higher growth temperature or H₂ dilution.

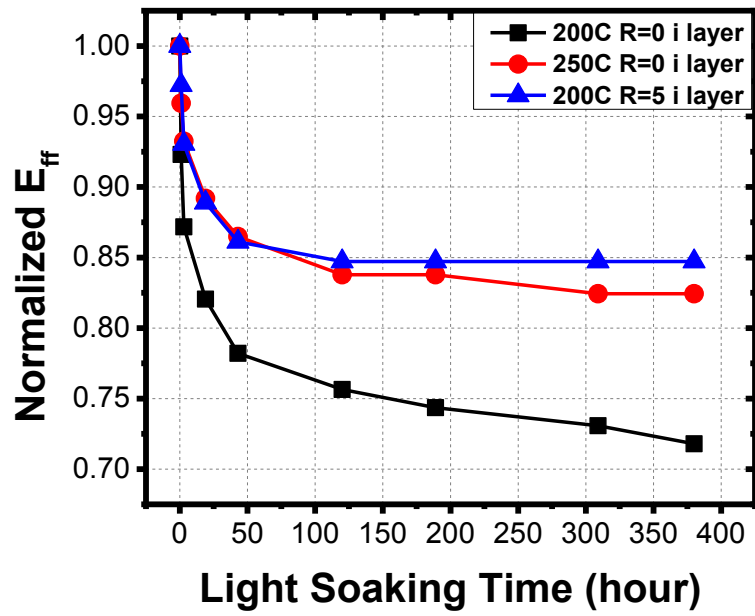


Figure A-1 Normalized Stability of 3 devices: baseline; higher growth temperature; H₂ dilution